Title
Point Defects in Two-Dimensional Layered Semiconductors: Physics and Its Applications

Author
Suh, Joonki

Publication Date
2015

Peer reviewed|Thesis/dissertation

Point Defects in Two-Dimensional Layered Semiconductors: Physics and Its Applications

By

Joonki Suh

A dissertation submitted in partial satisfaction of the

requirements for the degree of

Doctor of Philosophy

in

Engineering – Materials Science and Engineering

in the

Graduate Division

of the

University of California, Berkeley

Committee in charge:

Professor Junqiao Wu, Chair

Professor Jie Yao

Professor Chris Dames

Summer 2015

Point Defects in Two-Dimensional Layered Semiconductors:

Physics and Its Applications

Abstract

Point Defects in Two-Dimensional Layered Semiconductors: Physics and Its Applications

by

Joonki Suh

Doctor of Philosophy in Materials Science and Engineering

University of California, Berkeley

Professor Junqiao Wu, Chair

Recent advances in material science and semiconductor processing have been achieved largely based on in-depth understanding, efficient management and advanced application of point defects in host semiconductors, thus finding the relevant techniques such as doping and defect engineering as a traditional scientific and technological solution. Meanwhile, two-dimensional (2D) layered semiconductors currently draw tremendous attentions due to industrial needs and their rich physics at the nanoscale; as we approach the end of critical device dimensions in silicon-based technology, ultra-thin semiconductors have the potential as next-generation channel materials, and new physics also emerges at such reduced dimensions where confinement of electrons, phonons, and other quasi-particles is significant. It is therefore rewarding and interesting to understand and redefine the impact of lattice defects by investigating their interactions with energy/charge carriers of the host matter. Potentially, the established understanding will provide unprecedented opportunities for realizing new functionalities and enhancing the performance of energy harvesting and optoelectronic devices.

In this thesis, multiple novel 2D layered semiconductors, such as bismuth and transition-metal chalcogenides, are explored. Following an introduction of conventional effects induced by point defects in semiconductors, the related physics of electronically active amphoteric defects is revisited in greater details. This can elucidate the complication of a two-dimensional electron gas coexisting with the topological states on the surface of bismuth chalcogenides, recently suggested as topological insulators. Therefore, native point defects are still one of the keys to understand and exploit topological insulators.

In addition to from a fundamental science point of view, the effects of point defects on the integrated thermal-electrical transport, as well as the entropy-transporting process in thermoelectric materials are thoroughly investigated. Point defects can potentially beat the undesired coupling, often term “thermoelectric Bermuda triangle”, among electrical conductivity, thermal conductivity and thermopower. The maximum thermoelectric

performance is demonstrated with an intermediate density of defects when they beneficially and multi-functionally act as electron donors, as well as strongly energy-dependent electron and phonon scatterers. Therefore, this is a good example of how fundamental defect physics can be applied for practical devices toward renewable energy technology.

Another interesting field of layered nanomaterials is on transition-metal dichalcogenides (TMDs), sensational candidates for 2D semiconductor physics and applications. At the reduced dimensionality of 2D where a far stronger correlation between point defects and charge carriers is expected, it is studied how chalcogen vacancies alter optical properties of monolayer TMDs. A new, sub-bandgap broad emission lines as well as increase in the overall photoluminescence intensity at low temperatures are reported as a result of high quantum efficiency of excitons, *i.e.*, bound electron-hole pairs, localized at defect sites. On electrical transport, both *n*- and *p*-type materials are needed to form junctions and support bipolar carrier conduction while typically only one type of doping is stable for a particular TMD. For example, MoS_2 is natively n-type, thus the lack of *p*-type doping hampers the development of charge-splitting *p*-*n* junctions of MoS_2. To address this issue, we demonstrate stable *p*-type conduction in MoS_2 by substitutional Nb doping up to the degenerate level. Proof-of-concept, van der Waals *p*-*n* homo-junctions based on vertically stacked MoS_2 layers are also fabricated which enable gate-tuneable current rectification. Various electronic devices fabricated are stable in ambient air even without additional treatment such as capping layer protection, thanks to the substitutionality nature of the doping; this is in stark contrast to the existing approach of using molecular doping, which usually suffers from volatility and reactivity with air and/or water molecules.

Dedicated to my parents, *Sungki Suh* & *Myungsook An*,
and my family, *Mido*, *Chloe* & *Aiden*,
for their unconditional love, sacrifice & devotion

Table of Contents

List of Figures

List of Table

Acknowledgements

I am most thankful to my advisor, Prof. Junqiao Wu, for his excellent guidance and ceaseless support over the past five years. He has shaped my own way of designing, leading and concluding scientific works with his solid knowledge and passion. We always initiated a research project under his clear and enlightening physics pictures, and enjoyed our journey toward comprehensive understanding and solution. Even when abstruse problems were often encountered, he systematically simplified them such that I could find the best strategy to proceed. Thinking in a simple but technically sound manner has been the most valuable training with him at Berkeley. I also appreciate his constant trust in my decisions from which I could develop responsibility and leadership to become a good mentor of others like him.

I have been also blessed to have an eminent group of other academic mentors. I would like to first thank Dr. Wladek Walukiewicz and Prof. Kin Man Yu for all their frequent advice, inspiration and support. Furthermore, I would like to thank Prof. Chris Dames and Prof. Ali Shakouri for their support and education on thermal and thermoelectric physics as well. I would also express my great appreciation to Prof. Oscar Dubon, Prof. Mark Asta and Prof. Andrew Minor for serving on my qualifying exam committee and helping me refining my research plan. And I would like to acknowledge the fruitful collaborations with Prof. Feng Wang's group and Prof. Jie Yao's group on further understanding the optical properties of chalcogenide nanostructures. Finally, I would like to thank Prof. Zhenan Bao who provided the very first research opportunity during my master's degree at Stanford University.

I consider myself fortunate to be among the many bright and fine colleagues in the Wu group. Dr. Sefaattin Tongay, a fellow postdoctoral researcher, introduced me the field of 2D materials and established long-term and fruitful collaborations on that subject. Dr. Deyi Fu, another fellow postdoctoral researcher with whom I discussed semiconductor physics on a daily basis, is a bright and kind person. Dr. Kai Liu, Dr. Wen Fan and Kevin Wang, who were always great laboratory buddies, kept encouraging me and helped me in all possible ways. I would also like to thank Dr. Sangwook Lee, Dr.

Hwan Sung Choe and Dr. Changhyun Ko for sharing with me their broad experimental techniques and knowledge. And lastly I want to thank all the other fellow students and postdocs in Wu group for their support; they are Dr. Greg Brown, Dr. Devesh Khanal, Dr. Joanne Yim, Prof. Jijun Zou, Dr. Alejandro Levander, Prof. Chenglun Hsin, Prof. Chun Cheng, Dr. Tyler Matthews, Dr. Jian Zhou, Prof. Ning Wang, Prof. Juan F. Sanchez-Royo, Alex Luce, Dr. Qinglin Xia and Dr. Yabin Chen.

I had the pleasure to work collaboratively with a number of leading groups in their fields. Most notably: Prof. Chris Dames (Dr. Christian Monachon and Sean Lubner) Prof. Feng Wang (Dr. Jonghwan Kim, Chenhao Jin, Dr. Yinghui Sun and Dr. Xiaoping Hong), Prof. Ali Shakouri (Dr. Tela Favaloro), Prof. Renkun Chen (Dr. Jaeyun Moon), Prof. Costas Grigoropoulos (Dr. Jae Hyuck Yoo), Prof. Jeong Young Park at KAIST (Dr. Jonghun Kim, Dr. Hyunsoo Lee and Jaehyeon Kim), Prof. Heonjin Choi at Yonsei (Jaejun Lee), Prof. Goki Eda at NUS (Dr. Weijie Zhao), Dr. Joonyeon Chang at KIST (Dr. Tae-Eon Park), Prof. Robert Sinclair (Joonsuk Park and Dr. Hee Joon Jung), Prof. Jacek Furdyna at University of Notre Dame (Dr. Xinyu Liu), Prof. Dong Yu at UC Davis, Prof. Long-Qing Chen (Dr. Yijia Gu) and Prof. Jeffrey Grossman at MIT (Dr. Can Ataca). I also want to thank Prof. Der-Yuh Lin, Dr. Jingbo Li, Dr. Yeonbae Lee and Jeffrey Beeman for their thorough help.

Finally I am most thankful to my family for their support to pursue my dreams for the last five years. Many sacrifices were made but without their unconditional support I never would have been able to accomplish this dream. I would like to thank my father Sungki Suh who encouraged me along the way as he pioneered a semiconductor industry decades ago. I would like to thank my mother Myungsook An who always provided me the best experience of life and education. I would like to thank my wife Mido who was willing to come to the States and become a part of my life. Finally, I would like to express my love to my daughter Chloe and my son Aiden who are my precious treasure.

Chapter 1

Introduction

I am among those who think that science has great beauty. A scientist in his laboratory is not only a technician: he is also a child placed before natural phenomena which impress him like a fairy tale. We should not allow it to be believed that all scientific progress can be reduced to mechanisms, machines, gearings, even though such machinery also has its beauty.

MARIE CURIE (1867 – 1934)

Point defects including intrinsic native defects and extrinsic dopants in crystalline semiconductors have been a subject of tremendous interest from the viewpoints of fundamental condensed matter physics as well as semiconductor technology. Generally, they can be classified into either delocalized shallow dopants or highly localized deep level defects (and dopants such as transition metal donor/acceptor). As witnessed during the past decades, the former led to the revolutionary developments of semiconductor industry by tailoring "impure" semiconductors to a certain extent upon technological demand. For instance, their delocalized wave functions are intimately associated with the corresponding band edges (e.g., donors for conduction band minimum and acceptors for valence band maximum), thus the electrical resistivities of host semiconductors can be efficiently modified over a wide range. In the case of the latter, material properties are differently, but still significantly, affected owing to their localized wave functions constructed by all the extended states in the Brillouin zone. Representative examples

among their multiple functions are recombination and scattering centers of free charge carriers and trapping sites for Coulomb-bound electron-hole pairs, *i.e.,* excitons. As outlined above, point defects thus affect a variety of physical properties of host semiconductors ranging from electrical and thermal transport to optical transitions including photon emission and absorption. Those all stem from a strong interaction between point defects and host lattice matrix. Consequently, chemical doping and defect management in semiconductor research have served as the most *conventional* scientific and technological approach to optimize and enhance their device performances thanks to their reliability and a broad range of tunability.

1.1 When *conventional* meets *unconventional*: Emergence of two-dimensional layered semiconductors

Two-dimensional (2D) layered crystals have recently emerged as *unconventional* class of materials with many peculiar physical phenomenon and remarkable properties of novel devices. Its vast family includes almost all kinds of building blocks of modern electronics and sustainable energy technologies. Bismuth chalcogenides such as Bi_2Te_3 and Bi_2Se_3 are a typical example of such materials best known as commercially available thermoelectrics. They redraw attentions due to their unique band structures and spin properties as three-dimensional topological insulators where the bulk is a conventional band insulator, but the exotic surface possesses gapless electronic states carrying back-scattering-free electric current along with the spin-momentum locking property [1,2]. Even more recently, transition-metal dichalcogenides, as atomically thin 2D semiconductors, are resurged as an indispensable member of 2D materials family. When thinned down to a single-layer thickness, they have demonstrated extraordinary properties including the direct band gap emission in the visible frequency range, the striking spin-orbit coupling, the ultra-strong Coulomb interaction, and the novel physics related to the valley degree of freedom.

The interaction between point defects and other (quasi-) particles (*e.g.,* electron, phonon and exciton) in 2D semiconductors is by nature expected to become far stronger at such miniaturized dimensionalities, comparable to the thickness of unit cell, where associated electron wave function is tightly localized and confined. Considering that it will greatly influence on various material properties and the existence of defects are inevitable to the growth of nanomaterials owing to the immature synthetic process, in-depth understanding their interactions and resultant effects in 2D layered semiconductors will bring a high impact to the materials research community. This will also open a new route toward on-demand control of many physical characteristics in corresponding 2D materials, ultimately leading to nanotechnology innovations.

1.2 Outline of thesis

In Chapter 2–3 we focus on defect physics and the related thermoelectric application of bismuth chalcogenides, a narrow bandgap layered semiconductor. Profound understanding is first developed to clarify the physical origin of two-dimensional electron gas coexisting with topological surface states of Bi_2Te_3, Bi_2Se_3, and their ternary alloys in Chapter 2. Electron density in topological insulator thin films are manipulated by controlling the density of electronically active native defects with particle irradiation, and the results are in quantitative agreement with the amphoteric defect model, which predicts that electronically active native defects shift the Fermi energy toward a Fermi stabilization level located universally at ~4.9 eV below the vacuum level. We further applied the obtained insight and experimental technique to thermoelectric properties of Bi_2Te_3 in Chapter 3. It is demonstrated that simultaneous increases in the in-plane electrical conductivity (up to 200%) and thermopower (up to 70%) by controlling native defects in Bi_2Te_3 films, leading to a high power factor of 3.4×10^{-3} $Wm^{-1}K^{-2}$. Potentially, these defects may further improve performance by reducing the thermal conductivity. The maximum enhancement of thermoelectric performance occurs at an intermediate dosage where the native defects act beneficially as electron donors as well as electron and phonon scatterers. In addition, another novel observation of nanoscale thermoelectric phenomenon at metal-insulator domain walls in a single vanadium dioxide nanobeams is briefly discussed in Appendix A.

In Chapter 4, we investigate effects of anion vacancies, the dominant point defect species, in monolayer transition metal dichalcogenides as 2D semiconductors where the vacancies density is controlled by both alpha particle irradiation or thermal-annealing. We found a new, sub-bandgap broad emission peak as well as increase in overall photoluminescence intensity upon the vacancy generation, thus can conclude that in opposite to conventional wisdom, optical quality at room temperature cannot be used as criteria to assess crystal quality of the 2D semiconductors and point defects have huge effects to localize excitons at reduced temperatures. With this vast information, defect engineering can offer a new route toward tailoring optical properties of 2D semicondcutors.

Next in Chapter 5, we present a substitutional doping technique in layered transition metal dichalcodenides for which typically only one type of doping is inherently available and stable. As an example, stable *p*-type conduction in molybdenum disulfide (MoS_2), natively *n*-type semiconductor, is achieved by substitutional niobium (Nb) doping, leading to a degenerate hole density of $\sim 3 \times 10^{19}$ cm^{-3}. Structural and X-ray techniques reveal that the Nb atoms are indeed substitutionally incorporated into MoS_2

by replacing the Mo cations in the host lattice. van der Waals *p*–*n* homojunctions based on vertically stacked MoS_2 layers are fabricated, which enable gate-tunable current rectification. A wide range of nanoelectronic, optoelectronic, and spintronic devices can be envisioned from the demonstrated substitutional bipolar doping of MoS_2. From the miscibility of dopants with the host, it is also expected that the synthesis technique demonstrated here can be generally extended to other 2D semiconductors for doping against their native unipolar propensity.

Finally in Chapter 6, our comprehensive understanding obtained is summarized and corresponding future works are suggested toward greater implications on nanomaterial innovations.

Chapter 2

Defect physics in bismuth chalcogenides[1]

The saddest aspect of life right now is that science gathers knowledge faster than society gathers wisdom.

ISAAC ASIMOV (1920 – 1992)

Topological insulators (TIs) are of great interest owing to the topologically protected gapless surface states [1,2]. The novel topological surface states have been extensively studied and their existence has been experimentally confirmed by angle-resolved photoemission spectroscopy (ARPES) [3], scanning tunneling microscopy (STM) [4] and corresponding transport measurements [5,6]. Furthermore, they have the possibility of hosting novel physical phenomena, including Majorana fermions [7], magnetic monopoles [8], and quantum anomalous Hall effect [9], as well as of promising applications in spintronics and quantum computing. Bi_2Se_3 and Bi_2Te_3 are representative examples of such three-dimensional TIs, and their ternary alloys, $Bi_2(Se_{1-x}Te_x)_3$, have also been demonstrated to display TI properties [10].

More recently, coexistence of two distinctive types of surface conducting channels has been observed in both Bi_2Se_3 [11,12] and Bi_2Te_3 [13,14], one being Dirac electrons

[1] Reproduced in part with permission from J. Suh et al., "Fermi-level stabilization in the topological insulators Bi_2Se_3 and Bi_2Te_3: origin of the surface electron gas," Physical Review B **89,** 115307 Copyright 2014 American Physical Society.

from the topological state, and the other from a two-dimensional electron gas (2DEG). The latter has been often attributed to a conventional band-bending effect, without specifying its physical origin. As another possible explanation, an epitaxial bismuth bilayer (Bi_2) on top of bulk TIs has been hypothesized [15] and experimentally revealed by STM imaging [16]. However, the Bi bilayer formation was spatially non-uniform and triggered only by thermal activation; thus it cannot support the spontaneous formation of 2DEG universally observed in this family of TIs.

In this Chapter we present the first experimental evidence that the 2DEG in TIs is directly related to unavoidable native defects and associated dangling bonds present on the surface. The defect-induced pinning of surface Fermi energy was revealed through a combination of irradiation experiments where we intentionally generate native defects in the bulk, and theoretical analysis in terms of a widely applied defect model. Since in exploiting the unique properties of TIs it is often necessary to interface them with other materials, this demonstration of native-defect-induced 2DEG on TIs is a significant step toward better understanding of the topological states, and has important implications for applications of TIs in practical devices.

2.1 Theory: Review of amphoteric defect model

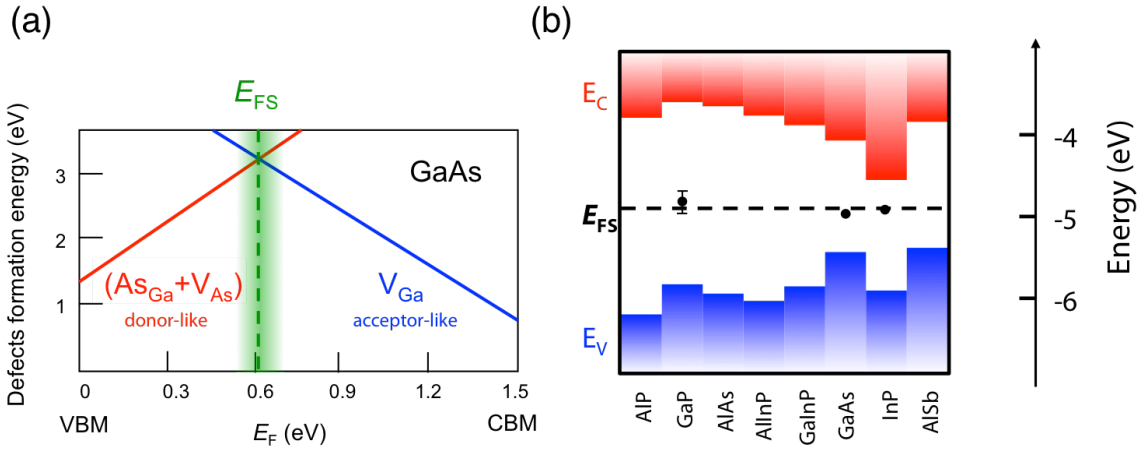

Figure. 2.1. Amphoteric defect model. (a) Formation energy of a gallium vacancy and the related donor defects as function of the Fermi energy in the GaAs band gap. (b) Band offsets and the Fermi level stabilization energy (E_{FS}) in various III-V compound semiconductors.

The mechanism explaining the defect induced stabilization of the Fermi energy is established based on the concept of amphoteric native defects. The amphoteric defect model (ADM) asserts that the formation energy of charged native defects, such as atomic vacancies, interstitials, and anti-sites, sensitively depends on the location of Fermi level in the host semiconducting crystals (Fig. 2.1(a)). In semiconductors with high defect concentrations, regardless of whether they are either intentionally introduced or intrinsically present, it was discovered that the Fermi level always moves toward the identical energy value, known as the Fermi stabilization energy (E_{FS}). This is often termed as the branch point energy or the charge neutrality level, independent of the particular host semiconductors or chemical dopants [17]. The stabilization of the Fermi energy can be now understood if we assume that the type of defects formed (*e.g.,* by high-energy particle irradiation) depends on the location of the Fermi energy with respect to E_{FS}. In the case of Fermi energy $E_F > E_{FS}$ ($E_F < E_{FS}$), acceptor-like (donor-like) defects are predominantly formed resulting in a gradual shift of the Fermi energy towards E_{FS}. Consequently, when the condition $E_F = E_{FS}$ is finally achieved, the donor- and acceptor-like defects are incorporated at the same rate such that they perfectly compensate each other stabilizing the Fermi energy.

Such an amphoteric behavior of native defects has been widely supported by *ab-initio* theoretical calculations that show the dependence of defect formation energies on E_F. In the case of GaAs it was shown that both gallium and arsenic vacancies can mutually undergo amphoteric transformations. For example, as illustrated in Fig. 2.1(a) V_{Ga} is a triple acceptor when E_F > valence band maximum (VBM) + 0.6 eV. However if the Fermi energies become significantly low and approaches to VBM, this defect configuration is relatively unstable and the vacancy undergoes a relaxation via defect migration. One possible scenario is that one of the first neighbor As atoms moves towards the vacant Ga site in this case, thus leaving a defect complex of As_{Ga} and V_{As} (Fig. 2.1(a)).

Notably, E_{FS} is universally located approximately 4.9 eV below the vacuum level, and this can be understood in a consideration of the fact that the amphoteric native defects are strongly localized in real spaces. Thus, their wave functions in *k*-space are extended over the entire Brillouin zone, leading to an energy level that is determined by regions with a large density of states, and becomes insensitive to the band edges of the host materials, which have a relatively small density of states. This universality is shown in Fig. 2.1(b) together with the natural band edge offsets of a variety of III-V compound semiconductors.

2.2 Experimental procedure and details

Thin films of Bi_2Se_3, Bi_2Te_3 and their ternary alloys were grown on semi-insulating GaAs (001) substrates with molecular beam epitaxy (MBE) [18]. The composition of ternary compounds was controlled by varying Se_2 and Te_2 beam fluxes to cover the entire composition range. After growth, the thickness and composition of TI films were precisely determined by Rutherford backscattering spectrometry (RBS), while the crystal structure was characterized by high resolution X-ray diffraction (XRD) and ion channeling. XRD measurements reveal the high crystal quality of these TI films with preferred crystal orientation along the c-axis (Fig. 2.2(a)). The existence of topological surface states in these films was confirmed by ARPES measurements [19].

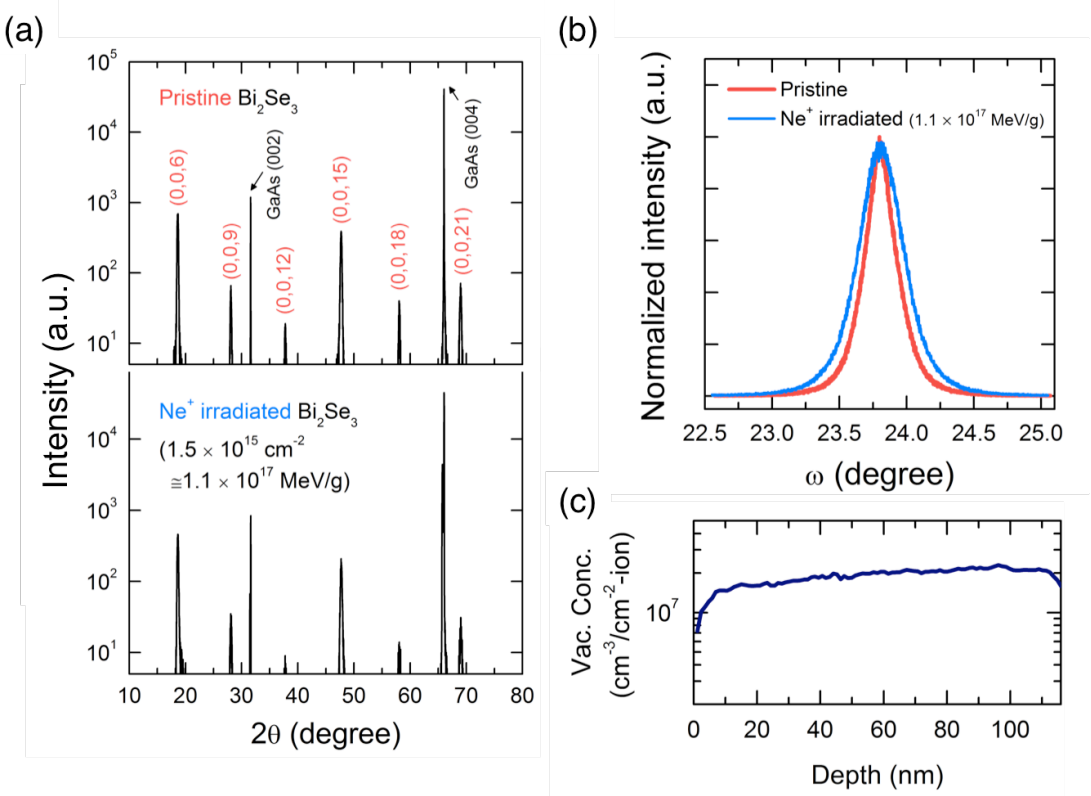

Figure. 2.2. X-ray diffraction spectra of a representative TI film. (a) θ - 2θ scans, and (b) Normalized ω rocking curves at (0,0,15) reflection of pristine film and Ne^+ irradiated at the highest displacement damage dose (D_d), 1.1×10^{17} MeV/g, of a 105-nm-thick Bi_2Se_3 film grown on semi-insulating GaAs (001) substrate. (c) SRIM-simulated depth profile of vacancy concentration generated by 150 keV Ne^+ bombardment in 116 nm Bi_2Te_3 film, the thickest film used in the irradiation experiment.

Native point defects in the TI films were generated by irradiating the samples with energetic ions. In order to compare the degree of irradiation damage (and hence the density of generated native defects) by different species of ions, the displacement damage dose (D_d) approach was utilized by extracting non-ionizing energy loss (NIEL) from Monte Carlo simulation with the Stopping Range of Ions in Matter (SRIM) program [20]. TI films were sequentially irradiated for D_d up to 2×10^{14} MeV/g with 3 MeV He^{2+} (up to an ion dose of 2×10^{15} cm^{-2}) and then for D_d ranging from 1×10^{15} to 1×10^{17} MeV/g with 150 keV Ne^{+} ions (with ion dose from ~ 10^{13} to 10^{15} cm^{-2}). Also, the maximum thickness of TI films used for this irradiation study was restricted by the projected range (~ 180 nm in $Bi_2(Se_{1-x}Te_x)_3$) for the 150 keV Ne^{+} irradiation. The thickness of the films in the irradiation study ranges from 29 to 116 nm. Thus most of the He^{2+} and Ne^{+} ions completely pass through the entire film thickness, leaving behind uniform damage throughout the film in both depth and lateral directions. SRIM predicts that the distribution of defect concentration is relatively uniform along the depth of TI films, even in the thickest 116 nm Bi_2Te_3 sample (Fig. 2.2(c)). It was also confirmed that the semi-insulating GaAs substrate still remains electrically highly insulating after the irradiation, so that we can confine our discussion to irradiation-induced native defects in the TI films. XRD pattern in Fig. 2.2(a) confirms that the high crystal quality of the film is still retained even after irradiation with the highest $D_d = 1.1 \times 10^{17}$ MeV/g, corresponding to Ne^{+} irradiation with a high dose of 1.5×10^{15} cm^{-2}. All diffraction peaks indeed remain sharp, although the full-width at half-maximum of the rocking curve is slightly increased from 0.27° to 0.39°, as seen in Fig. 2.2(b). This is a clear indication that irradiation within the doses used in our work generates only native point defects (vacancies and interstitials) in the TI films, and does not cause amorphization or formation of substantial amounts of extended defects.

2.3 Characterization: Hall-effect measurement

Figure 2.3 shows the evolution of electrical transport properties of Bi_2Se_3 and Bi_2Te_3 as native defects are introduced by irradiation, determined by room-temperature Hall effect measurements with a 0.6 T magnetic field in the van der Pauw configuration. The concentration of free electrons (n) in both binary TIs increases with increasing D_d as shown in Fig. 2.3(a); the irradiation-induced native defects behave as donors in these narrow-bandgap semiconductors. Accordingly, electron mobility is generally reduced due to increasing scattering events from the ionized native defects acting as charged scattering centers (Fig. 2.3(c)). Assuming that surfaces already are already saturated with a high density of native defects associated with dangling bonds, the decrease of measured

mobility is mainly caused by decrease in the bulk mobility upon irradiation. We note that our measured room-temperature mobilities in pristine films are consistent with report values in literature [21,22].

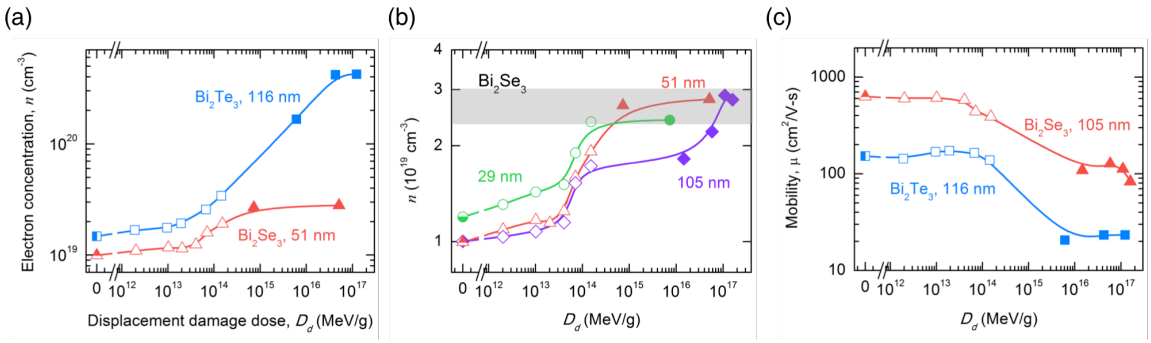

Figure 2.3. (a) Electron concentration, determined by Hall effect at room temperature, as a function of D_d in a Bi_2Se_3 (51 nm) and Bi_2Te_3 (116 nm) film. D_d was obtained by multiplying irradiation dose with NIEL calculated with SRIM. (b) Room-temperature electron concentration upon irradiation in three Bi_2Se_3 thin films with different thicknesses. The shaded region shows the approximate level where n saturates. (c) Carrier mobility as a function of D_d in a Bi_2Se_3 and Bi_2Te_3 film. All half-filled symbols correspond to pristine values. Open and filled symbols represent values measured on He^{2+} and Ne^{+} irradiated films, respectively. Solid lines are guides for the eye.

With further increase in damage dose, however, n ultimately saturates at a characteristic concentration (n_{sat}) that differs by more than an order of magnitude between Bi_2Se_3 ($n_{sat} \sim 3 \times 10^{19}$ cm^{-3}) and Bi_2Te_3 ($n_{sat} \sim 4 \times 10^{20}$ cm^{-3}). Regardless of film thicknesses which lead to different pristine n, the electron concentration is observed to saturate approximately at the same level (Fig. 2.3(b)). This means that n_{sat} is an intrinsic property of the material, corresponding to a Fermi-level (E_F) stabilized at a specific energy position. We also note that D_d required to achieve the carrier saturation is proportional to film thickness due to greater bulk contribution in thicker films.

2.4 Quantitative analysis with ADM

These observations can be well understood within the amphoteric defect model (ADM) developed based on E_F-dependent formation energy of native defects [23] as previously described in Chapter 2.1. To briefly summarize here, ADM predicts that, the formation energy and the type (donor or acceptor) of dominant native defects in a semiconductor is controlled by location of E_F relative to a nearly universal energy level located at about 4.9

eV below the vacuum level, termed as the Fermi stabilization level (E_{FS}). Thus, donor (acceptor)-like native defects are predominantly formed when $E_F < E_{FS}$ ($E_F > E_{FS}$). Consequently, for sufficiently high defect concentration, E_F stabilizes at E_{FS}, where the formation energies and incorporation rates of donor-like defects become equal to those of acceptor-like. The ADM concept with the universal E_{FS} has been successfully applied to a wide range of elemental and compound semiconductors [17]. Therefore, the location of E_F relative to the known E_{FS} is a key parameter to gauge electronic properties of native defects. First, the energies of band edges in Bi_2Te_3 can be deduced from its intrinsic bandgap (E_G^0 = 0.17 eV) [24] and the work function (Φ) of 5.3 eV measured in *p*-type Bi_2Te_3 when E_F is located at its valence-band maximum (VBM) [25]. As visualized in Fig. 2.4(a), E_{FS} ~ 4.9 eV is then situated deep inside the conduction band of Bi_2Te_3. Therefore, in our moderately *n*-type Bi_2Te_3 samples, $E_F < E_{FS}$, and donor-like native defects are predominantly generated during irradiation, shifting E_F up toward E_{FS}. Eventually, as shown in Fig. 2.3, the electron concentration saturates at n_{sat} when E_F reaches E_{FS}. Similar effects have been observed in other compound semiconductors with large electron affinity (χ) such as InN [26,27] and CdO [28,29]. On the other hand, to the best of our knowledge, the electron affinity of Bi_2Se_3 has not been experimentally determined yet. However, following the argument of ADM, we can use our results on the irradiation-induced saturation of electron concentration to determine its electron affinity.

A quantitative determination of the band offset can be made using the ADM under the condition that $E_F = E_{FS}$ when $n = n_{sat}$. The relationship between n and E_F is given by [30],

$$n = \frac{2}{8\pi^3}\iiint \frac{1}{1+\exp[(E_C - E_F)/k_B T]}\, d^3k\,, \tag{2.1}$$

where the electron energy E_C is related to wavevector k via the non-parabolic dispersion by solving Kane's two-band model [31],

$$E_C(k) = E_G + \frac{\hbar^2 k^2}{2m_0} + \frac{1}{2}\left(\sqrt{E_G^2 + 4E_P \cdot \frac{\hbar^2 k^2}{2m_0}} - E_G\right)\,. \tag{2.2}$$

Here E_P is an energy parameter related to the interaction momentum matrix element and approximately determined through the $k \cdot p$ result,

$$\frac{m_e^*}{m_0} \approx \frac{E_G}{E_P}\,. \tag{2.3}$$

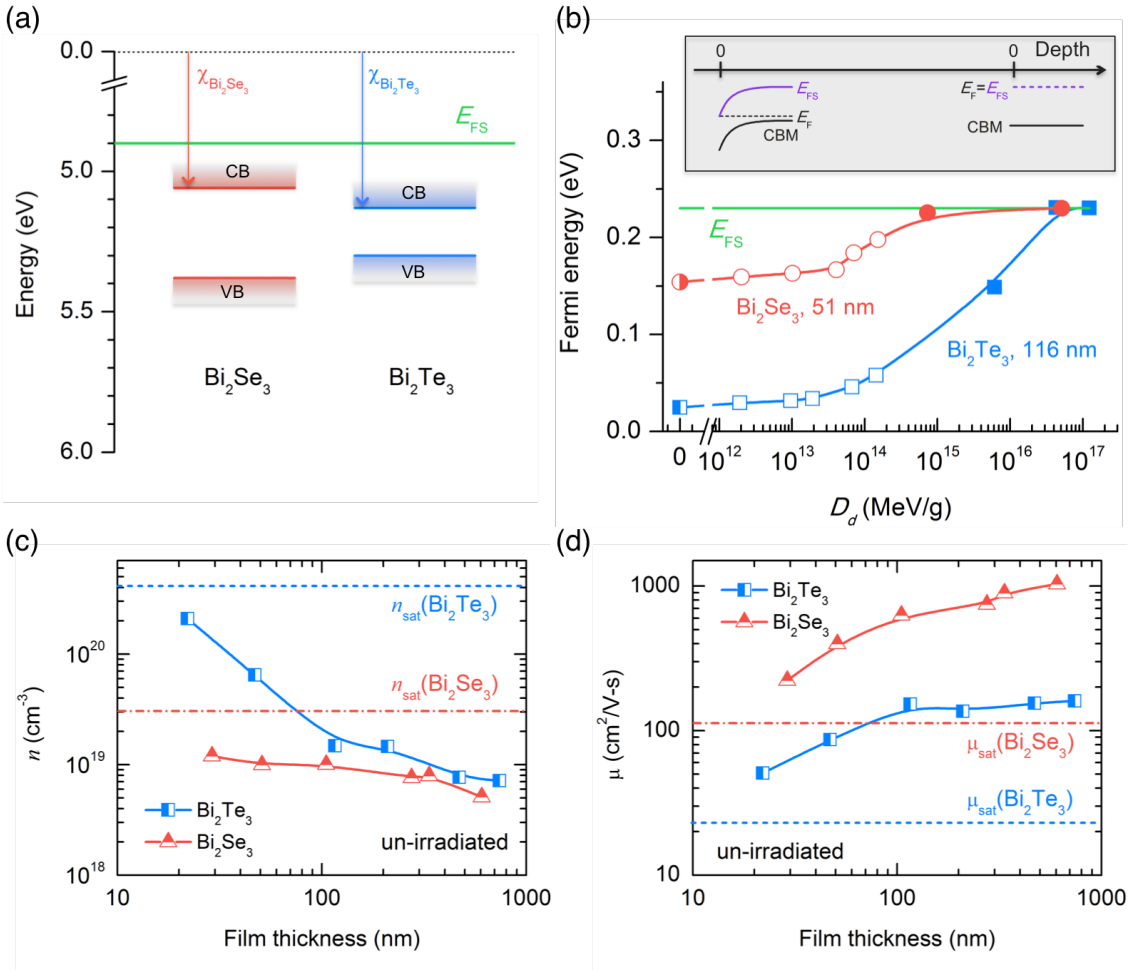

Figure 2.4. (a) Schematic representation of the Fermi stabilization position (E_{FS}), conduction band edge (CBM), and valence band edge (VBM) in Bi_2Se_3 and Bi_2Te_3. (b) Bulk Fermi level, measured from the CBM of Bi_2Te_3, moving toward E_{FS} as a function of D_d in Bi_2Se_3 and Bi_2Te_3. Inset shows schematics of band diagram along the depth of the samples, in the pristine (left) and Fermi-level-stabilized (right) TI films. All half-filled symbols correspond to the pristine values. Open and filled symbols represent values measured on He^{2+} and Ne^{+} irradiated films, respectively. (c) Electron concentration and (d) Carrier mobility of pristine (un-irradiated) TI films as a function of thickness. The saturated carrier densities and mobilities of Bi_2Te_3 and Bi_2Se_3 are obtained from Fig. 2.3.

We have also taken into account the conduction band renormalization effects at high n due to electron-electron interaction (ΔE_{e-e}) and electron-ionized impurity interaction (ΔE_{e-i}), given by the following expression [32]:

$$\Delta E_{e-e} = -\frac{2e^2 k_F}{\pi\varepsilon_S} - \frac{e^2 k_{\mathrm{TF}}}{2\varepsilon_S}\left[1 - \frac{4}{\pi}\arctan\left(\frac{k_F}{k_{\mathrm{TF}}}\right)\right], \tag{2.4}$$

$$\Delta E_{e-i} = -\frac{4\pi e^2 n}{\varepsilon_S a_B k_{\mathrm{TF}}^3}, \tag{2.5}$$

where $k_F = \left(3\pi^2 n\right)^{1/3}$ is the Fermi wave vector, $k_{\mathrm{TF}} = \left(2/\sqrt{\pi}\right)\left(k_F / a_B\right)^{1/2}$ is the Thomas-Fermi screening wave vector, ε_S is the static dielectric constant, and a_B is the Bohr radius (Å). We note that even at $n = n_{\mathrm{sat}} \sim 4 \times 10^{20}$ cm^{-3}, the renormalization-caused downshift of CBM is equal to only ~ 0.024 eV (hence E_G narrows to 0.146 eV) in Bi_2Te_3; this is due to the large ε_S of 290 [33] and to the multiplicity of the effective conduction-band valleys (N = 12) that include the secondary conduction band edges located very close to CBM [34]. With our measured n and literature value of $m_e^*/m_0 \sim 0.07$ in Bi_2Te_3, E_F relative to CBM is calculated as a function of D_d (Fig. 2.4(b)). The results are in quantitative agreement with ADM in that E_F stabilizes exactly at E_{FS} = 4.9 eV at high irradiation doses. Using the universality of E_{FS} among different materials, the same quantitative treatment is applied to Bi_2Se_3 with parameter values found in literature ($\varepsilon_S = 113$, $N = 1$, and $m_e^*/m_0 \sim 0.13$) [33,35,36], and the results are presented in Fig. 2.4. With this ADM approach, χ of Bi_2Se_3 is found to be ~ 5.06 eV, giving a VBM of ~ 0.08 eV lower than that of Bi_2Te_3, thus forming a type-I band offset between Bi_2Se_3 and Bi_2Te_3. This ADM-enabled quantitative treatment for Bi_2Se_3 (Bi_2Te_3) is in good agreement with the reported downward band bending of 0.13 eV (0.23 eV) caused by 2DEG when E_F in the bulk is located close to the CBM [13,37].

The successful application of ADM has an important implication for understanding of the origin of 2DEG on the TI surfaces. ADM predicts that E_F on natural surfaces of semiconductors is pinned at E_{FS} due to abundant surface defects and dangling bonds with similar origin and properties as the native bulk defects. This prediction has been confirmed by the observed dependence of Schottky barrier height on semiconductor band edge locations [38], as well as formation of 2DEG in accumulation layer in semiconductors having CBM below E_{FS} (e.g., InN [39] and CdO [28]). In both cases, there was a good agreement between the location of E_F on the surface and E_F in the bulk of heavily irradiated materials, potentially correlating the irradiation results to previously reported 2DEG formation by metal deposition [40].

In order to confirm the correlation between bulk and surface Fermi level stabilization energy, we have measured thickness dependence of the electron concentration and mobility measured in as-grown Bi_2Te_3 and Bi_2Se_3 films. As shown in Fig. 2.4(c) and (d), the electron concentrations increase with decreasing thickness and tend toward n_{sat} in the low thickness limit in both materials. In contrast, the mobilities

decrease with decreasing sample thickness but again they converge on the mobility values measured in thick, heavily irradiated materials. The electrical properties of thick samples are determined by the bulk with negligible contribution from the surface/interface layers. The bulk contribution decreases with decreasing film thickness, and in the limit of very thin samples, their electrical properties are determined by charge transport in the surface/interface layers. The observed clear tendency for both electron concentration and mobility to converge on the values of heavily irradiated thick samples confirms that E_F on the surface/interface of the studied TIs is pinned at E_{FS}, leading to accumulation of electrons and formation of the 2DEG.

2.4.1 Extension to ternary $Bi_2(Se_{1-x}Te_x)_3$ alloys

To further show the difference between Bi_2Se_3 and Bi_2Te_3, the ternary alloy system $Bi_2(Se_{1-x}Te_x)_3$ in the full composition range ($0 \leq x \leq 1$) was also investigated with He^{2+} and Ne^{+} irradiation. As shown in Fig. 2.5(a), all these alloys exhibit the stabilization of n at sufficiently high irradiation doses corresponding to the condition of $E_F = E_{FS}$. Figure 2.5 (b) illustrates the characteristic n_{sat} of these $Bi_2(Se_{1-x}Te_x)_3$ alloys with constant film thickness of ~ 60 nm. n_{sat} is strongly dependent on the composition x, increasing monotonically from 3×10^{19} in Bi_2Se_3 to 4×10^{20} cm^{-3} in Bi_2Te_3.

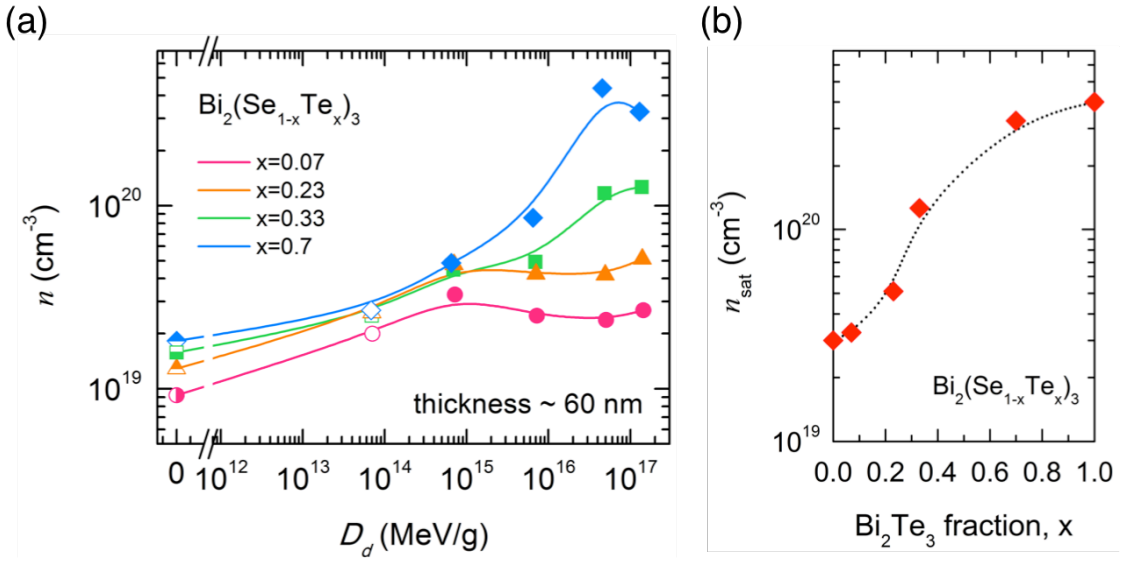

Figure 2.5. (a) Electron concentration as a function of D_d in a series of $Bi_2(Se_{1-x}Te_x)_3$ alloys with equal thickness of 60 nm. (b) Observed saturated electron concentration of $Bi_2(Se_{1-x}Te_x)_3$ as a function of x, the Bi_2Te_3 fraction.

2.5 Summary and remarks

In conclusion, high-energy particle irradiation was used to show that intentionally introduced native defects tend to stabilize the Fermi level in the conduction band in topological insulators Bi_2Se_3, Bi_2Te_3 and their alloys. The measured electron density and mobility saturate with the Femi level stabilization at high doses of irradiation, a trend that is also observed with decreasing thickness in pristine films. This indicates that the defects and dangling bonds abundant on the surface and/or interfaces will result in formation of electron accumulation layers and 2D electron gas. The finding explains difficulties in previous attempts to decouple electrical properties of TIs, and has important implications for potential applications that utilize the unique dispersion relation of the topological states on the surface of these materials.

Chapter 3

Enhancing thermoelectric performance of Bi_2Te_3 via defect engineering[2]

There is no abstract art. You must always start with something. Afterward you can remove all traces of reality.

PABLO PICASSO (1881 – 1973)

Thermoelectric materials have been heavily investigated over the past several decades for environment-friendly applications of solid-state energy conversion: heat to electricity and vice versa [41,42]. The figure-of-merit (ZT) of thermoelectric materials is given by $\alpha^2\sigma T/\kappa$, in which α is the Seebeck coefficient (thermopower), σ is the electrical conductivity, T is absolute temperature and κ is the thermal conductivity. Since α and σ are anti-correlated through the free carrier concentration (n), recent successes to enhance ZT have mostly relied on reduction of lattice thermal conductivity (κ_l) without significantly affecting the power factor ($\alpha^2\sigma$) [43]. This approach has achieved ZT of PbTe-SrTe compounds exceeding 2 at temperatures above 900 K by effectively scattering acoustic phonons with all-length-scale mean free paths [44].

[2] Reproduced in part with permission from J. Suh et al., "Simultaneous enhancement of electrical conductivity and thermopower of Bi_2Te_3 by multifunctionality of native defects," Advanced Materials **27,** 3681–3686 Copyright 2015 WILEY-VCH Verlag GmbH & Co. KGaA, Weinheim.

On the contrary, the best single-phase materials (*i.e.*, excluding superlattices [45]) available today for near-room-temperature thermoelectrics are Bi_2Te_3-based bulk alloys, and their best *ZT* is still around 1, *e.g.*, *n*-type $Bi_2Te_{2.7}Se_{0.3}$ with ZT_{max} ~0.9 [46] and *p*-type $Bi_{0.5}Sb_{1.5}Te_3$ with ZT_{max} ~1.2 [47]. The approach of phonon engineering has limited potential for these materials as their thermal conductivity is already low and does not have much room for further reduction [45,48]. Hence it is ultimately necessary to seek a breakthrough in materials engineering that would improve *ZT* beyond what is limited by the trade-off between α and σ, preferably with a single methodology. Though various experimental (*e.g.*, energy filtering in Bi_2Te_3/Bi_2Se_3 superlattices [49]) and theoretical (*e.g.,* hybridization by topological surface states [50]) approaches have been attempted or proposed, only α or σ, but not both, is effectively improved in these cases. The trade-off between α and σ originates fundamentally from the fact that a high α prefers a large asymmetry in electron population above and below the Fermi level, thus a rapid variation in the material density of states; this is opposite to the direction of increasing σ and *n*, which occurs typically as the Fermi level is displaced deep into the band where the density of states is relatively constant.

In this Chapter, we demonstrate a new way to drastically enhance thermoelectric properties of Bi_2Te_3 by utilizing native defects (NDs). We present a new, atomic-scale mechanism to break the trade-off between α and σ, simultaneously improving both for enhanced *ZT*. Such a unique combination of electrical and thermoelectric benefits originates from the multi-functionality of native point defects in Bi_2Te_3 acting as electron donors and electron energy filters. The presented results establish the importance of understanding and controlling point defects in thermoelectric materials as a venue to much improve their device performance.

3.1 Experimental section

3.1.1 Thin-film growth and structural characterization

Bi_2Te_3 thin-films with a wide range of thicknesses (11 nm ~ 1 μm) were grown by molecular beam epitaxy (MBE) on semi-insulating GaAs (001) substrates. The Bi_2Te_3 thin-films were grown using a dual chamber Riber 32 solid-source MBE system. The Bi and Te_2 fluxes were generated by standard effusion cells, and the structure and thickness of the films were monitored *in situ* by reflection high-energy electron diffraction. The growth step is initiated by heating an epi-ready semi-insulating GaAs (001) substrate to 600 °C for de-oxidation in the III-V MBE chamber. This was followed by deposition of a 100 nm GaAs buffer layer. This modified substrate was then transferred to the

chalcogenide MBE chamber through an ultra-high vacuum connection. The growth of the MBE film was initiated by the deposition of a series of monolayers of Te-Bi-Te-Bi-Te – a quintuple layer (QL) – in atomic layer epitaxy fashion at room temperature. The substrate was then gradually heated to 300 °C, and the MBE growth of Bi_2Te_3 was subsequently performed under Te-rich condition of T_{Te} (250 °C) < $T_{substrate}$ (300 °C) < T_{Bi} (~500 °C) with a Te:Bi beam equivalent pressure ratio ranging from 20:1 to 80:1. The films were grown layer-by-layer, with typical growth rates of 0.5–2 QL/min. Later, the compositions and thicknesses of the films were confirmed by Rutherford backscattering spectroscopy (RBS) before further experiments.

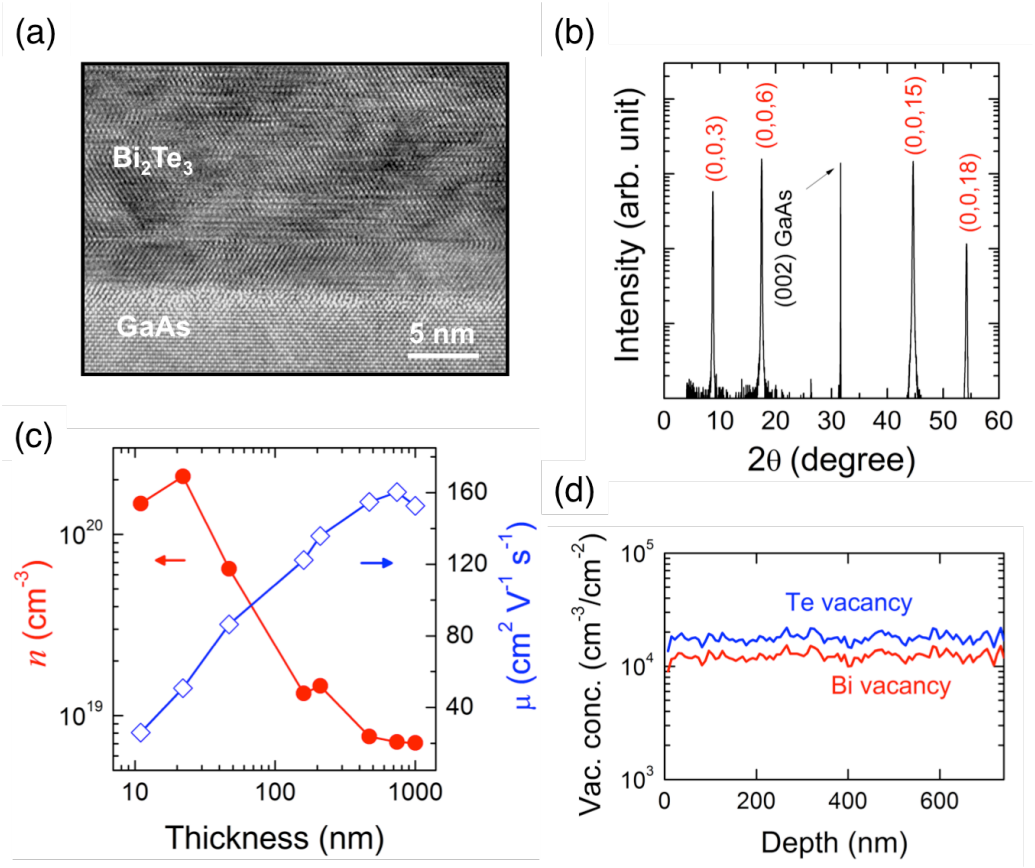

Figure 3.1. Characterization of pristine Bi_2Te_3 films. (a) Cross sectional HRTEM image and (b) XRD data of Bi_2Te_3 films grown by MBE on a GaAs (001) substrate. (c) Hall-effect determined carrier density and mobility as a function of thickness at room temperature. (d) The concentration of vacancies was calculated using SRIM for 740-nm thick Bi_2Te_3 film under 3 MeV alpha particles irradiation. SRIM predicts that the concentration of irradiation-induced defects is very uniform along the depth of films. As indicated by the units (cm^{-3}/cm^{-2}), the real vacancy concentration is given by this value multiplied with the irradiation dose (in units cm^{-2}), implying a linear dependence between them.

In Figure 3.1(a), the cross-section high-resolution transmission electron microscopy (HRTEM) image shows clean interfaces without amorphous phases, and shows highly parallel QLs. The crystallinity of the MBE films was further evaluated by X-ray diffraction (XRD) using the Cu $K_{\alpha 1}$ radiation line (Figure 3.1(b)). The XRD pattern clearly shows strong reflections from {003}-type lattice planes. This is a strong indication of the highly *c*-axis directional growth of the MBE films. The QL thickness was calculated from the XRD data, giving $d_{QL} = 1.014 \pm 0.005$ nm for Bi_2Te_3 that is consistent with the value of 1.016 nm for bulk Bi_2Te_3 [51].

3.1.2 Alpha particle irradiation

As presented in Figure 3.1(c), n decreases and carrier mobility (μ) increases monotonically with film thickness, and tends to saturate in thicker films, akin to those observed in Bi_2Se_3 MBE thin films [52]. In order to generate NDs, the samples were irradiated with 3 MeV alpha particles (He^{2+}) with doses ranging from 2×10^{13} cm^{-2} to 3×10^{15} cm^{-2}. The pristine samples were irradiated in an accumulated manner employing a high energy (3 MeV) He^{2+} beam with current between 35 and 100 nA generated by a NEC Pelletron tandem accelerator. The accumulated dose was monitored by measuring the total charge on the sample in an electrically isolated irradiation chamber. The ion beam was defocused to an area of 40 mm^2 maintaining a homogeneous ion fluence over the entire film, assuring the introduction of uniformly distributed NDs, both vertically and laterally.

3.1.3 Thermoelectric transport characterization

Electrical transport was measured by Hall effect using an Ecopia HMS-3000 system at room temperature. Seebeck coefficient was measured by a home-built thermopower measurement system. A differential 3ω technique was used to measure the cross-sectional thermal conductivity ($\kappa_\perp$) of the ND-engineered Bi_2Te_3 thin film with a thickness of 740 nm at various irradiation doses. Using the plasma-enhanced chemical vapor deposition (PECVD) technique, a 500 nm SiO_2 layer was simultaneously deposited on the top of both a pristine Bi_2Te_3 thin film, for electrical isolation, and a reference (identical semi-insulating GaAs (001)) bare substrate at 300 °C. Two identical 20 μm × 1500 μm gold line heaters were then patterned on the top of PECVD-grown SiO_2 layers using conventional photolithography. Since the thicknesses of the dielectric layer (500 nm) and Bi_2Te_3 film

(740 nm) are much thinner than the width of the patterned gold heater (20 μm), the through-thickness (along *c*-axis) heat conduction can be approximated as one-dimensional to better than 5% accuracy [53].

3.2 Defect generation and corresponding SRIM simulation

The projected range of these particles exceeds 8 μm in Bi_2Te_3, as calculated by Monte Carlo simulation using the Stopping and Range of Ions in Matter (SRIM) program (Figure 3.5 inset). Therefore, the He^{2+} ions completely pass through the entire film thickness, leaving behind NDs that are uniformly distributed in both lateral and depth directions. As predicted by SRIM, the primary NDs induced by irradiation are Bi (V_{Bi}) and Te (V_{Te}) vacancies and corresponding interstitials with average densities of 1.2×10^4 (for Bi) and 1.8×10^4 $cm^{-3}/ion \cdot cm^{-2}$ (for Te), respectively, that scale linearly with the irradiation dose (Figure 3.1(d)). We note that within the doses used, the materials are gently damaged with only point defects generated; no extended defects, surface sputtering, non-stoichiometry or amorphization is observed [54]. We also note that the substrate (semi-insulating GaAs) does not contribute to the electrical conductivity measured from the film. It is theoretically expected [55] and experimentally confirmed that the substrate remains electrically extremely insulating after the irradiation, with a sheet resistance orders of magnitude higher than that of the film.

3.3 Simultaneous enhancement of thermoelectric transport parameters (I): electrical conductivity

After the irradiation, σ of the Bi_2Te_3 increases for films with thickness between 47 and 740 nm, and this trend is more significant for thicker films (Figure 3.2(a)). Considering the multiple conduction channels (*e.g.,* surface and bulk) in Bi_2Te_3, this effect suggests that bulk transport, which is affected by the NDs, plays an important role in the electrical conductance in this thickness range. In contrast, very thin films are insensitive to irradiation, because surface conduction dominates and remains robust to irradiation. Hall effect measurements reveal that the enhanced σ is a combined effect of a monotonic increase in n and a non-monotonic change of μ (Figure 3.2(b) and (c)). The increase in n indicates that the irradiation predominantly introduces donor-like NDs, which are also considered as the primary reason for the unintentional n-type behavior of as-prepared Bi_2Te_3 [56,57].

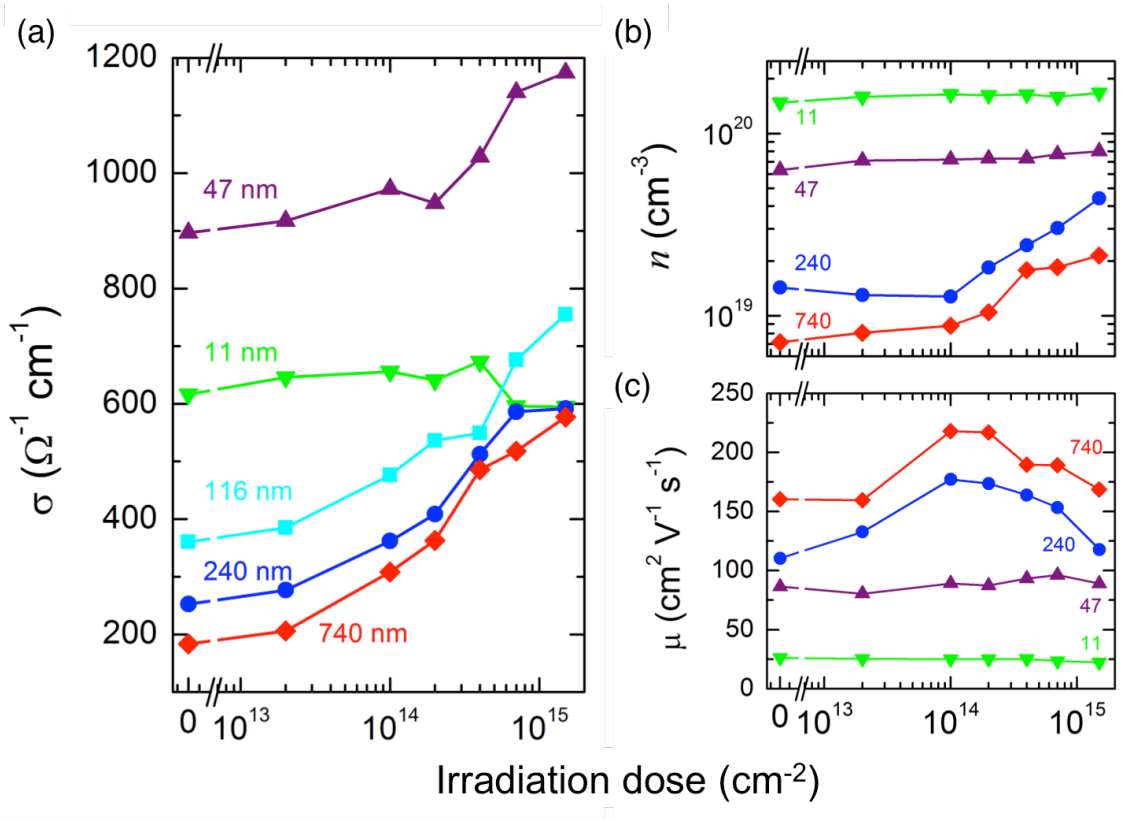

Figure 3.2. Electrical transport of ND-engineered Bi_2Te_3 thin films. (a) Electrical conductivity variation upon irradiation of films with different thicknesses. (b) Electron concentration and (c) Electron mobility of representative Bi_2Te_3 films as a function of irradiation dose, determined by Hall-effect measurement at room temperature.

3.3.1 Anomalous carrier mobility behavior: Bi-layer modeling

As shown in Figure 3.2(c), the mobility of thick films increases remarkably (by up to 50%) upon irradiation until an intermediate dose (~ 2×10^{14} cm^{-2}), then steadily decreases. For conventional semiconductors, it is believed that NDs produced by irradiation are charged Coulomb scattering centers, lowering the carrier relaxation time and thus the carrier mobility. Recent theoretical and experimental studies have shown that in addition to the bulk transport, Bi_2Te_3 exhibits significant surface or grain boundary transport, which are attributed to the topological insulator state [3] or to a surface accumulation layer [13,58].

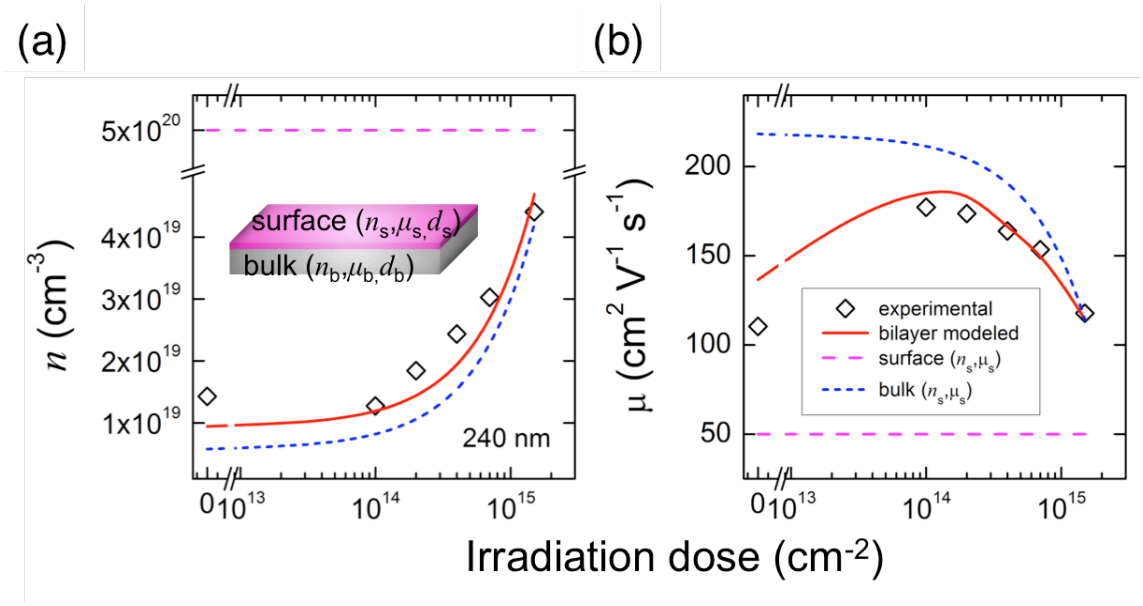

Figure 3.3. Bilayer Hall-effect modeling of Bi_2Te_3 films. Comparison of (a) electron concentration and (b) electron mobility between experimental data with bilayer modeled data for 240 nm film. Inset shows schematics of the two conduction channels of surface and bulk. Surface properties are assumed to be constant for all the films within the ranges of thickness and irradiation dose. Also, its thickness (d_s) is assumed to be ~3 nm, considering other contributions such as grain boundaries in the bulk as well as the surface roughness.

We propose that the irradiation-induced NDs cause the unusual mobility behavior of Figure 3.2(c) by modifying the relative contribution of conduction electrons between the bulk and the surface (including grain boundaries and specimen surface). Simplifying the system into two electrically conduction channels, surface and bulk, we modeled the dependence of carrier concentration and mobility on irradiation dose [59,60]. As illustrated in the inset of Figure 3.3(a), parallel electron transport was considered in the surface and bulk layers. With the relative contribution from each layer, effective (modeled) electron concentration (n^*) and mobility (μ^*) were determined using

$$n^* = \frac{\left[n_s\mu_s(d_s/d)+n_b\mu_b(d_b/d)\right]^2}{n_s\mu_s^2(d_s/d)+n_b\mu_b^2(d_b/d)}, \tag{3.1}$$

$$\mu^* = \frac{n_s\mu_s^{\,2}(d_s/d)+n_b\mu_b^{\,2}(d_b/d)}{n_s\mu_s\,(d_s/d)+n_b\mu_b\,(d_b/d)}, \tag{3.2}$$

where $n_s(n_b)$ and $\mu_s(\mu_b)$ are the electron concentration and mobility of surface (bulk) layer, respectively, and $d_s(d_b)$ is the thickness of surface (bulk) layer, and the total thickness, d, is given by $d = d_s + d_b$ [59]. The surface properties (n_s and μ_s) are inferred from Hall-effect

data of very thin films (11 ~ 22 nm) where surface contribution is dominant. Note that in this model n_s and μ_s are assumed to be not strongly affected by irradiation, *i.e.*, the irradiation generates more free electrons only in the bulk (increasing net n_b), as opposed to redistributing existing surface n_s to the bulk n_b. Indeed, in very thin films where the bulk conduction is insignificant, the measured n^* (Hall μ^*) is always dominated by n_s (μ_s), staying high (low) and nearly intact upon irradiation (Figure 3.2(b) and (c)).

Given that μ_s is insensitive to the irradiation and $\mu_s \ll \mu_b$ [21,54], n^* and μ^* were fitted to the experimental Hall-effect data at various irradiation doses. Such a bilayer model is in good agreement with the experimental data for films with various thicknesses, explaining both the monotonically increasing n^* and, in particular, non-monotonic variation of μ^* upon irradiation (see representative fitting in Figure 3.3). The irradiation-induced, drastic net increase in bulk electron density would shift the weight more toward bulk conduction, compared to the case in pristine films where surface conduction weighs more. Therefore, although μ_b slightly decreases upon irradiation, the measured μ^* shows an increase at intermediate irradiation doses, because after irradiation the higher-mobility bulk conduction plays a much more significant role than the surface conduction.

3.4 Simultaneous enhancement of thermoelectric transport parameters (II): thermopower

More importantly, while steadily increasing σ, the NDs at intermediate irradiation doses also improve the thermopower (α) of the thick Bi_2Te_3 films as seen in Figure 3.4(a). This simultaneous enhancement of α and σ is unusual, since in most cases α decreases and σ increases with increasing n. Normally, as n increases, the Fermi level E_F moves deeper into the band where the density of states is flatter, hence reducing the entropy carried by charges around E_F [61]. The simultaneous enhancement of α and σ is observed only in relatively thicker films (> 47 nm), which suggests that the measured thermopower is dominated by the bulk contribution that can be tailored by the NDs.

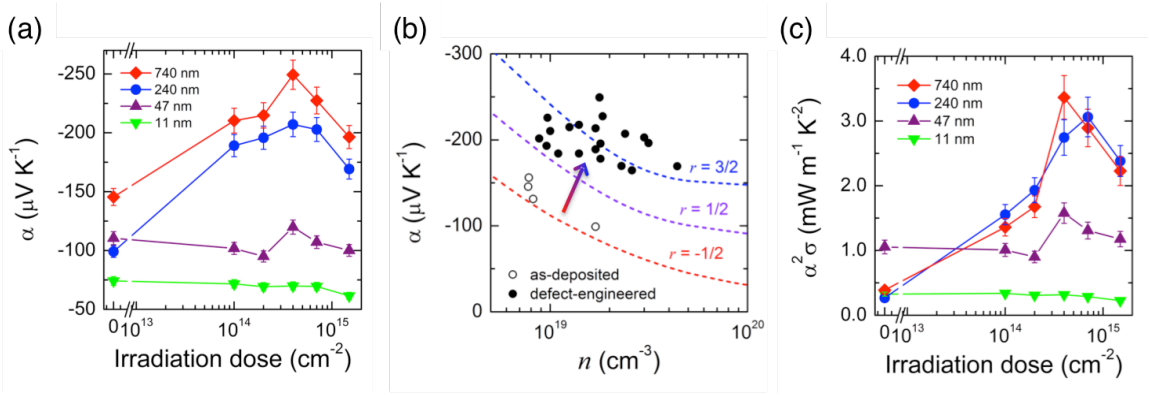

Figure 3.4. Enhancement of Seebeck coefficient and power factor by the NDs. (a) Variation of α upon irradiation. (b) α enhancement of irradiated Bi_2Te_3 films in the thick film regime (Pisarenko plot). The dotted lines show the results of calculated Seebeck coefficient with different scattering time index *r* ranging from phonon-scattering (-1/2) to ionized impurity-scattering (3/2). Here the rigorous Fermi-Dirac carrier statistics are used such that the calculation is valid across all concentrations ranging from non-degenerate to degenerate. The arrow indicates simultaneous increase of α and carrier concentration (*n*) of the films. (c) Thermoelectric power factor enhancement in the ND-engineered Bi_2Te_3 films.

3.4.1 Numerical calculation of thermopower

The definition of Seebeck coefficient (thermopower), α, can be derived from the solution to the steady-state Boltzmann transport equation under the relaxation time approximation as [62]

$$\alpha = \frac{2e}{\sigma}\int \frac{d^3k}{(2\pi)^3}\tau(k)\mathbf{v}_\mathbf{k}\mathbf{v}_\mathbf{k}\frac{\xi}{T}\left(-\frac{df^{(0)}}{d\xi}\right), \tag{3.3}$$

where $\sigma = 2e^2\int \frac{d^3k}{(2\pi)^3}\tau(k)\mathbf{v}_\mathbf{k}\mathbf{v}_\mathbf{k}\left(-\frac{df^{(0)}}{d\xi}\right)$ and $\xi = E(k)-\left(E_F - e\phi\right)$. Here e is the elementary charge, $\mathbf{v}_\mathbf{k}$ is the electron group velocity, E_F is Fermi energy, φ is electric potential and $f^{(0)}$ is the Fermi-Dirac carrier distribution function. The dependence of relaxation time τ on electron energy E follows $\tau(E(k)) \sim E(k)^r$, where the exponent $r = -1/2$ accounts for phonon dominated scattering mechanism, while $r = 3/2$ accounts for impurity dominated scattering mechanism. To calculate Seebeck coefficient as a function of carrier concentration, the Fermi level needs to be determined first based on the charge neutral condition, *i.e.*,

$$N_d - n(\phi, E_F) + p(\phi, E_F) = 0, \tag{3.4}$$

where N_d is the constant concentration of donors, n and p are the carrier population of the conduction and valence bands respectively. Setting the conduction band edge as the energy reference point, i.e. $\varphi = 0$, n can be calculated as

$$n(E_F) = \int \frac{\rho(E)dE}{1 + \exp\left[(E - E_F)/k_B T\right]}, \tag{3.5}$$

where $\rho(E)$ is the density of states for the conduction band. Here full Fermi-Dirac carrier statistics are used such that the calculation is valid across all concentrations ranging from non-degenerate to degenerate. Free hole concentration can be calculated in a similar way. In the degenerate doping limit, Equation (3.3) can be simplified to Equation (3.6) shown in the next Chapter.

3.4.2 Crossover into impurity scattering regime by irradiation-induced defects

In the relaxation time model, the thermopower in the degenerate doping limit is given by

$$|\alpha| \approx \frac{k_B}{e} \cdot \frac{\pi^2}{3} \cdot \frac{k_B T}{E_F} \cdot \left(\frac{3}{2} + r\right), \tag{3.6}$$

where r is the index of the electron relaxation time related to kinetic energy, $\tau(E) \propto E^r$ [63], and E_F is measured from the conduction band edge. Equation (3.6) not only predicts the ordinary decrease in α as n increases (through E_F), but also an increase in α when r increases. The former leads to the conventional wisdom of the inverse coupling between α and σ, while the latter allows it to be broken, as in our case. It is known that r varies from -1/2 for acoustic phonon scattering to 3/2 for ionized impurity scattering [63]. As shown in Figure 3.4(b), in pristine films, the measured α as a function of n follows the trend with calculation using r = -1/2, indicating that electrons are mostly scattered by phonons in these films. This is consistent with theoretical prediction that electrical transport in Bi_2Te_3 at similar carrier concentrations (~1×10^{19} cm^{-3}) is limited by phonon scattering [34], and is indeed reasonable considering its very large dielectric constant (ε_s = 290) [33]. However, the high density and multiple charge states of NDs introduced by irradiation as ionized impurities cause a transition of the scattering mechanism from phonon-dominated (r = -1/2) toward more impurity-dominated (r = 3/2); as a result, the thermopower is drastically enhanced, as indicated by the arrows in Figure 3.4(b). For the irradiated films, α starts to follow the calculated trend with r = 3/2. This transition is also

confirmed by the fact that the mobility μ of the pristine film becomes much higher when measured at low temperatures, while μ is less temperature-sensitive for irradiated films (Figure 3.5).

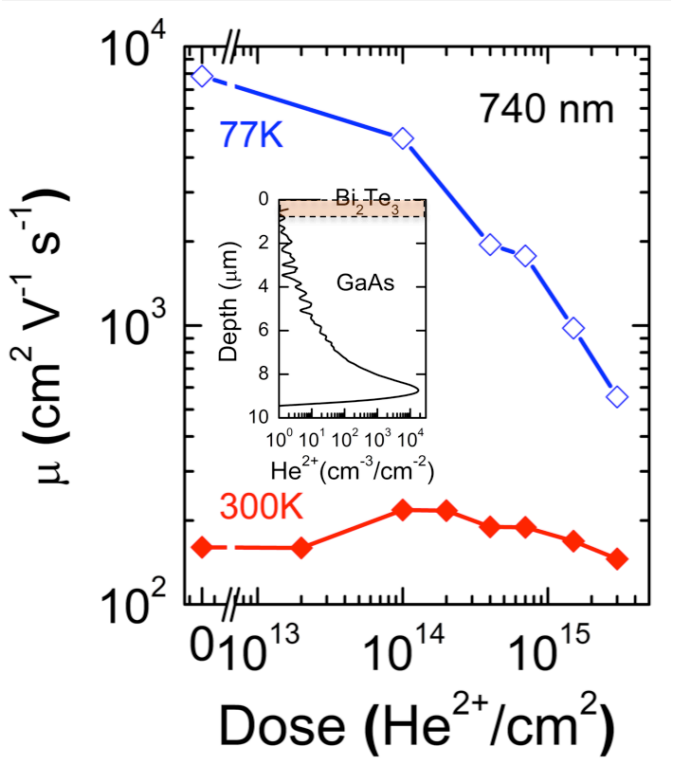

Figure 3.5. Low-temperature mobility of Bi_2Te_3 film. Comparison of carrier mobility determined at 77 K and 300 K for a 740 nm film as a function of irradiation dose. The mobility in the *pristine* film (740 nm thick) at 77 K is nearly two orders of magnitude higher than at 300 K. This difference becomes much smaller upon irradiation, suggesting that electrically active NDs (donors and compensated acceptors), as opposed to acoustic phonons, become the dominant scattering centers, which also increases the Seebeck coefficient. This supports the explanation in the main text of the simultaneous enhancements in both σ and α. Inset shows the depth distribution of the irradiation He^{2+} ions in the Bi_2Te_3 film and GaAs substrate determined by SRIM simulation.

3.4.2.1 Characteristics of native defects as charge scattering centers

Both native defects (NDs) and extrinsic chemical dopants enhance electrical conductivity of Bi_2Te_3 by donating more charge carriers. While they both behave as charged scattering

centers, their degree of ionized impurity scattering can be significantly different (hence different effects on Seebeck coefficient).

First, the scattering cross-section is much larger for NDs. For ionized impurity scattering, it is known that the cross-section is proportional to Z^2 as below:

$$\sigma \sim \left[\frac{1}{4\pi\varepsilon\varepsilon_0} \frac{Ze^2}{\frac{1}{2}m\upsilon^2} \right]^2, \tag{3.7}$$

where Z is the charge of the ionized defect center. It is widely known that NDs in semiconductors have multiple charge states depending on their Fermi level, and this also holds true for Bi_2Te_3 according to a recent computational investigation in Ref [57]. For instance, Te vacancies have the charge state of 2+. Recalling that high-energy particle irradiation normally generates Frenkel pairs (vacancy-interstitial), irradiation-induced NDs can have 4 times larger scattering cross-section compared to that of single charged extrinsic dopants such as iodine (*n*-type) and antimony (*p*-type).

Secondly, irradiation-induced NDs provide more charge scattering centers than chemical doping even when they donate the same number of free carriers. This is based on the fact that irradiation produces random damage consisting of donors and compensating acceptors. Although donor-like NDs (e.g., Te vacancies) are dominant, however acceptors (e.g., Bi vacancies) are also simultaneously generated as shown in Figure 3.1(d). Both types of NDs naturally act as charge scattering centers. The carrier scattering rate is given by $1/\tau = N\upsilon\sigma$ where N is the concentration of ionized scattering centers. In compensated semiconductors,

$$N = \frac{n}{Z} \frac{1+\theta}{1-\theta}, \tag{3.8}$$

where n is free carrier concentration and θ is the effective compensation ratio. For irradiated Bi_2Te_3, θ is estimated to be ~ 0.67 from our SRIM simulation, so N will be ~ 2.5 n. On the contrary, the uncompensated Bi_2Te_3 (e.g., I-doped Bi_2Te_3) will have $N \sim n$. Therefore, our finding of simultaneous enhancements in electrical conductivity and thermopower has never been observed in chemically doped Bi_2Te_3, in which the conventional wisdom of thermoelectrics governs.

3.4.3 Maximized power factor at intermediate irradiation dose

The ND-enabled decoupling of α and σ naturally leads to a significant increase in the thermoelectric power factor, $\alpha^2\sigma$, as shown in Figure 3.4(c). It reaches a peak value of 3.4 ± 0.3 mW m^{-1} K^{-2} for the 740 nm film at an irradiation dose of 4×10^{14} cm^{-2}, representing

an eight-fold enhancement from its pristine value. This peak power factor is a factor of 1.5 ~ 3 higher compared to recently reported values in binary Bi_2Te_3 [49,64].

3.5 Simultaneous enhancement of thermoelectric transport parameters (III): thermal conductivity

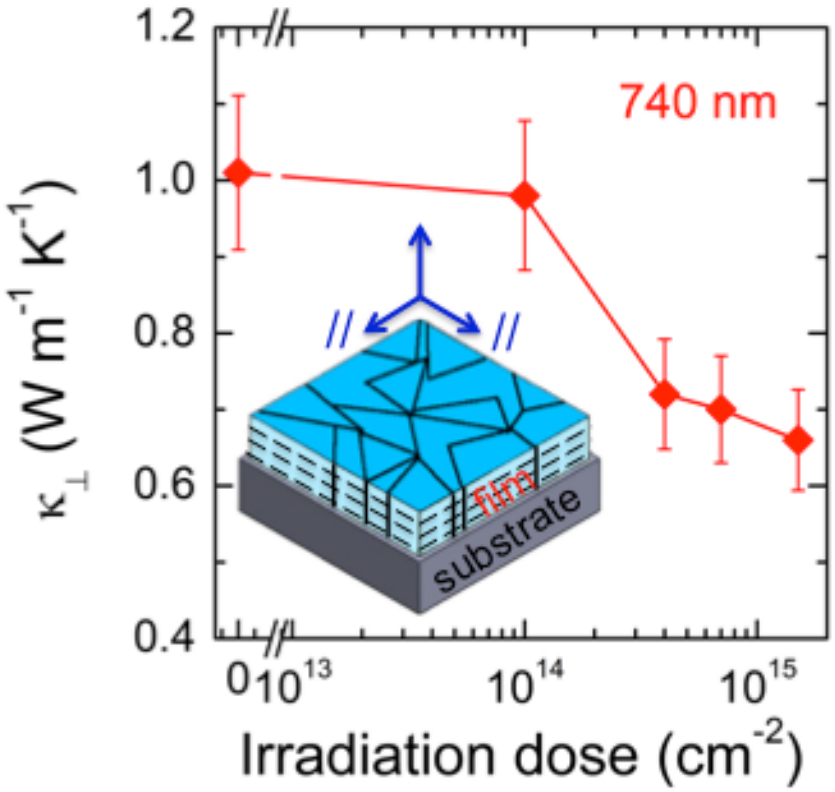

Figure 3.6. Cross-plane thermal conductivity of the 740 nm Bi_2Te_3 film upon irradiation. Inset illustrates the in-plane and cross-plane configuration of the textured film.

In addition, the effect of the NDs on the cross-plane (*c*-axis) thermal conductivity ($\kappa_\perp$), particularly in the thick Bi_2Te_3 films, was investigated using the differential 3ω technique (see the details in the following Chapter 3.5.1) [65]. We found that $\kappa_\perp$ decreases by up to 35% upon the irradiation as shown in Figure 3.6. It is noteworthy that the reduction in $\kappa_\perp$ is substantially stronger than the case if the NDs were replaced by conventional donor ions at the same concentrations (~3×10^{19} cm^{-3}, or ~0.1% of the atomic sites). This is

because a point defect's ability to scatter acoustic phonons goes as the square of the defect's relative deviation in mass, radius, and/or bonding strength [66]. These relative deviations are much stronger for the irradiation-introduced NDs (vacancies, anti-sites, and missing bonds) as compared to simple substitutional dopants [27]. As our measured κ is cross-plane ($\perp$), while the measured α and σ are in-plane (//), a rigorous evaluation of ZT is not within the scope of this Chapter due to the anisotropic transport. However, given the eight-fold enhancement in $\alpha^2\sigma$, it is safe to conclude that ZT is expected to be significantly enhanced accordingly, because κ is expected to only decrease upon the irradiation.

3.5.1 Details of 3ω measurement

Figure 3.7 illustrates these two 3ω samples, namely, "*sample*" (with Bi_2Te_3 film) and "*reference*" (without Bi_2Te_3 film). Figure 3.7(b) and (c) show the amplitude of the temperature oscillation in the pristine Bi_2Te_3 sample (ΔT_{sample}) and reference substrate ($\Delta T_{reference}$), calculated using

$$\Delta T = 2R\frac{dT}{dR}\frac{V_{3\omega}}{V_{1\omega}}, \tag{3.9}$$

where R, $V_{1\omega}$, $V_{3\omega}$ are the electrical resistance, 1ω voltage, and 3ω voltage of the gold heater, respectively, and dR/RdT is the temperature coefficient of resistance of the heater. The average temperature drop across Bi_2Te_3 film (ΔT_{film}) was determined using $\Delta T_{film} = \Delta T_{sample} - \Delta T_{reference}$, and the cross-plane thermal conductivity of film ($\kappa_{film,\perp}$) was calculated as

$$\kappa_{film,\perp} = \frac{Pd}{Lw\Delta T_{film}}, \tag{3.10}$$

where P is the amplitude of the heater power, d is the thickness of film, and L and w are the length and width of the heater, respectively. The representative temperature rise to determine $\kappa_{film,\perp}$ at 1.5×10^{15} cm^{-2} irradiation is shown in Figure 3.7(b).

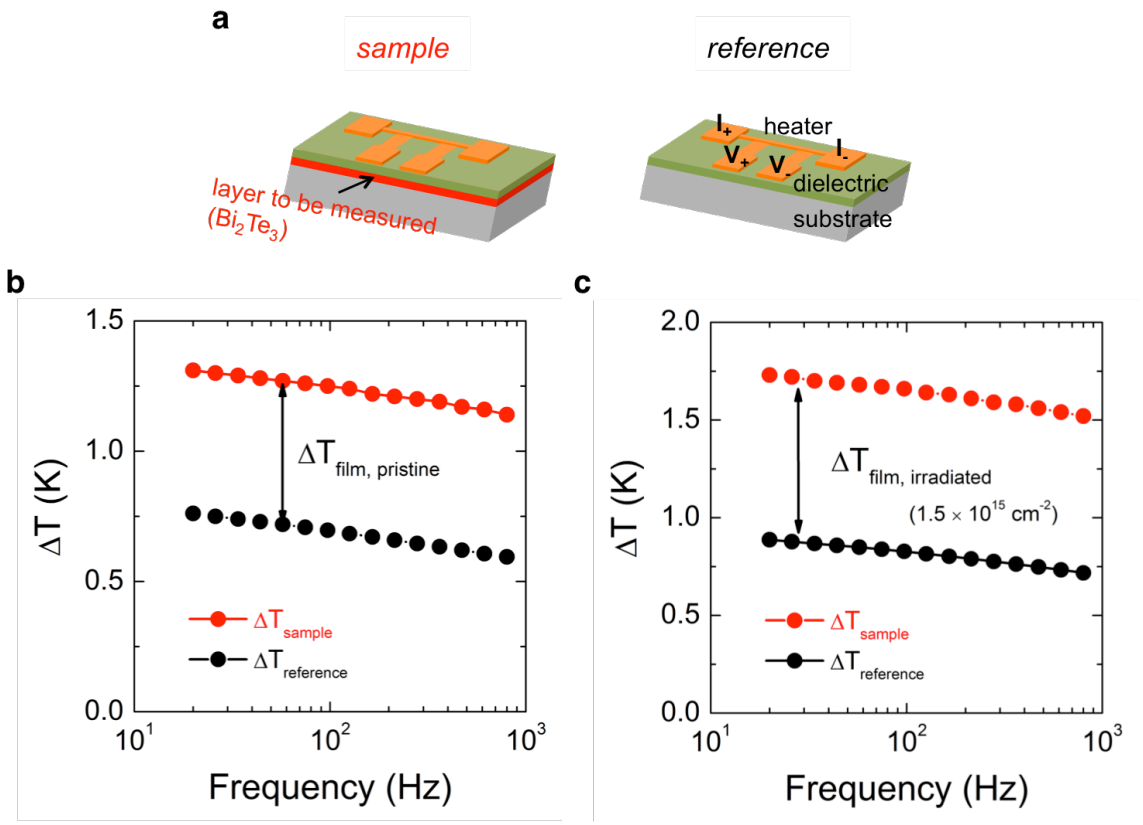

Figure 3.7. Thermal conductivity of Bi_2Te_3 film. (a) Schematic drawings of two types of specimen used for the differential 3ω measurement: "sample" and "reference". The only difference is the additional Bi_2Te_3 layer in the "sample". Determined temperature rise in the "sample" and "reference" (b) before and (c) after irradiation at a dose of 1.5×10^{15} cm^{-2}. Arrows indicate the temperature rise across the 740 nm Bi_2Te_3 film (ΔT_{film}).

Thermal conductivity was monitored by irradiating both the sample and reference substrate with the same dose. The $R(T)$ curve of every sample and reference was re-calibrated after every additional dosing step. We also note that due to the finite projected range of the alpha particles (see inset of Figure 3.5), the damage profile in the GaAs substrate will be slightly shallower in the "sample" as compared to the "reference" measurements. However, the following estimate shows that this effect should contribute only around 1% of additional uncertainty to the thermal conductivity of the film, and thus is simply neglected. The damaged region of GaAs can be approximated as a layer 1 µm thick that is either ~7 µm (sample) or ~8 µm (reference) below the top GaAs surface. For a comparable point-defect concentration of ~10^{19} cm^{-3}, the thermal conductivity of the damaged GaAs can be estimated as 40 W/m·K, as compared to 60 W/m·K for pristine GaAs. As a conservative estimate of the additional difference between these two samples,

we estimate the difference between one-dimensional conduction resistances of 1 μm of damaged and undamaged GaAs, and compare it to the thermal resistance of the 740 nm film at 1 W/m·K. On an area normalized basis this is 8.3×10^{-9} m^2 K/W compared to $7.4x10^{-7}$ m^2K/W, or only 1.1%.

3.5.2 Phonon mean free path of Bi_2Te_3

We then consider the range of phonon mean free paths (MFPs) that are important in bulk Bi_2Te_3 prior to irradiation. The lattice thermal conductivity of a bulk material can be expressed as

$$\kappa_{bulk} = \int \tfrac{1}{3} C v \Lambda_{bulk} \, d\omega, \tag{3.11}$$

where ω is the phonon frequency, C is the volumetric specific heat capacity per unit frequency, v is the group velocity, Λ_{bulk} is the bulk MFP, and each term in the integrand is frequency-dependent. For simplicity we use a Born-von Karman dispersion relation and average the transverse and longitudinal polarizations. Due to its low Debye temperature of 165 K [67], at 300 K Bi_2Te_3 is well into the Dulong-Petit regime of constant heat capacity. In bulk Bi_2Te_3 of comparable doping [68,69], Λ_{bulk} at room temperature is dominated by umklapp scattering both in-plane and cross-plane. As a result, $\kappa_{bulk} \propto T^{-1}$, consistent with umklapp-limited transport and inconsistent with other scattering mechanisms such as boundaries and point defects. Thus, the bulk MFP can be approximated as $\Lambda_{bulk}^{-1} \approx \frac{B\omega^2 T}{v}$ [70], where the free parameter B is determined by substituting this bulk MFP into Equation (3.11) and fitting the model to experimental data for the in-plane [68] and cross-plane [69] lattice thermal conductivities. The resulting values are $B_{//} = 4.58\times10^{-18}$ s/K (in-plane) and $B_{\perp}=1.12\times10^{-17}$ s/K (cross-plane). The other parameters used in the model are the lattice constants [68] ($a_{//}$ = 0.4383 nm, $a_{\perp}$ = 3.0487 nm) and average sound velocities ($v_{s,//}$ = 2090 m/s, $v_{s,\perp}$ = 2017 m/s) [51].

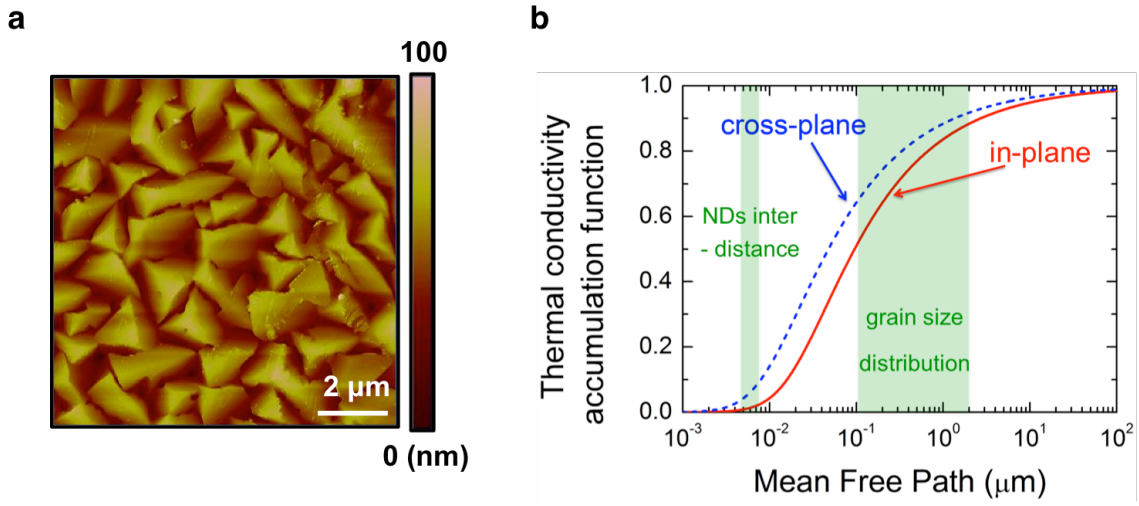

Figure 3.8. (a) AFM image of Bi_2Te_3 films grown by MBE on a GaAs (001) substrate displaying grains ranging from 100 nm to 2 μm and oriented in the film plane. (b) Calculated thermal conductivity accumulation function of non-irradiated Bi_2Te_3. The shaded region represents the range of grain sizes observed in the films.

The resulting accumulation functions [71] for bulk Bi_2Te_3 at 300 K are shown in Figure 3.8, along with typical distribution of grain sizes from ~100 nm to 2 μm in the films. The calculation shows that the additional scattering by 2 μm grains would have only a modest impact on thermal conductivity, since 88% (in-plane) and 92% (cross-plane) of κ_{bulk} is carried by phonons with MFPs shorter than 2 μm. However, for 100 nm grains, effect of grain boundary scattering would be substantial, and would impact $\kappa_{//}$ more than $\kappa_{\perp}$, since the accumulation function at 100 nm is smaller in plane (51%) than cross plane (64%). Assuming that the in-plane and cross-plane grain sizes are similar, this calculation also shows that $\kappa_{//}/\kappa_{\perp}$ should become slightly more isotropic as grain boundary scattering becomes increasingly important.

3.5.3 Estimation of bounds of in-plane *ZT*

For bulk crystalline Bi_2Te_3 at similar carrier concentrations, it is well known that $\sigma_{//}/\sigma_{\perp} \approx 5.0$ and $\kappa_{//}/\kappa_{\perp} \approx 2.0$ [22]. Using the Wiedemann-Franz law [72], the corresponding ratio of phonon thermal conductivities is $\kappa_{//,phonon}/\kappa_{\perp,phonon} \approx 1.7$. As compared to this reference data, the $\kappa_{//}/\kappa_{\perp}$ ratio of the present film samples will differ due to several effects. First, we note that the range of phonon mean free paths (MFPs) of

the bulk materials is estimated to span from ~10 nm to ~1 μm, with the MFPs longer in-plane than cross-plane by a factor of ~2. Phonon scattering by grain boundaries affects transport in both directions; but because these grains are textured, $\kappa_{//,phonon}$ should be reduced more than $\kappa_{\perp,phonon}$ due to the longer in-plane MFPs, and it is estimated that about 50% of the in-plane-propagating phonons are scattered at MFPs comparable to the grain sizes in the films (see Figure 3.8(a)).

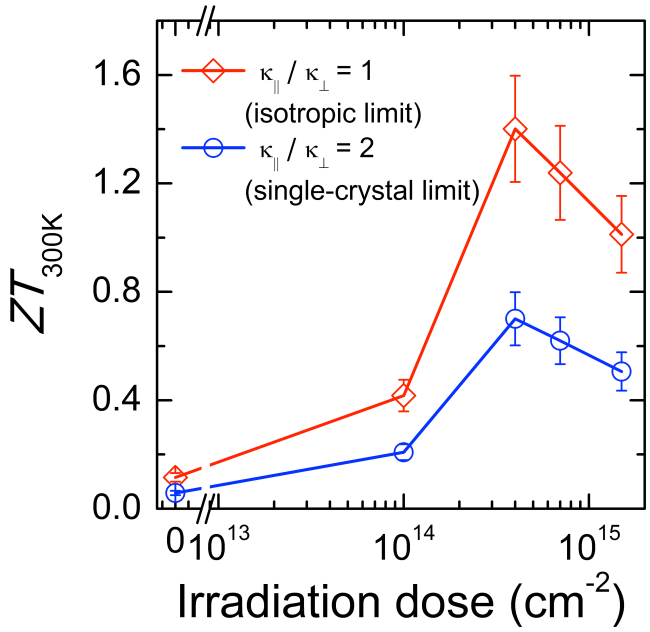

Figure 3.9. In-plane *ZT* of the irradiated film for anisotropy ratios of 1 (anisotropic, or random polycrystalline limit) and 2 (single-crystal limit), respectively. The real *ZT* value should be in between these two scenarios. In both scenarios the maximum *ZT* is enhanced approximately by an order of magnitude compared to the pristine film.

Similarly, the strong impurity scattering also tends to reduce $\kappa_{//,phonon}$ more than $\kappa_{\perp,phonon}$, as seen in measurements of Bi_2Te_3 [22] and modeling of In_4Se_{3-x} [73]. At the optimal irradiation dose, the NDs distribute over an average distance of ~5 nm, which is much smaller than the median phonon MFP. Overall the $\kappa_{//}/\kappa_{\perp}$ ratio of the 740 nm film should be less than that of single-crystal limit of 2.0 [22]. The resulting in-plane *ZT* at room temperature is calculated in Figure 3.9 for two limiting cases of $\kappa_{//}$. It can be seen that the *ZT* of the optimally irradiated films is at least 0.7 (using the most conservative value of $\kappa_{//}/\kappa_{\perp} = 2.0$), and potentially reaches 1.4 in the isotropic limit ($\kappa_{//}/\kappa_{\perp} = 1.0$).

Both values correspond to an enhancement by a factor of ~ 10 in *ZT* compared to the pristine-film values.

3.6 Summary and remarks

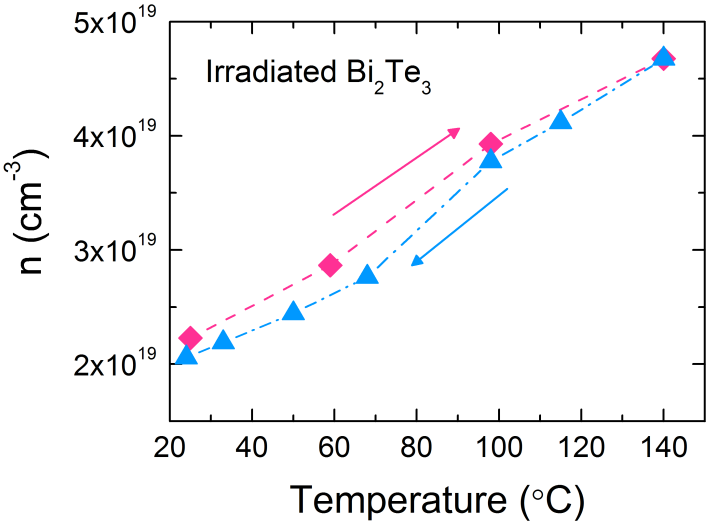

Figure 3.10. Carrier concentration of irradiated Bi_2Te_3 across a practical temperature range. The carrier concentration of 740 nm thin-film was measured during heating (red) and cooling (blue) with a ramping rate of 10 K/min. At each temperature point, the time spent on waiting for temperature stabilization and the Hall measurement is about 10 minutes, such that the total time of a full cycle is about 90 minutes.

To summarize, irradiation-induced NDs drastically enhance thermoelectric properties in Bi_2Te_3 by decoupling the three key thermoelectric parameters and simultaneously modifying all of them toward the desired direction. This is enabled by the multiple functionality of the NDs acting beneficially as electron donors, energy-dependent charge scattering centers, and phonon blockers. Our results suggest that a significant improvement of the thermoelectric performance can be achieved through a judicious control of the ND species and their density by post-growth processing with high-energy beams. As the NDs are expected to be generated and behave in the similar way in a wide range of narrow-bandgap semiconductors (*e.g.*, observed in InN [74] and InAs [75]), it is possible to extend this method to improve the figure-of-merit of other materials in conjunction with other widely utilized techniques such as alloying and nano- and hetero-structuring. Although irradiation cannot be directly applied to bulk materials due to

limitation in irradiation projection range (~ 10 μm), our approach is of practical importance because thin film thermoelectrics could play an important role in on-chip cooling [76]; in addition, our approach can be used in complementary to existing nanotechnology to scale up in bulk thermoelectrics. For instance, nano-objects (such as Bi_2Te_3 nanowires, particles and nanoplates) can be irradiated, and then pressed into bulk or assembled into bulk using a polymer matrix, as demonstrated by N. E. Coates *et al.* [77]. Also, to extend our understanding on thermoelectics, another novel observation of nanoscale thermoelectric phenomenon at metal-insulator domain walls in a single vanadium dioxide nanobeams is discussed in Appendix A.

Chapter 4

Defects activated photoluminescence in two-dimensional semiconductors[3]

In Science, 'fact' can only mean 'confirmed to such a degree that it would be perverse to withhold provisional assent.' I suppose that apples might start to rise tomorrow, but the possibility does not merit equal time in physics classrooms.

STEPHEN J. GOULD (1941 – 2002)

In semiconductors, lattice point defects such as vacancies and interstitials can act as very efficient traps for electrons, holes and excitons, and strongly influence transport and optical properties of the host material. Excitons bound to defects, if recombine radiatively, lead to light emission at energies lower than the band-to-band optical transition energy. Such interactions become stronger in reduced dimensionalities due to tighter localization of the electron wave function. For example, in three dimensions (3D) within the hydrogenic defect model, shallow defects bind electrons at a ground-state binding energy equal to $13.6\ \mathrm{eV} \times m^* / \varepsilon_r^2$, where $m^\star$ is the effective mass and ε_r is relative dielectric constant. This is increased to $54.4\ \mathrm{eV} \times m^* / \varepsilon_r^2$ in two dimensions (2D) simply due to the dimensionality effect [78]. Similarly, the binding energy and recombination

[3] Reproduced in part with permission from J. Suh et al., "Defects activated photoluminescence in two-dimensional semiconductors: interplay between bound, charged, and free excitons," Scientific Report **3,** 2657 Copyright 2013 Nature Publishing Group.

dynamics of Wannier and Frenkel excitons are expected to be drastically different going from 3D to 2D [79-81]. The escalated binding energy means stabilization of bound excitons and their emission features at higher temperatures, pointing to a potentially useful way to tailor optical properties of 2D semiconductors.

Although the understanding of point defects in conventional 3D semiconductors is well established and the defects database is relatively complete, physics and behavior of point defects in 2D semiconductors, such as the newly emerging monolayer semiconducting transition metal dichalcogenides (TMDs), have remained an unexplored field. In this chapter we report the effects of anion vacancies, the dominant point defect species, on photoluminescence (PL) and Raman spectra of monolayer TMDs. Since these materials become direct-bandgap semiconductors with relatively high PL intensity in the monolayer limit [82], the defect effects can be easily monitored optically. We find that irradiation with MeV alpha particles or thermal annealing at sub-decomposition temperatures introduce anion vacancies in monolayer MoS_2, $MoSe_2$, and WSe_2, where the vacancy density can be controlled by the irradiation dose or annealing time. These defects introduce a new emission peak at ~0.15 to 0.25 eV below the free-exciton PL peak, and its intensity is enhanced as the defect density is increased. Moreover, the overall PL intensity also increases at higher defect densities, and as such, the defective material becomes more luminescent compared to pristine monolayers. Surprisingly, these effects are absent when measured in vacuum, suggesting that the interaction between ambient gas molecules and the defect sites play a significant role in the process. Our density functional theory (DFT) calculations show that these anion vacancies create energy levels approximately 0.2 eV below the band edge, and gas molecules can be physically adsorbed at the defect sites with relatively large charge transfer, which electron-depletes the material.

4.1 Optical characterization of 2D semiconductors

4.1.1 Sample preparation, micro-PL/Raman, and AFM

Monolayer MoS_2, $MoSe_2$, and WSe_2 flakes were mechanically exfoliated from bulk crystals (2D Semiconductors and SPI) onto 90 nm SiO_2 (MTI corporation, resistivity 0.001 ~ 0.1 Ω-cm) where a relatively high contrast can be observed at the flakes [83]. The monolayers were identified using atomic force microscopy (AFM), Raman, and PL measurements. Raman/PL measurements were performed using a Renishaw micro-PL/Raman system. The laser beam (wavelength 488 nm) was focused onto the sample (spot diameter of ~1–2 μm) using excitation power up to 5–10 mW unless stated otherwise in this Chapter. The part of PL/Raman measurements were performed in a home-made vacuum chamber

pumped down to ~10^{-4} Torr using a turbo-molecular pump. High purity (99.9995%) N_2 gas was introduced into the chamber regulated by flow meters and the pressure was measured by a vacuum gauge.

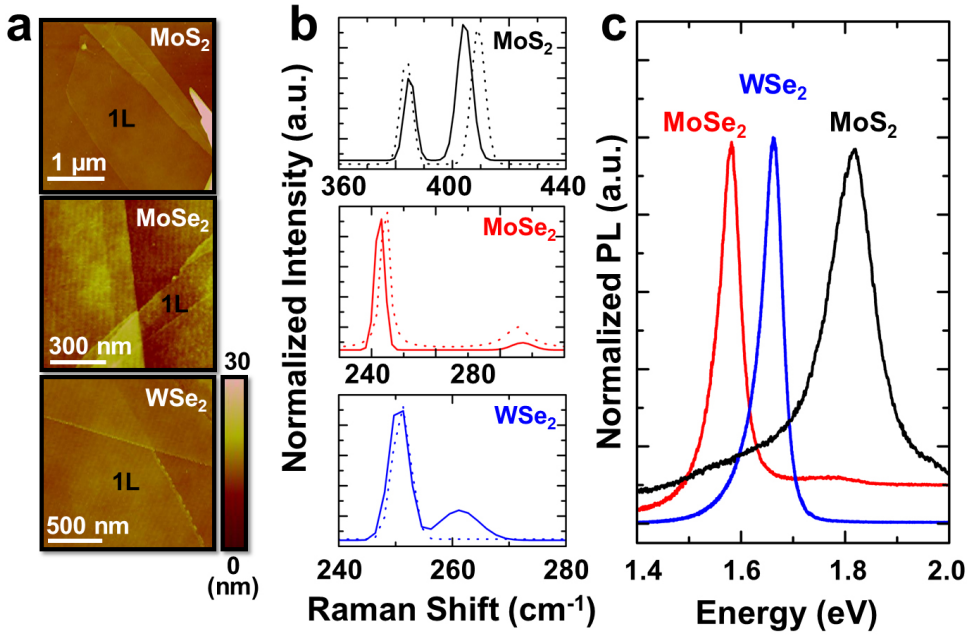

Figure 4.1. (a) AFM images taken on monolayer MoS_2, $MoSe_2$, and WSe_2. (b) Raman spectra measured on monolayer MoS_2, $MoSe_2$, and WSe_2, where the solid and dashed curves correspond to monolayers and few-layers, respectively. (c) Room-temperature normalized PL for monolayer MoS_2, $MoSe_2$, and WSe_2.

AFM measurements, performed using Veeco Multimode AFM in the tapping mode, on monolayers yield a height of ~0.7 nm corresponding to the thickness of a single unit cell (Figure 4.1(a)). From the bulk to monolayers, the out-of-plane Raman mode (A_{1g}) softens and the in-plane mode (E_{2g}) stiffens for MoS_2 [84] and $MoSe_2$ [85,86], whereas for WSe_2 [87], the degenerate A_{1g} and E_{2g} modes in the bulk split by 12 cm^{-1} in the monolayer as a result of broken degeneracy (Figure 4.1(b)). The PL signal is greatly enhanced by orders of magnitude from the bulk to monolayer due to the indirect to direct bandgap transition, consistent with previous reports [82,85,88]. At room temperature, monolayer MoS_2, $MoSe_2$, and WSe_2 show a strong PL peak at 1.84 eV, 1.56 eV and 1.65 eV, respectively (Figure 4.1(c)).

4.1.2 Alpha particle irradiation and thermal annealing

The exfoliated monolayer samples were irradiated employing a high energy (3.04 MeV) He^{2+} beam with current around 35 nA generated by a Pelletron tandem accelerator. The ion beam was defocused to an area of 32 mm^2 maintaining a homogeneous ion fluence over the entire flake. The accumulated dose was monitored by Faraday cups inside the irradiation chamber to create different densities of point defects, and the samples were cooled down to the lowest attainable temperature in our system (77 K) for PL and Raman measurements. Before and after the irradiation, the sulfur to molybdenum (S/Mo) atomic ratio was monitored using nano-Auger electron spectroscopy (nano-AES). We find that the S/Mo ratio decreases slightly (Figure 4.2(a)), implying that the irradiation induces S vacancies in the 2D crystal, consistent with earlier results [89]. After the irradiation, the full-width-at-half maximum of the Raman peaks slightly broadens (Figure 4.2(b)) due to relaxation of the Raman selection rule at the defects.

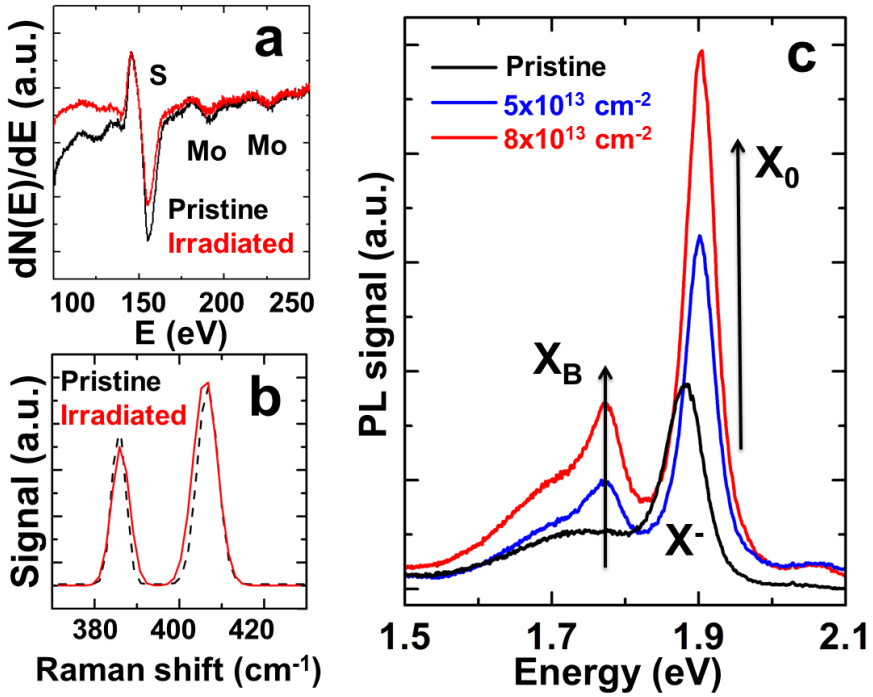

Figure 4.2. (a) Nano-Auger spectrum taken on a monolayer MoS_2 before and after irradiation with a particles at a dose of 8×10^{13} cm^{-2}. (b) Raman spectrum of the same. (c) PL spectrum for pristine and irradiated monolayer MoS_2 at the shown irradiation doses. The PL was taken at 77 K in N_2 (50 Torr) environment with a constant laser excitation power. The irradiation-caused enhancement in bound exciton (X_B) and free exciton (X_0) emission intensity is indicated.

For thermal annealing, the samples were heated to 500 °C at 30 °C/min rate and the temperature was hold at 500 ± 0.5 °C for 30 minutes. The annealing was performed in a 2-inch quartz tube in vacuum (30 mTorr base pressure). Prior to the annealing, the quartz tube was cleaned at 1000 °C in H_2 gas (2 Torr) overnight. Its effect will be discussed in the following section.

4.1.3 Interplay between bound, charged, and free excitons

At 77 K, the as-exfoliated MoS_2 monolayers display a strong PL peak at 1.90 eV corresponding to the direct bandgap at the K symmetry point. Upon the alpha particle irradiation at different doses, the 77 K PL spectrum changes significantly as shown in Figure 4.2(c) and these changes are summarized as follows: (i) a new PL peak appears at 1.78 eV and the integrated intensity of this peak increases with the irradiation dose; and (ii) the integrated intensity of the main PL line at 1.90 eV increases by ~3 times while the PL peak position shifts to higher energy by ~20 meV. The Stopping and Range of Ions in Matter (SRIM) calculations estimate that 7.5×10^{23} vacancy/cm × ion is generated on MoS_2 upon the alpha particle irradiation, and this corresponds to 6×10^{11} cm^{-2} defect density, or approximately one defect per 100 unit cells, for 8×10^{13} cm^{-2} irradiation dose. We note that here the PL was all measured in the presence of N_2 gas (~50 Torr), and the effect of N_2 will be discussed later. The small blueshift and enhancement in the main PL intensity bear much resemblance with the previously reported transition from charged exciton (X^- or eeh) to neutral free exciton (X_0 or eh) in 2D systems, such as 2D electron gas (2DEG) heterostructures [90] and more recently on monolayer TMDs [79-81]. In these cases, the charged to neutral exciton transition is associated with charge depletion [79-81] or charge localization [90] which stabilizes (destabilizes) neutral (charged) excitons. In accord with these studies, we attribute the observed blueshift to irradiation-induced defect sites interacting with N_2 molecules, resulting in depletion and localization of charge carriers in the monolayer TMDs. Such effects will be discussed more in detail later.

Next, we focus on the new peak at 1.78 eV (Figure 4.2(c)). Since this PL peak appears after the irradiation and its intensity increases at higher doses, we attribute it to radiative recombination of bound excitons (X_B), i.e. neutral excitons (X_0) bound to defects. To probe this more, we also introduced the defects by thermal annealing in vacuum. Here, monolayers were annealed ~100 °C below their thermal decomposition temperature (~600 °C), and this process is known to create S vacancies in MoS_2 [91]. After the annealing, the PL spectrum also displays a defect-induced bound exciton peak at ~1.78 eV (Figure 4.3(a)), except that the peak appears relatively stronger and broader

than in the irradiated samples, possibly due to a higher density of point defects and defect clusters created by annealing. It is expected that vacancies generation by particle irradiation is a series of highly non-equilibrium, random and isolated events, while thermal annealing is much slower and may facilitate formation of vacancy clusters with different configurations. These defect complexes with different clustering configurations may have different exciton binding energies, thus broadening the observed defect PL peak.

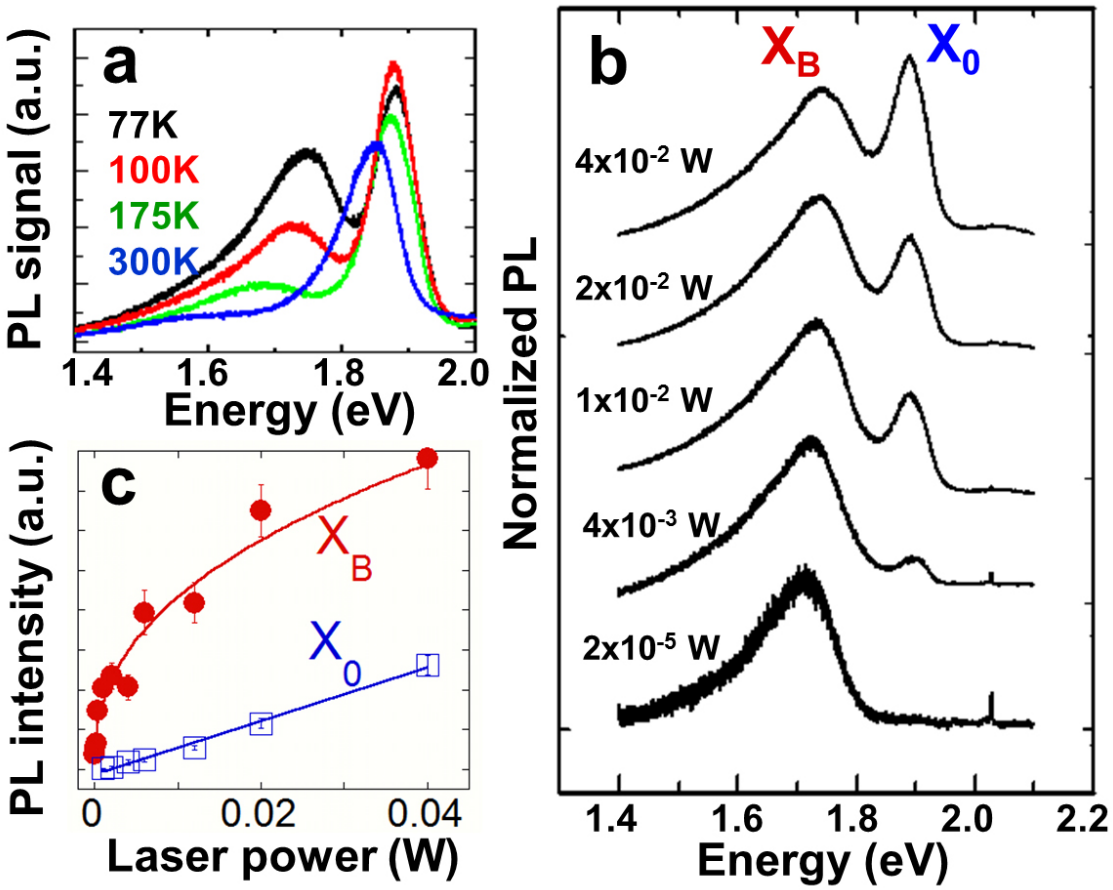

Figure 4.3. (a) PL spectrum measured over the temperature range from 77 K to 300 K of a monolayer MoS_2 after being annealed to 500 °C. (b) The PL at 77 K with different excitation laser power. Both a and b were taken in the presence of N_2 gas (50 Torr). (c) Integrated PL intensity of bound exciton (X_B) and free exciton (X_0) as a function of excitation laser power.

Further confirmation on the defect origin of the 1.78 eV peak comes from its excitation power dependence (Figure 4.3(c)). Since the X_B is associated with excitons bound to defects, the PL intensity of X_B is expected to saturate at high excitation power intensities when these defects are fully populated with excitons [92]. Consistent with this, the intensity of X_B exhibits a sub-linear laser power dependence with a tendency to saturate at high excitation powers, whereas the free exciton intensity (X_0) scales linearly without any sign of saturation (Figure 4.3(b) and (c)). As a result, the overall PL spectrum is mostly dominated by the defect peak, X_B, at low excitation intensities, and the X_0 line becomes observable only at high excitation intensities (Figure 4.3(b)).

4.1.4 Impact of physi-sorbed gas molecules

Next, we consider the effects of temperature and interaction with ambient gas molecules on the PL spectrum of defective monolayers. First, we note that the X_B peak is prominent at low temperatures or low excitation powers (Figure 4.3(a) and (b)). It becomes weaker as the temperature is increased and completely disappears above 250 K. At room temperature, both pristine and defective monolayers exhibit high optical quality with a strong, single PL peak associated with the band-to-band optical transition at the K point. Therefore, we conclude that in opposite to conventional wisdom believed in this new field of 2D semiconductors [93,94], optical quality at room temperature (PL intensity and sharpness) cannot be used as criteria to assess the crystal quality of the monolayers. Indeed, the defective monolayers yield even stronger PL intensity at room temperature (Figure 4.4(a)). However, the PL spectrum at 77 K immediately tells the difference between the pristine and defective monolayers (Figure 4.2(c)).

The PL spectra discussed so far were all recorded in the presence of N_2 gas, regardless of the measurement temperature (300 K or 77 K). Interestingly, when measured in vacuum, the aforementioned defect peak (X_B) in the PL spectrum disappears at both room and low temperatures (Figure 4.4(a) and (b)). We also note that the occurring of the defect PL peak was instantaneously reversible when the chamber is purged with or pumped out of N_2. This implies that the interaction between the defect sites and the N_2 gas molecules is weak (physi-sorbed), but dictates the optical emission of the material. The above results are discussed in detail in conjunction with first-principles calculations shown below.

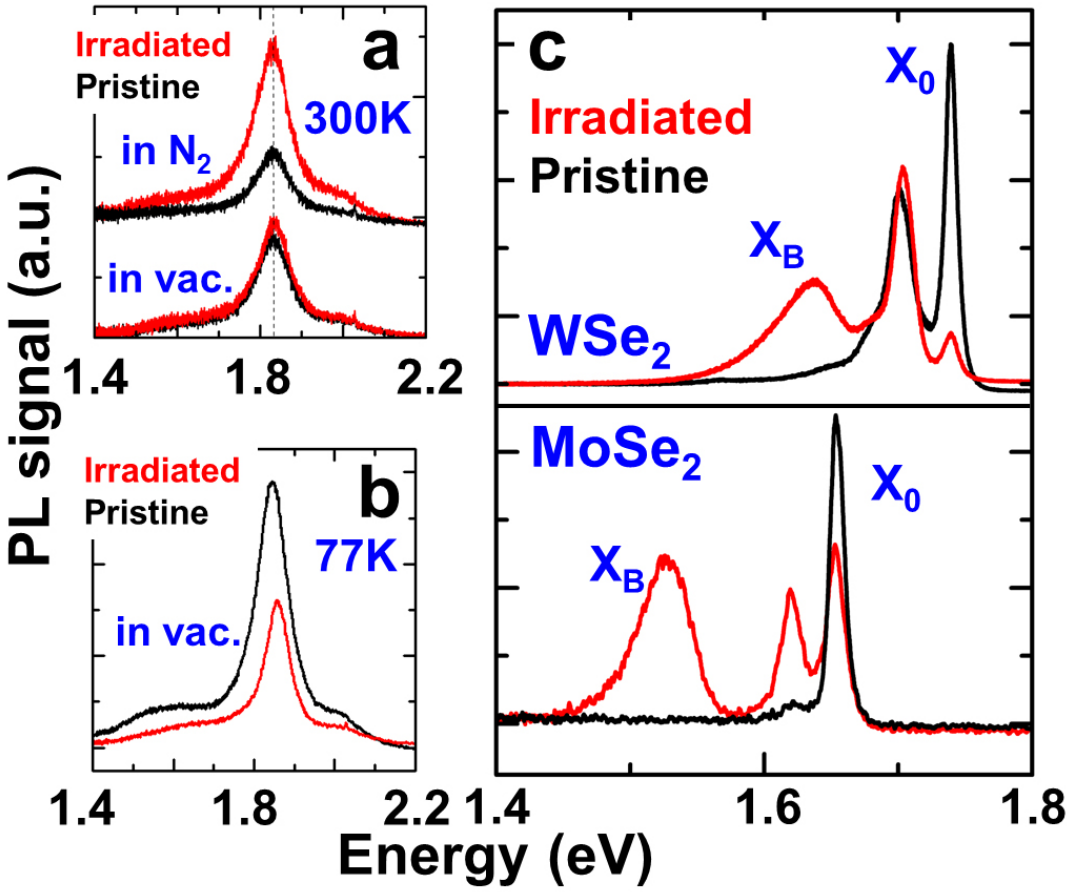

Figure 4.4. (a) PL spectrum of a monolayer MoS_2 at 300 K in the presence of N_2 or in vacuum before and after irradiation (dose ~ 8×10^{13} cm^{-2}). (b) The same taken at 77 K in vacuum. (c) PL spectrum taken at 77 K in N_2 on WSe_2 and $MoSe_2$ monolayers before and after the irradiation.

4.2 Density functional theory calculation

To understand the physical origin of the defect-induced PL peak (X_B) and the intensity enhancement in the main PL (X_0), we calculated the band structure and the density of states (DOS) of defective monolayer MoS_2. Our calculations were based on first-principles density functional theory (DFT) using projector augmented wave potentials [95]. The exchange correlation potential has been represented by the generalized gradient approximation characterized by Perdew-Burke-Ernzerhof [96] including van der Waals corrections [97] both for spin-polarized and spin-unpolarized cases. Effects of spin-orbit coupling and non-collinear magnetism were taken into account in the spin-polarized

calculations. The super-cell size, kinetic energy cut-off, and Brillouin zone sampling of the calculations were determined after extensive convergence analyses. A large spacing of ~15 Å between the 2D single layers was used to prevent interlayer interactions. A plane-wave basis set with kinetic energy cut-off of 300 eV was used. In the self-consistent field potential and total energy calculations, the Brillouin zone was sampled by special k-points. The numbers of these k-points were (25 × 25 × 1) for the primitive 1H-MoS_2 and were scaled according to the size of the super cells. All atomic positions and lattice constants were optimized using the conjugate gradient method, where the total energy and atomic forces were minimized. The convergence for energy were chosen to be 10^{-6} eV between two consecutive steps, and the maximum Hellmann-Feynman forces acting on each atom was less than 0.01 eV/ Å upon ionic relaxation. The pressure in the unit cell was kept below 5 kbar. Numerical calculations were performed by using the VASP software [98].

4.2.1 Effects of various S-vacancy configurations

Since the alpha particle irradiation [89] and thermal annealing may result in various types of sulfur vacancies in MoS_2, the monolayer MoS_2 was modeled in the presence of sulfur vacancies in different arrangements (Fig. 4.5).

In our measurements the sensitivity to the N_2 gas molecules are reversible with a time response limited to purging/pumping speed. Therefore, the binding between the monolayer transition metal dichalcogenides (TMDs) and N_2 gas has to be physi-sorption in origin. We have calculated the electronic band structure of monolayer MoS_2 in vacuum and N_2 rich environment before/after introducing the chalcogen vacancies. The binding energies of the N_2 gas molecules to monolayers were given by $E_b = E_{MoS_2+ad} - E_{MoS_2} - E_{ad}$ where E_{MoS_2+ad} is the total energy of relaxed structure of single layer MoS_2 and a N_2 molecule, E_{MoS_2} and E_{ad} are the total energies of single layer MoS_2 and N_2 molecule, respectively. Our calculations on monolayer MoS_2 were performed on 4 × 4 supercell including the spin-orbit interaction and magnetic coupling interactions. Even though N_2 molecule is physi-sorbed on MoS_2 by E_b ~70 meV, the molecular levels of N_2 are ~10–15 eV lower than Fermi energy of MoS_2 and therefore binding N_2 on monolayer MoS_2 has no influence on its photoluminescence peak position, lineshape, and magnitude.

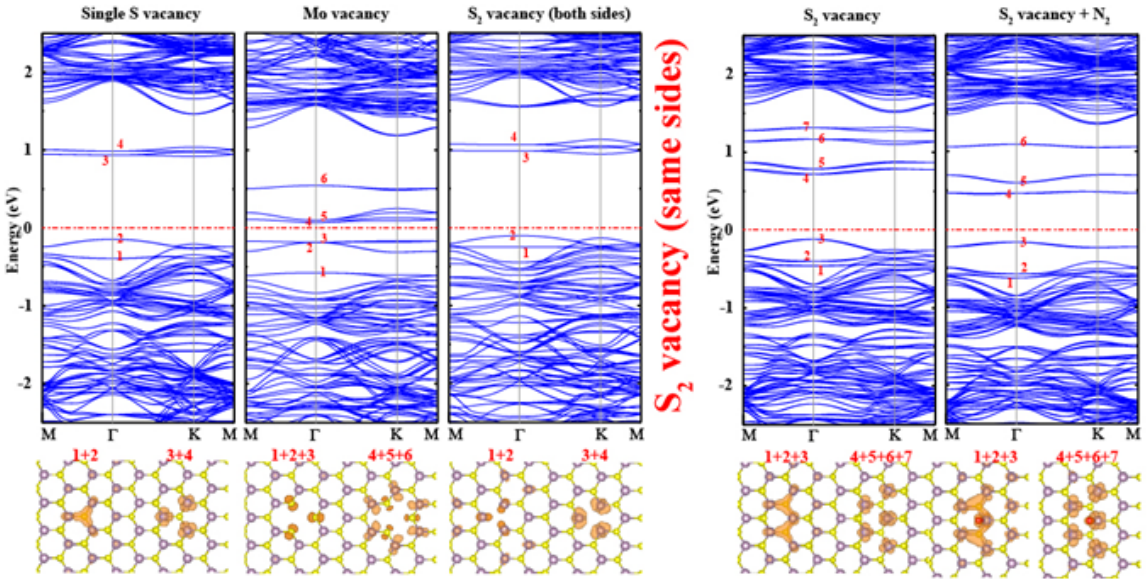

Figure 4.5. (Top panels) Band structure of monolayer MoS_2 in the presence of various types of vacancies. (Bottom panels) The charge density plots for each localized bands. Each charge density graph is made for localized bands within the bandgap. Isosurface value is taken as 7×10^{-5} e/Å^3.

Alpha particle radiation onto the surface of single layer MoS_2 and thermal annealing below decomposition temperature [91] can create vacancy defects on single layer MoS_2 and probably new physi-sorption sites for the N_2 molecules. It is known that vacancy defects in two-dimensional graphene [99-101], graphene nanoribbons, two-dimensional graphane and graphane nanoribbons give rise to crucial changes in the electronic and magnetic structure. We investigate four different types of vacancy defects that are formed on single-layer MoS_2, namely Mo and S single vacancies, two different geometric configurations of S_2 double-vacancies. These are two neighboring S vacancies on the same side of MoS_2 (same-side) and two neighboring S vacancies on different sides of MoS_2, but on top of each other (both-sides). Larger vacancy defects including MoS double-vacancies and MoS_2 triple-vacancies are not included in this study as larger defects are less probable to create, and generate attractive regions where molecules can get trapped and even dissociate into constituting atoms. All structures were optimized upon the creation of a particular type of vacancy. Vacancy energies, E_V, were calculated by subtracting the total energy of the perfect structure (without any vacancy) from the sum of the total energy of a structure having a particular type of vacancy and the total energy(ies) of missing atoms in the vacancy defect. The vacancy formation energies are 6.04, 14.13, 12.00 and 11.96 eV for S, Mo, S_2 (same-side) and S_2 (both-sides), respectively. It is energetically favorable by 80 meV to have S_2 double-vacancy in the same side of MoS_2 than having 2 separate non-interacting S vacancy defects.

To summarize, as shown in Fig. 4.5, after the vacancy is created, charges become localized around the vacancy regions as shown in the charge density plots and localized states are created within the band gap. These additional states introduce an intermediate level(s) for free excitons to relax to and further relaxation (radiative recombination) from these levels to VBM results in a new PL peak that is below the band edge luminescence. We first note that mono-chalcogen (S), di-chalcogen (S_2) (on both sides of MoS_2), and Mo vacancies introduce energy levels that is at least 0.4 eV below the band edge. However, these bands lay 0.2 eV below the CBM for MoS_2 with di-chalcogen vacancies (same side). We believe that the new PL peak appearing 0.15 eV below the free exciton PL at 1.9 eV is associated with the same-side di-chalcogen (S_2) vacancies whereas other types of vacancies only cause overall broadening in the bound exciton peak.

4.2.2 Interaction with N_2 molecules

Even though the same-side di-chalcogen vacancy provides an explanation for the peak position of the bound exciton peak, the bound exciton peak is only observable under N_2 gas conditions. For each vacancy defect, we carried out geometry relaxations for at least five different initial N_2 absorbed geometries to find the energetically most favorable absorption site. For single-vacancy defects (Mo and S), the only energetically favorable absorption site is ~ 0.2 nm above vacancy defect region where the N_2 molecule is parallel to MoS_2 surface. The calculated binding energies of N_2 molecule are 115 and 81 meV for S and Mo single-vacancy defects, respectively. Calculated energy band structures are the same as the ones without N_2 molecules around the Fermi energy (± 5 eV), since there is no significant interaction and charge transfer. Localized N_2 molecule states are ~10–15 eV lower than Fermi Energy. In the case of S_2 (both-sides) double-vacancy defects, there are two energetically probable absorption sites. One is similar with single-vacancy defects, where N_2 molecule is 0.2 nm away from the surface with a binding energy of 118 meV and has no effect on the electronic structure. In the other absorption geometry, N_2 takes the place of vacant S_2 sites and makes a strong bond with surrounding Mo atoms. Very high binding energy of 2.28 eV makes this absorption cite least probable for desorption of N_2. As S layers in MoS_2 act as charge accumulation regions, the N_2 molecule is 1.57 electrons negatively charged. In case of S_2 (same-side) double-vacancy defects, absorption geometry shown in Fig. 4.5 is the energetically most favorable site with a binding energy of 143 meV. When N_2 is physi-sorbed in this vacancy defect, 0.24 electrons accumulate on the N_2 molecule. The energy band structure shows minor changes in the localized states. Due to its low binding energy and comparable energies of localized states with first-principles *ab-initio* calculations and experiments, we conclude that clustered S vacancy defects on the same side of single-layer MoS_2, can provide physi-sorption sites for N_2 molecules and induce localized states which create new radiative channels.

4.2.3 Comprehensive understanding combined with experimentally observed photoluminescence behavior

Consequently, our calculations show that di-sulfur vacancies are most relevant to the experiments presented here, so our discussions will be limited to the di-S vacancies. In Figure 4.6(a), we show the band structure of a monolayer MoS_2 in the presence of di-S vacancies with and without the N_2 gas molecules around. We first note that once the di-S vacancies are created, new states appear within the bandgap. Specifically, states with energies 0.2 ~ 0.3 eV near the conduction/valence band edge (Figure 4.6(a) red) are of particular interest, as they are close to the energy difference between X_B and X_0 (0.12 eV). However, since the X_B peak is observable only in the presence of N_2 gas molecules, defect-induced levels themselves are not enough to explain our results. Next, we take into account the interaction with N_2 molecules at the defect sites (Figure 4.6(a) blue) and our findings are summarized as follows;

(1) In the absence of S vacancies, the interaction between the pristine monolayer MoS_2 and N_2 is negligible. N_2 molecules electronically interact with the MoS_2 only at the defect sites. The calculated binding energy of such interaction varies from 90 meV to 150 meV, depending on the type of the S vacancy, implying that the N_2 molecules are physi-sorbed (as opposed to chemi-sorbed) at the defect sites. As a result, the effect of N_2 is reversible when the chamber is purged with or pumped out of N_2.

(2) The interaction of a N_2 molecule with the di-S vacancy on a 4×4 unit cell results in ~0.2e charge transfer from MoS_2 to the N_2 molecule. The N_2 molecules deplete the material using the defect sites as channels, and the total free carrier density is much reduced. Consequently, screening on the excitons are lifted, hence the free neutral (X_0) and bound (X_B) neutral excitons are stabilized, while the negatively charged excitons (X^-) vanish due to the lack of equilibrium free electrons in the system to act as the second electron in the X^- [90]. As a result, the intrinsic free exciton line (X_0) is enhanced, and the X_B peak is observed.

(3) The discrete energy levels that are introduced by the S vacancies (Figure 4.6(a) red) are renormalized by the N_2 interacting with the defect sites (Figure 4.6(a) blue). Afterwards, two levels appear at ~0.2 eV above the valence band maximum (VBM) (labelled #1) and ,0.3 eV below the conduction band minimum (CBM) (labelled #4). Optical transitions from CBM to #1 and #4 to VMB yield a PL peak that is 0.2 eV and 0.3 eV lower than the X_0 peak. Based on these comparisons, we attribute the bound exciton peak X_B to either or both these transitions as shown in Figure 4.6(a).

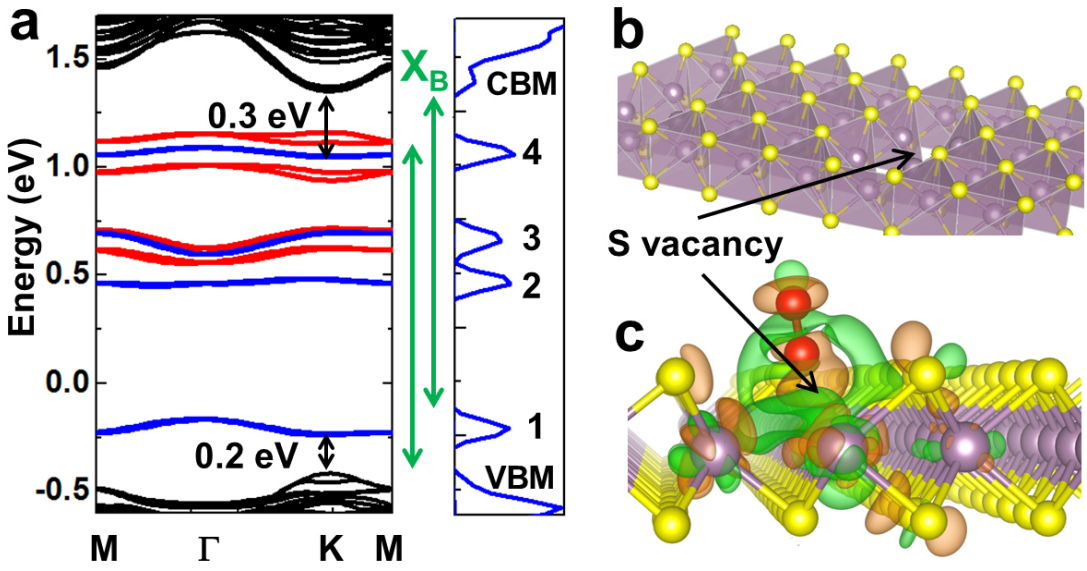

Figure 4.6. (a) Left panel: Calculated band structure of monolayer MoS_2 in the presence of di-S vacancies. Red levels within the bandgap are the levels appearing when the S vacancies are introduced. Blue levels appear when the N_2 molecule interacts with the S vacancies. Right panel: Total density of states of the monolayer MoS_2 with S vacancies in the presence of N_2. Here the modeled vacancies density is $7 \times 10^{13}/cm^2$. (b) Monolayer MoS_2 in the polyhedral representation to illustrate the di-S vacancy. (c) Charge density plots (iso-surface value = 10^{-3} e/Å^3) of monolayer MoS_2 with a di-S vacancy interacting with a N_2 molecule (red). Orange denotes charge accumulation and green charge depletion.

4.2.4 Possible impact from other environmental gas molecules

The onset of the X_B emission is not specific to N_2 gas, but to other gas species that are known to deplete the monolayer TMDs, such as O_2 [102]. Our DFT calculations show that the interaction with O_2 molecules at different types of vacancy types results in binding energies typically ranging from 300 meV to 8 eV. In most of the cases, binding O_2 molecule to the defective MoS_2 requires large energy to overcome the energy barrier (2 ~ 3 eV). We find that O_2 molecules only get physi-sorbed at the di-sulfur vacancy site with ~300 meV binding energy. Once the O_2 is absorbed at the surface, additional states appear within the bandgap and some of levels are within ~200 meV vicinity to conduction and valance bands (Figure 4.7). Similar to the case of N_2, transitions from these levels to conduction and valance bands are expected to yield X_B emission line(s).

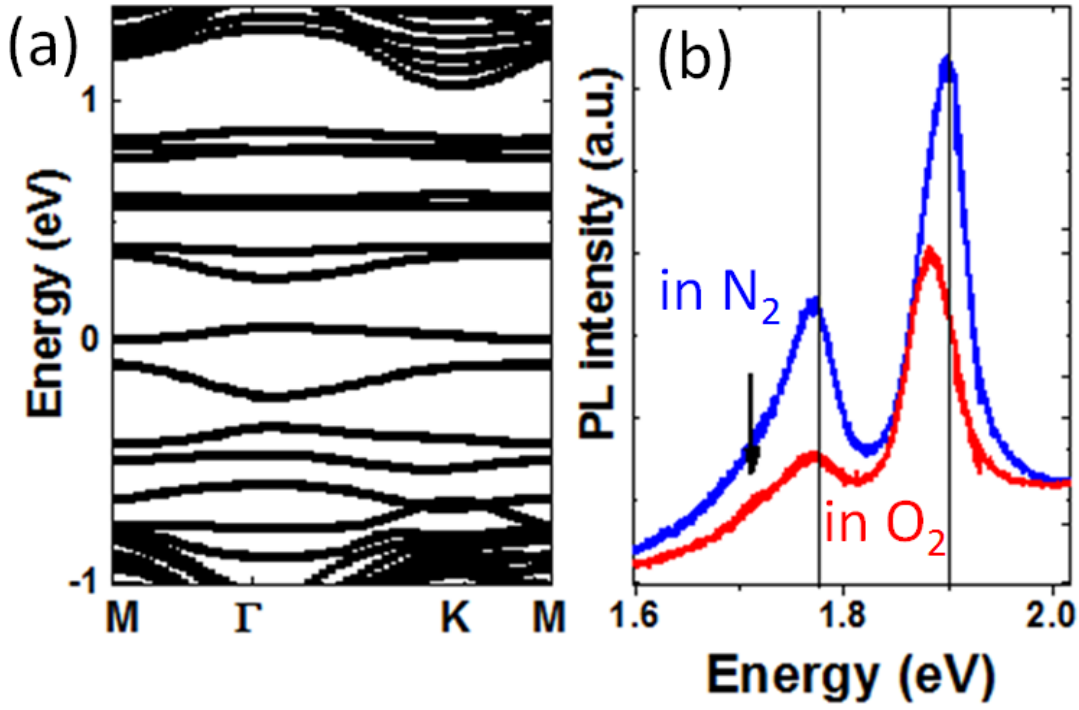

Figure 4.7. (a) Band structure of monolayer MoS_2 in the presence of di-sulfur vacancies interacting with O_2 molecules. (b) Comparison between PL spectra taken on irradiated MoS_2 monolayer in the presence of O_2 (red) and N_2 (blue) gases. The O_2 effect is only observable when the O_2 partial pressure is above 100 mTorr.

Consistent with the DFT predictions, the PL spectrum taken from irradiated MoS_2 in O_2 gas display a X_B peak 1.75 eV, and possibly more peaks at lower energies but cannot be individually resolved at 77 K. Even though the overall PL looks similar to the N_2 case, the X_B line is weaker and the X_0 line peak position is slightly different. These results show that the reported interaction of gas molecules with defect sites is a general effect applicable to a variety of monolayer TMDs (such as MoS_2, $MoSe_2$ and WSe_2), as well as different molecules (O_2 and N_2).

4.3 Summary and remarks

Point defects exist ubiquitously to different extents even in pristine 2D semiconductors. The observed effects of point defects are universal in other 2D semiconductors as well. Similar to MoS_2, after irradiating $MoSe_2$ and WSe_2 monolayers with alpha particles, a

broad bound exciton peak appears below the bandgap transition, as shown in Figure 4c. The bound exciton peak is located at 1.52 eV and 1.63 eV for $MoSe_2$ and WSe_2, respectively, which is about 0.10 eV below their bandgap. These results indicate that the reported interaction of gas molecules with defect sites and the resultant influence on the optical property are a general effect applicable to a variety of monolayer TMDs, as well as different environmental molecules (O_2 and N_2).

In conclusion, anion vacancies as point defects drastically modify the optical properties of monolayer TMDs in such a way that: (1) the overall integrated PL intensity is enhanced, and (2) a new, defect-related peak is observed below the bandgap. These effects are prominent at low temperatures and in gas environments (such as N_2). We show that the new peak originates from bound excitons that are formed by localizing excitons at the defect sites. The overall enhancement in the PL intensity is attributed to an electronic effect of the defects: the gas molecules drain free electrons from the material via these defect sites, causing a transition of exciton population from charged to neutral (both free and bound) excitons. Our results not only shed light on defect and exciton physics of 2D semiconductors in general, but also offer a new route toward tailoring their physical properties by defect engineering. The latter includes, for example, doping or compensating 2D semiconductors with irradiation, potentially creating 2D multi-bandgap semiconductors for wide-spectrum response akin to those enabled by defect-engineered 3D semiconductors [103], fabricating multi-colored light emission devices by controlling defects inside a single 2D semiconductor, and photometric-spectrally resolved optical sensors for sensing gas molecules and/or radiative environment.

Chapter 5

Substitutional chemical doping in 2D semiconductors[4]

I have not failed. I've just found 10,000 ways that won't work.

THOMAS A. EDISON (1847 – 1931)

In layered transition metal dichalcogenides (TMDs), each layer is weakly bonded to its neighbors by van der Waals force, thereby allowing physical or chemical isolation into atomically thin semiconducting layers, as well as assembly of junctions free of lattice mismatch issues. A wide variety of TMDs have been used as the active material to fabricate atomically thin field-effect transistors (FETs) [104,105], integrated circuits [106,107] and optoelectronic devices [108-110] such as light-emitting diodes, solar cells, and photodiodes.

Similar to traditional semiconductor technologies, stable *n*- and *p*-type conduction in the TMDs is indispensable for all these applications. Yet in contrast, a bipolar doping strategy of the TMDs is currently lacking. Wisdom can be learned from studies of conventional semiconductors, where a native, unipolar doping propensity is usually found. For example, in semiconductors such as CdO and InAs whose conduction

[4] Reproduced in part with permission from J. Suh et al., "Doping against the native propensity of MoS_2: Degenerate hole doping by cation substitution," Nano Letters **14,** 6976 Copyright 2014 American Chemical Society.

band minimum (CBM) and valence band maximum (VBM) lie low with respect to the vacuum level, native *n*-type conduction and difficulty in *p*-type doping are observed; the opposite is true for semiconductors such as Ge and diamond whose CBM and VBM lie high. This is attributed to the amphoteric doping behavior of electrically active native point defects [17], such as vacancies, interstitials, and defect complexes, which naturally occur in the materials in thermodynamic equilibrium. Extending this understanding to TMDs [111], it would be natural to predict a native *n*-type (*p*-type) behavior of not intentionally doped MoS_2 (WSe_2), given the low (high) - lying CBM and VBM in MoS_2 (WSe_2) as seen in Fig. 5.1(a).

Currently, modulation of carrier type and density in these layered TMDs is achieved by means of electrostatic FET gating [108-110,112], metal work-function engineering [113,114], surface functionalization [115,116], or charge transfer from physic-sorbed volatile molecules [102]. However, to dope TMDs against their natural doping propensity, such as *p*-type in MoS_2 (*n*-type in WS_2) with very low VBM (high CBM), it is challenging to find molecules capable of donating holes (electrons) effectively to these low (high) - lying band edges. Moreover, practical applications require substitution of host atoms with dopants as practiced in traditional semiconductors, where the doping is secured and stabilized by covalent bonding inside the lattice. Hetero-junctions integrating different materials, such as *n*-type MoS_2 with *p*-type WSe_2 [117,118], have been fabricated as an alternative to homo-junctions, but these hetero-structures usually suffer from their type-II band offset. For example, it leads to lower photo-voltages because the band offset curtails the maximum splitting of Fermi levels, as well as red-shifted light emission due to recombination across the spatially indirect band edges.

Indeed, for MoS_2, consistent with the prediction above, recent electrical [104-107] and optical [80] investigations confirm its native *n*-doping, owing hypothetically to sulfur vacancies [119]. The lack of *p*-type doping strictly limits carrier conduction in MoS_2 to its conduction bands, despite the suggestion that *p*-type operation is more desirable for MoS_2-based FET devices [112], and much more interest lies in its spin-polarized valence bands for the recently developed valleytronics [120,121]. Niobium (Nb), which has one less valence electron than Mo, is theoretically suggested as the most suitable substitutional acceptor by density-functional energetics / formation energies calculations [122]. Moreover, MoS_2 and NbS_2 share the identical 2H crystal structure, with similar lattice parameters, a = 3.16 Å and 3.32 Å, and c = 12.29 Å and 11.94 Å for MoS_2 and NbS_2, respectively [123]. The covalent radius (Mo = 130 pm and Nb = 134 pm) [124] and oxidation states of Mo and Nb in the 2H-polytype lattice are nearly identical. Indeed, fullerene-like $Mo_xNb_{1-x}S_2$ nanoparticles [125] and polycrystalline thin-films [126] have been reported, but unambiguous *p*-type conduction and direct evidence of the substitutionality of doping have not been demonstrated in single-crystal MoS_2. In this Chapter, we report stable *p*-type conduction in MoS_2 single crystals and ultra-thin layers via substitutional Nb doping. The substitutionality of the Nb dopants in the MoS_2 crystals

is confirmed by structural and chemical analysis techniques, and the degenerate *p*-type conduction is evaluated by Hall-effect and gated transport studies. Prototypical *p*-*n* homo-junctions built from vertically stacked MoS_2 layers show current rectification tunable by a gate voltage.

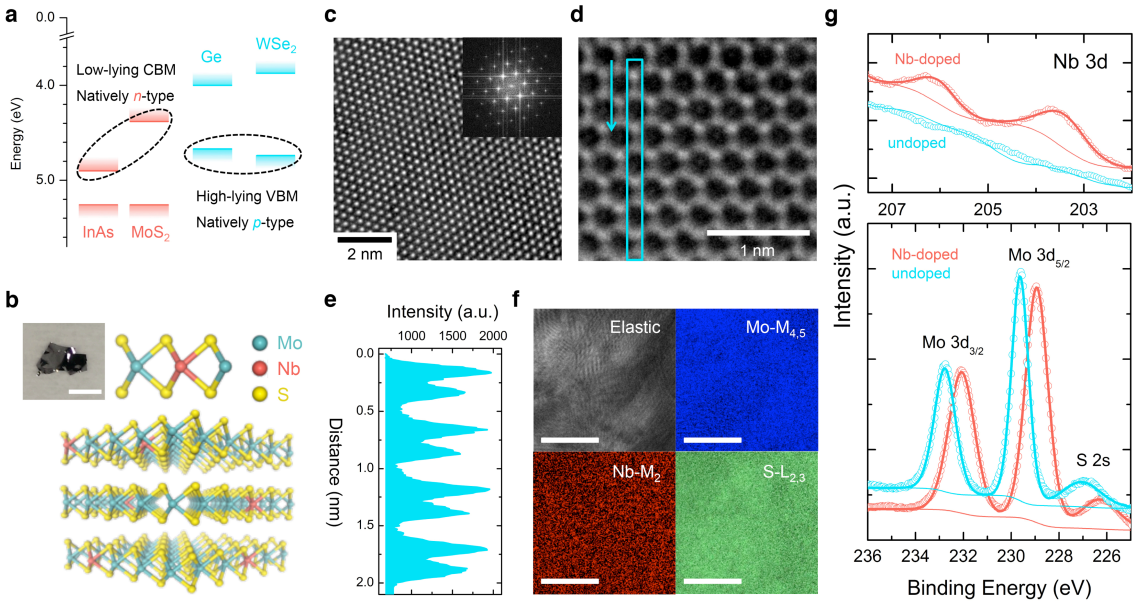

Figure 5.1. Structural and chemical analyses of Nb-doped MoS_2 (MoS_2:Nb). (a) Band-edge (CBM and VBM) alignment of representative conventional semiconductors and TMDs, referenced to the vacuum level. (b) Cross-section illustration of van der Waals coupled MoS_2:Nb layers where Nb dopants replace the Mo host atoms in a substitutional manner. A digital photograph inset shows a synthesized MoS_2:Nb crystal with a scale bar of 3 mm. (c) HRTEM image of the MoS_2:Nb with the corresponding FFT in the inset. (d) Cs (spherical aberration)-corrected HRTEM image with sub-Å resolution acquired from the monolayer part. (e) Transmitted electron intensity along the vertical direction of corresponding blue box denoted in Fig. 5.1d. (f) EFTEM-SI maps of elastic (0 eV), Mo $M_{4,5}$, Nb M_2, and S $L_{2,3}$ measured from the same region of the MoS_2:Nb sample. Scale bars are 100 nm. (g) XPS scans of the Nb 3d (top), the Mo 3d, and S 2s (both in bottom) core-levels measured from the Nb-doped and undoped MoS_2.

5.1 Material synthesis

The Nb-doped MoS_2 (MoS_2:Nb) single crystals were grown by a chemical vapor transport (CVT) method using iodine as the transport agent, an approach that has been employed to prepare other layered compounds with high quality [127]. A horizontal three-zone furnace was utilized where the high (low) temperature zone was used as the reaction (growth) zone, as seen in Fig. 5.2. Prior to the crystal growth, a quartz tube containing the transport agent and the elements required for the doped crystals was evacuated to below 10^{-6} Torr and securely sealed. The purity of the source materials was Mo 99.99%, S 99.99%, and Nb 99.99%, with a molar ratio of Mo:S:Nb equal to 1:2:0.005 for a nominal 0.5% Nb doping. The sealed quartz tube was then inserted into the three-zone furnace. In the beginning, the temperature of the growth zone was set to 1000 °C for 12 hours to remove any possible residues.

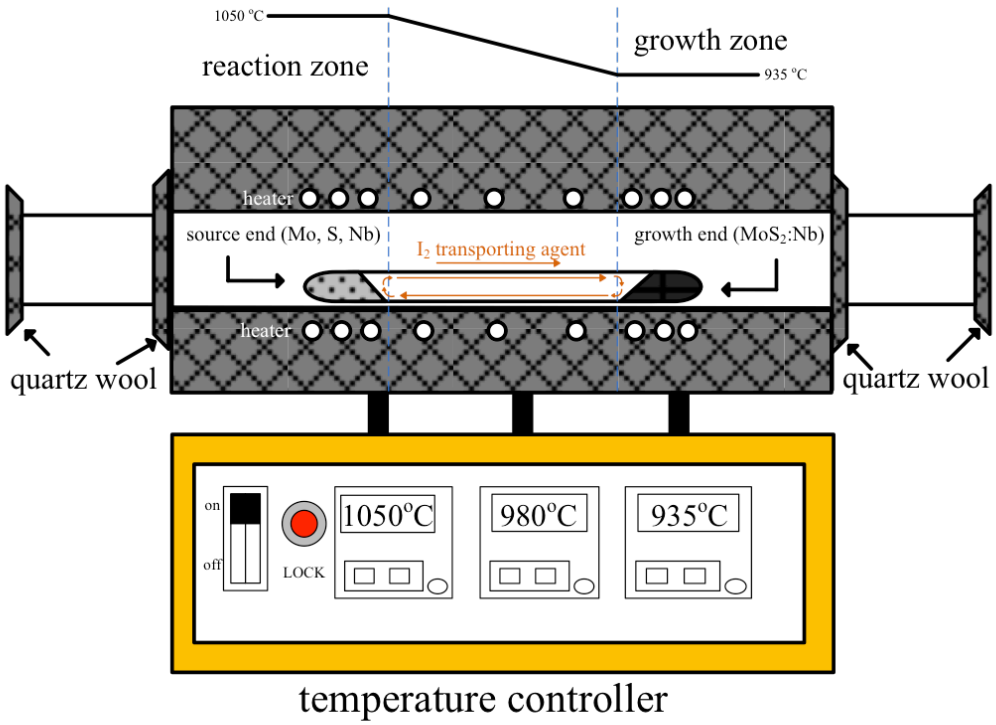

Figure 5.2. Schematics of the three-zone furnace setup used for the Nb-doped MoS_2 crystal growth. Top panel shows the corresponding temperature profile along the horizontal quartz tube during growth process.

The process of the CVT was then initiated with a temperature gradient varying from 1050 °C in the reaction zone to 935 °C in the growth zone over a distance of ~30 cm, and the system was held in this condition over 500 hours in order to provide sufficient diffusion and equilibration for the single-crystal synthesis. The CVT growth yielded large, thin, and shiny MoS_2:Nb crystals that are typically a few mm in lateral size with high crystallinity (Fig. 5.1(b)). Similar to other TMDs, these as-synthesized MoS_2:Nb crystals are exfoliation-ready, and the number of exfoliated layers can be determined by Raman spectroscopy and atomic force microscopy (Fig. 5.3).

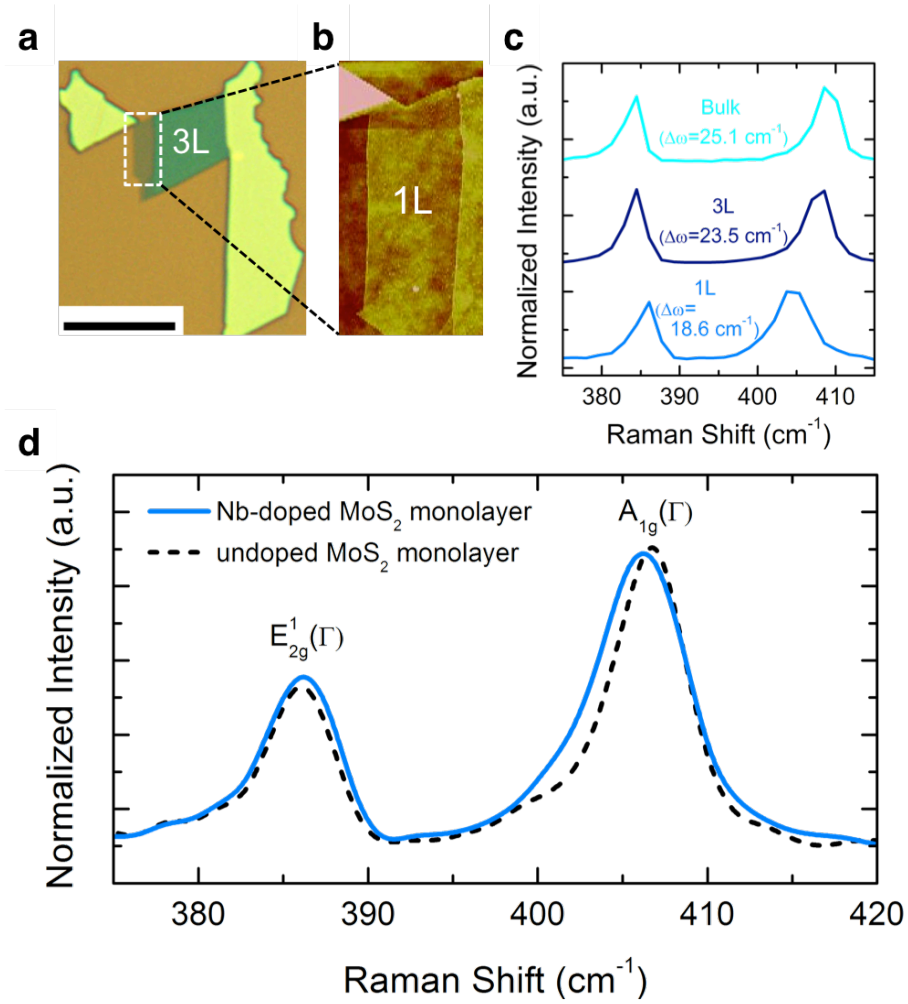

Figure 5.3. (a) Optical image of the as-exfoliated atomic terrace structure consisting of monolayer (1L), trilayer (3L), and bulk MoS_2:Nb. Scale bar is 10 μm. (b) Zoom-in AFM image of the corresponding monolayer part. (c) Raman spectra, normalized by peak height, of 1L-, 3L-, and bulk MoS_2:Nb acquired at room temperature. The frequency difference (Δω) between in-plane (E^1_{2g}) and out-of-plane (A_{1g}) phonon modes at Γ point decreases with the number of layers, and is reduced to ~ 18.6 cm^{-1} in 1L MoS_2:Nb from the bulk value of 25.1 cm^{-1}. (d) Comparison of normalized Raman spectra between Nb-doped and undoped monolayer MoS_2. We note that the Raman spectral shape slight changes upon Nb doping (hence greater carrier density); the linewidth of the A_{1g} mode broadens and slightly softens. In contrast, the E^1_{2g} mode is insensitive to the Nb doping. This suggests a stronger electron-phonon coupling of the A_{1g} mode, which is similar to the change in Raman spectrum induced by FET gating [128]. In this regard, Raman spectroscopy can be quite useful for probing the level of doping in 1L-MoS_2 as that is employed in graphene devices.

5.2 Structural analysis with HR-/EF-TEM

To determine the crystal structure and evaluate the crystallinity of the MoS_2:Nb, we deployed extensive high-resolution transmission electron microscopy (HRTEM) measurements over a wide area on multiple samples. After mechanical exfoliation onto a SiO_2/Si substrate, Nb-doped MoS_2 micro-flakes were transferred to Quantifoil holey carbon-coated Au TEM grids using a polymer-free transfer technique. Cs (spherical aberration)-corrected HRTEM with sub-Å resolution was taken using FEI Titan 80–300 environmental TEM with 80 kV accelerating voltage and a negative spherical aberration coefficient (-20 μm). EFTEM-SI (spectrum image) using JEOL ARM 200cF with GIF Quantum® 965 EELS spectrometer was conducted under these conditions; energy range/slit width/step size: 120–550 eV/10 eV/1 eV and exposure time of a step: 2 sec. Elemental maps of Mo, Nb and S from EFTEM-SI were achieved by energy-filtering at 227 eV (Mo $M_{4,5}$), 378 eV (Nb M_2), and 165 eV (S $L_{2,3}$), respectively.

The as-synthesized MoS_2:Nb is single crystalline, exhibiting a hexagonal lattice as seen from the fast-Fourier transform (FFT) pattern displayed in the inset of Fig. 5.1(c) (see also selected area electron diffraction pattern in Fig. 5.4(a)). The estimated lattice spacing of 1.6 and 2.7 Å, corresponding to the (110) and (100) planes, respectively, is consistent with reported values [129]. Cross-section HRTEM images also show highly parallel layer stacking with an inter-layer separation of approximately 6.15 Å (Fig. 5.4(b)). The Cs (spherical aberration)-corrected atomic HRTEM image in Fig. 5.1(d) clearly reveals hexagonal rings formed by the S atoms (dimmer sites) together with the transition metal atoms, the Mo atoms or Nb dopants (brighter sites) supported by the corresponding intensity profiles presented in Fig. 5.1(e). It is noted that structural imperfections such as grain boundaries, dislocations, and atomic defects were not observed from the HRTEM. Energy-filtered electron transmission microscopy spectrum imaging (EFTEM-SI) was subsequently used to probe the chemical composition of the MoS_2:Nb with nanoscale spatial resolution, in particular, the incorporation of Nb dopants into the lattice. As seen in Fig. 5.1(f), the Nb signal was well resolved through its M_2 peak (~ 378 eV), and is indeed uniformly dispersed in the MoS_2 matrix with no evidence of clustering (also see the corresponding electron energy loss spectrum in Fig. 5.4(c)).

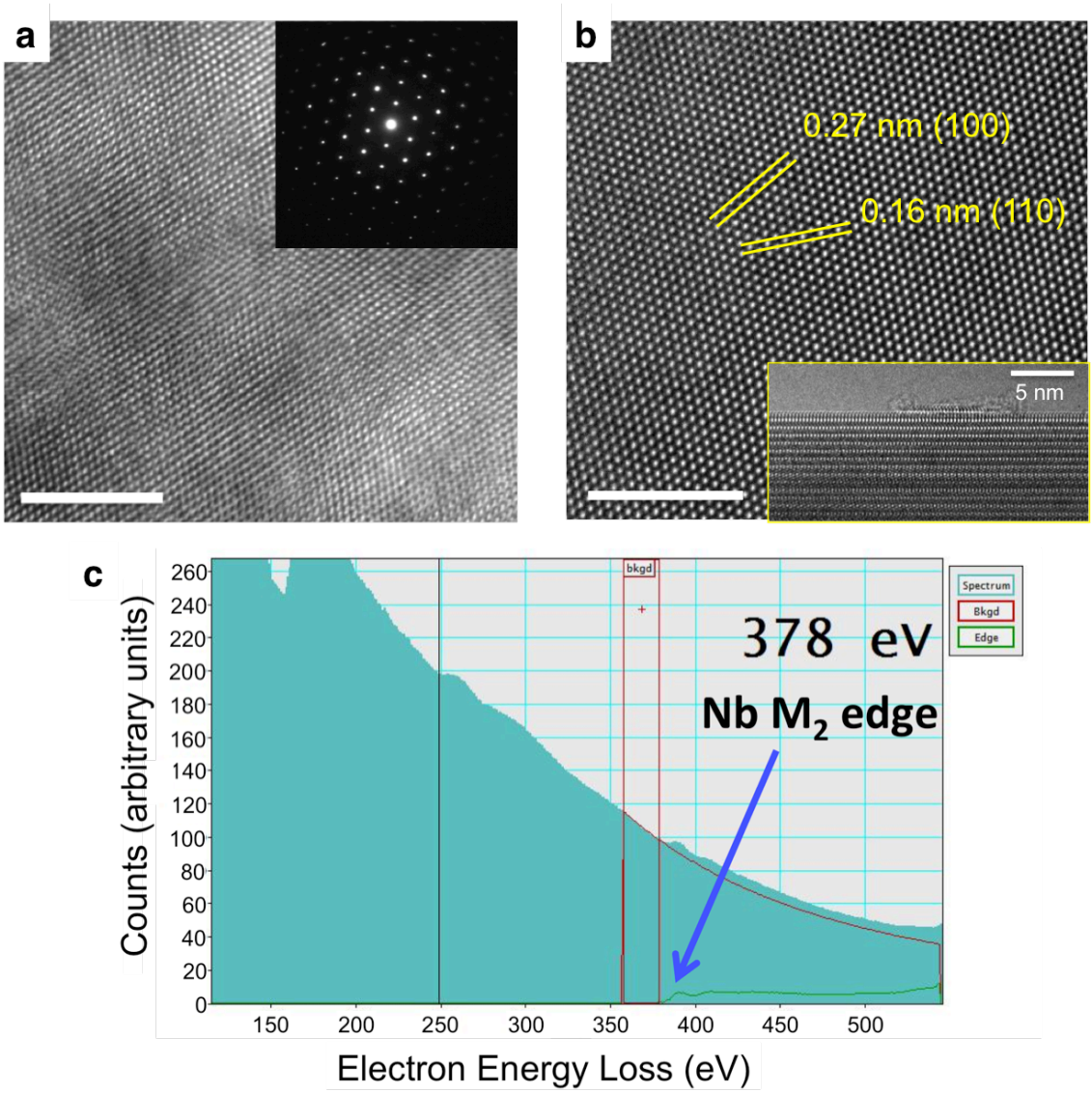

Figure 5.4. (a,b) Additional HRTEM images of a MoS_2:Nb flake with the selected area electron diffraction pattern acquired and the measured lattice spacing, respectively. Scale bars are 5 nm. Inset in Fig. 5.4b shows a HRTEM image taken from the MoS_2:Nb flake with its basal planes oriented in parallel to the electron beam. Estimated inter-plane distance from the image is ~ 6.15 Å. (c) Extracted electron energy loss spectrum (EELS) from the EFTEM-SI showing the Nb M_2 peak at ~ 378 eV.

5.3 Chemical analysis with XPS

The Nb dopants in the MoS_2 crystals were further analyzed with X-ray photoelectron spectroscopy (XPS). XPS was performed on both undoped and Nb-doped MoS_2 utilizing a Mg Kα X-ray source (1253.6 eV) from an anode operated at 300 W and a hemispherical NanoSAM electron energy analyzer in a ultra-high vacuum chamber (base pressure ~ 10^{-10} mbar). The samples were directly grounded through metal holders to the system, and the pass energy was kept constant at 10 eV during the scans. Distinct binding energy peaks associated with the Nb 3d core levels at 203.6 and 206.1 eV were detected only in the MoS_2:Nb samples (Fig. 5.1(g)), and they well match previously observed XPS features from fullerene-like $Mo_{1-x}Nb_xS_2$ nanoparticles [125]. In addition, the core-level peaks of Mo and S in the MoS_2:Nb show a uniform shift toward lower binding energies compared to those of the undoped MoS_2. This shift is attributed to lowering of the Fermi level (E_F) upon the *p*-type doping, as similarly observed in previous studies [125]. The amount of E_F downshift, ~ 0.7 eV, is found to be consistent with the MoS_2 band gap of 1.2 eV and the degenerate *p*-doping.

5.4 Substitutional doping revealed by EXAFS

Recent reports have suggested many possible, non-substitutional atomic configurations for dopants in MoS_2, *e.g.,* adatom [130] or intercalation [131]. Therefore, it is important to evaluate the substitutionality of Nb in the MoS_2 lattice. Since Nb and Mo atoms are adjacent to each other on the periodic table, it is rather difficult to distinguish them in the HRTEM, and more chemically sensitive characterization techniques are required to determine the location of Nb dopants. Extended X-ray absorption fine structure (EXAFS) analysis is ideally suited for this purpose, allowing for determination of local environment around the X-ray absorbing atoms. By analyzing oscillations in the normalized X-ray absorption data, critical information can be extracted such as local coordination number (*N*), interatomic distance to neighboring atoms (*r*), and the Debye-Waller disorder parameter (σ^2). Despite their adjacent atomic numbers, the *K* edge energies of Nb and Mo are widely separated by ~1 keV (Nb = 18.99 keV and Mo = 20.01 keV), and this provides sufficient energy span to fully resolve their EXAFS oscillations in the post-absorption spectral region.

EXAFS measurements at the Nb *K* edge and Mo *K* edge were carried out at the Stanford Synchrotron Radiation Laboratory on beamline 7-3 using a Si (220) monochromator at phi=0°, considering its glitch database in the measured energy range. A Rh-coated Si collimating mirror was used to reject the significant fraction of the higher

harmonic signal. Before the measurements, reference Nb and Mo metal foils were also measured for calibration of energy absorption shift. Due to the small amount of Nb dopants, EXAFS data for Nb *K* edge was acquired in a fluorescence geometry using 30-element germanium detector (Canberra). On the contrary, EXAFS of Mo *K* edge was collected in transmission mode where X-ray intensity was measured after passing through the sample using an ionization chamber. Long data collection times (> 8 hrs per measurement) were employed in order to obtain more precise EXAFS signals, and they were averaged in the software package Sixpack after background subtraction. Further data reduction of the EXAFS spectra was processed with Athena, and curve fitting was performed with the Artemis and IFEFFIT software.

Figure 5.5(a) shows the normalized absorption data for the Nb and Mo *K* edges, collected in the fluorescence and transmission mode, respectively. Figure 5.5(b) shows the extracted EXAFS oscillations, k^3-weighted $\chi(k)$, along with the result of best fitting to the data. The fitting was determined by Fourier transforming the $\chi(k)$ across a *k*-range up to 15 $Å^{-1}$ considering the first two coordination shells for both the Nb and Mo *K* edges (see detailed fitting parameters in Table 5.1).

The results show nearly identical *N* and *r*, and thus local atomic bonding environment for the Nb and Mo atoms, clearly indicating the substitutional nature of Nb atoms. The Fourier transformed k^3-weighted EXAFS is plotted in Fig. 5.5(c) showing two distinct peaks at two radial distances. The first peak corresponds to atomic bonds with S atoms, the nearest neighbor of the transition metal atoms, and the second peak is associated with intra-layer cation (transition metal) neighbors. These bond lengths agree quantitatively with those measured in MoS_2 single crystals [132]. Here, while scattering from the first and second nearest neighbors of the X-ray absorbing cation atoms is evident, the existence of the inter-layer van der Waals gap may damp contributions from neighbors at greater distances. We also note that σ^2 is quite narrow, despite that the data was collected in ambient air at 300 K, which further confirms the high crystal quality in agreement with the HRTEM measurements.

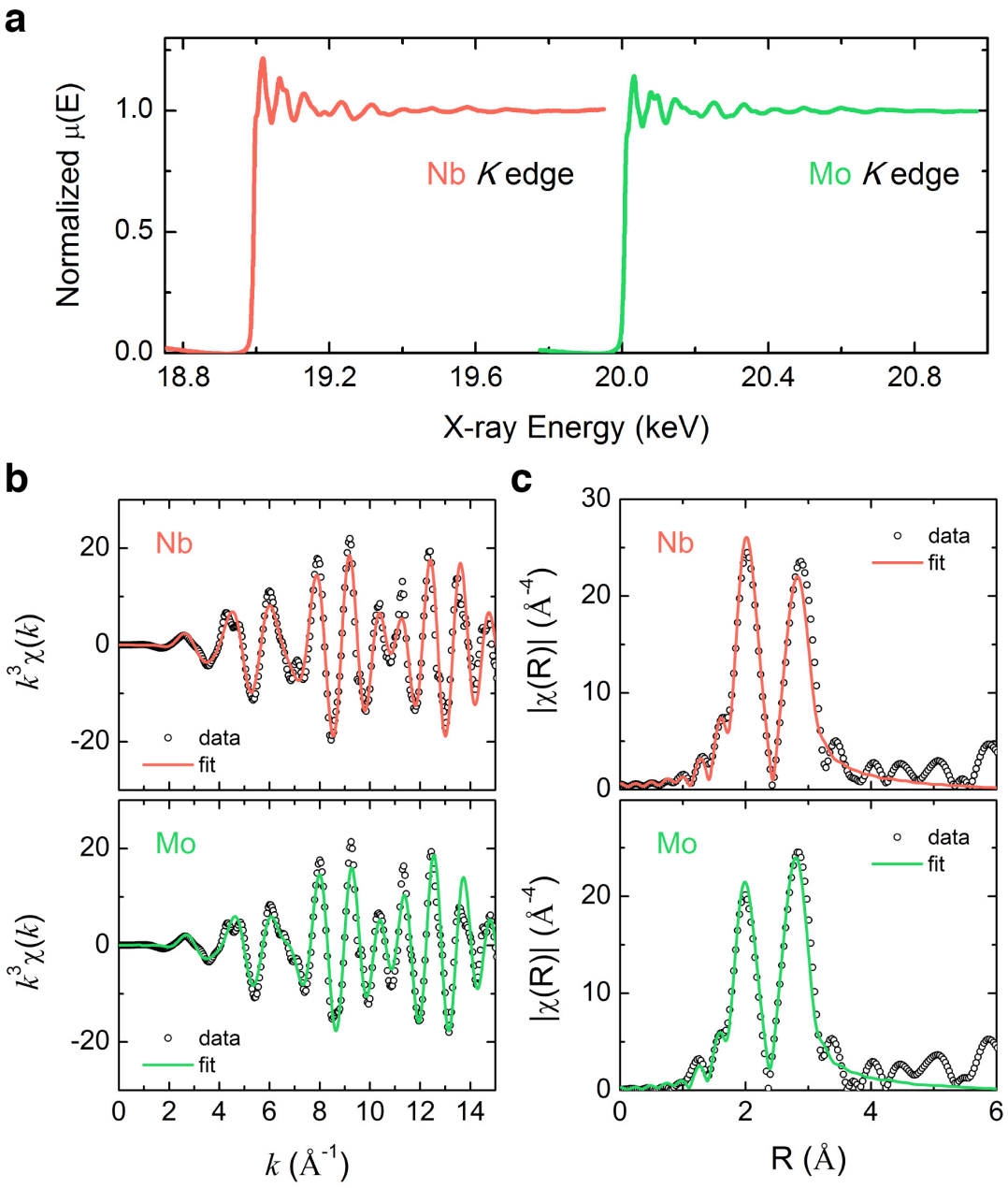

Figure 5.5. EXAFS analysis on Nb-doped MoS_2: Evidence for substitutional doping. (a) Raw X-ray absorption data for the Nb and Mo *K* edges normalized by peak intensity. (b) EXAFS oscillations extracted from the absorption data weighted by k^3. (c) Radial distribution of Fourier-transformed EXAFS signal. Points are raw experimental data while red and green lines are best fits for the Nb and Mo *K* edge, respectively.

	1st Peak (Nb–S)			2nd Peak (Nb–Mo/Nb)		
	N_1	r_1 (Å)	σ_1^2 (Å^2)	N_2	r_2 (Å)	σ_2^2 (Å^2)
Nb	6	2.4489	0.00169	6	3.1653	0.00197
	1st Peak (Mo–S)			2nd Peak (Mo–Mo/Nb)		
	N_1	r_1 (Å)	σ_1^2 (Å^2)	N_2	r_2 (Å)	σ_2^2 (Å^2)
Mo	6	2.4042	0.00151	6	3.1394	0.00186

Table 5.1. EXAFS fitting parameters for Nb-doped MoS_2.

5.5 Electrical transport characterization

We measured the *p*-type electrical conduction in a thin flake mechanically exfoliated from the MoS_2:Nb crystals using variable-temperature Hall effect. The multilayer MoS_2:Nb Hall device was fabricated on a 300 nm SiO_2/Si substrate, and standard e-beam lithography (EBL) was used to define the flake into a Hall bar configuration as seen in Fig. 5.7(a). After etching the unwanted area with XeF_2 gas, a second EBL was performed to pattern the voltage leads and current injection electrodes, followed by deposition of Ti/Au (5/100 nm) metal contacts. As shown in Fig. 5.6, two-probe *I-V* curves displayed linear characteristics suggesting ohmic contacts, despite the Schottky barrier expected between the MoS_2 valence band and Ti (surface potential-energy barrier $\Phi_B \sim 1.0$ eV, estimated from the Ti work function 4.33 eV and the VBM of MoS_2 [111]). This is attributed to the degenerate *p*-type doping resulting in very narrow depletion width of a few nm, thereby allowing significant tunneling current to flow as typically occurring in heavily doped semiconductors.

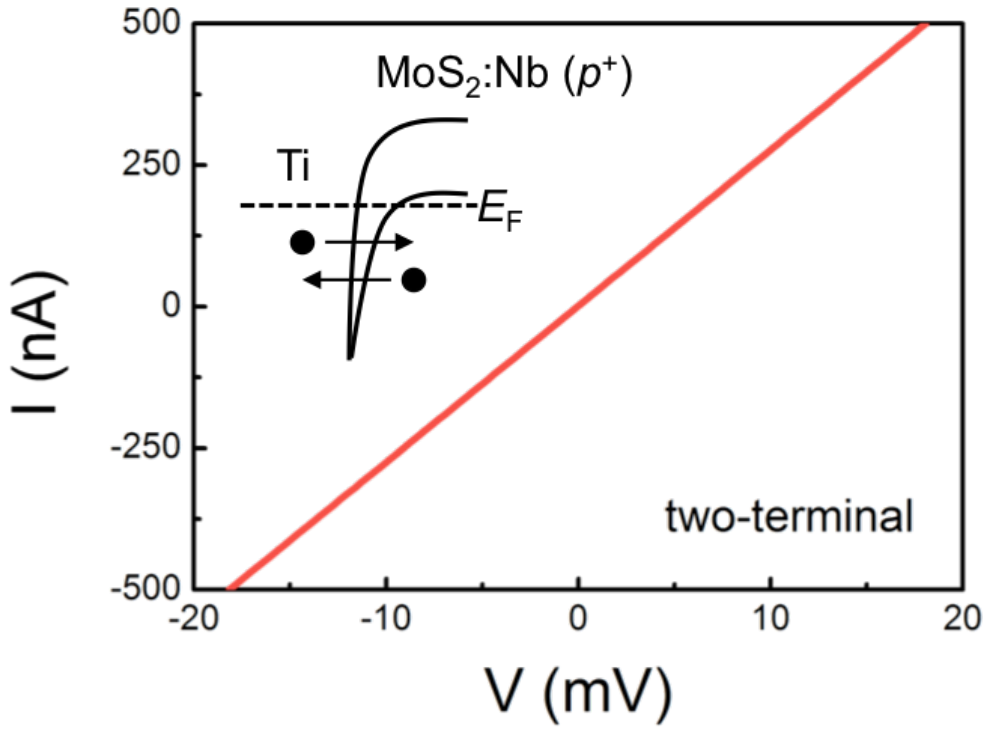

Figure 5.6. Two-terminal *I-V* characteristic of the MoS_2:Nb flake measured at 10 K, showing nature of ohmic contact with Ti. Inset is an expected schematic band diagram across Ti and the degenerate *p*-type MoS_2:Nb, depicting the Schottky barrier overridden by charge tunneling due to the degenerate doping.

The measured Hall resistance, R_{xy}, is plotted as a function of the magnetic field (B) in Fig. 5.7(b). The magnetic field was varied up to 4 T, and both current injection directions were used in order to remove influence of possible misalignment of voltage electrodes from the longitudinal resistance R_{xx}; that is, the treatment is equivalent to $R_{xy}(B)=\left(V_{xy}(+B)-V_{xy}(-B)\right)/2I_{xx}$ [133]. The results confirm the *p*-type conduction of MoS_2:Nb, as well as reveal a constancy of the Hall coefficient $R_H(=R_{xy}/B=-1/p_{2D}e)$ over a wide range of temperature. Linear fitting in Fig. 5.7(b) yields a high hole concentration of 3.0 × 10^{19} cm^{-3}, far exceeding the critical hole concentration for degenerate *p*-type doping in MoS_2. The critical hole concentration ($E_F \sim E_V + 3kT$) for degenerate *p*-type MoS_2 is estimated by using a parabolic valence-band model and the corresponding analytical formula, $p=2\left[\frac{m_p^* kT}{2\pi\hbar^2}\right]^{3/2} e^{(E_V-E_F)kT}$. It was found to be approximately 7 × 10^{17} cm^{-3} using a hole effective mass m_p^* of 0.68 m_o [134]. Therefore,

our measured hole density far exceeds this value and justifies our explanation assuming a degenerate doping.

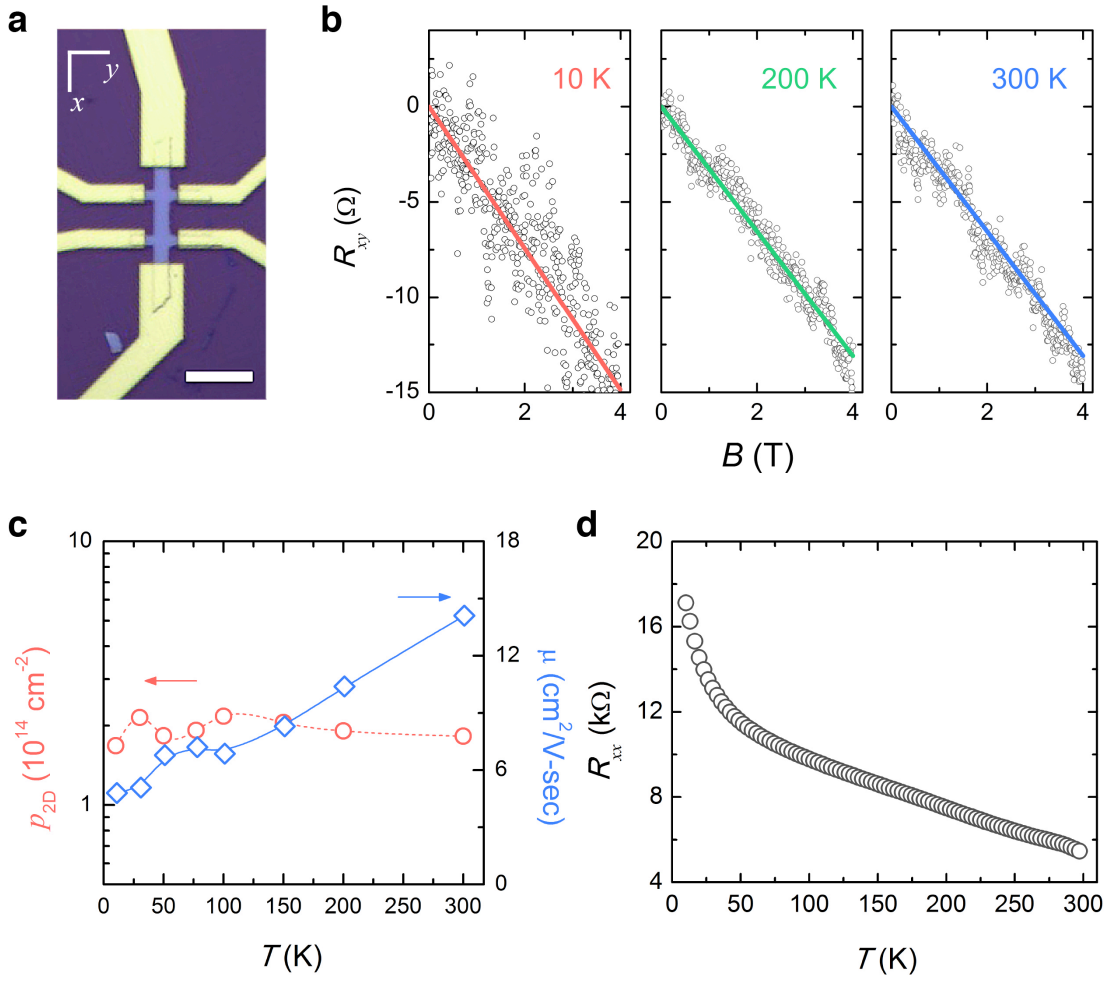

Figure 5.7. Hall-effect measurement of MoS_2:Nb micro-devices. (a) Optical microscopy image of a Hall-bar device based on a multilayer (61 nm thick, determined by atomic force microscopy) MoS_2:Nb flake (Scale bar = 10 μm). (b) Hall resistance, R_{xy}, as a function of magnetic field at three representative temperatures (10, 200, and 300 K). Blank circles and color lines are the measured data and linear fits, respectively. (c) Calculated hole sheet concentration (red) and Hall-effect mobility (blue) as a function of temperature from 10 K to 300 K. (d) Longitudinal resistance R_{xx} of the Hall-bar device as a function of temperature.

The absence of carrier freeze-out (Fig. 5.7(c)) indicates a degenerate level of doping, and such a dense hole concentration in the degenerate limit is indeed in good

agreement with the nominal doping concentration of Nb assuming each of the Nb atoms acts as a single acceptor [124]. We also note that a nearly identical hole density is observed from another Hall device. Combined with the four-terminal R_{xx} data presented in Fig. 5.7(d) and geometrical factors of the Hall device, the Hall mobility (μ) was extracted, which shows a monotonic increase with temperature. This is a further signature of degenerately doped semiconductors, where ionized impurity scattering dominates over phonon scattering even at room temperature. This is the opposite to the behavior of intrinsic MoS_2 crystals, where acoustic phonon scattering plays a much greater role in limiting μ at room temperature [105].

5.6 Device application based on 2D hetero-strucuture

To demonstrate a proof-of-concept device application of the substitutionally doped MoS_2, we fabricated a *p*-*n* homo-junction. First, back-gated FETs using Nb-doped and undoped MoS_2 flakes were separately fabricated, and typical electrical transport characteristics are presented in Fig. 5.8(a). The undoped, few-layer FET shows a strong, *n*-type gate voltage (V_g) dependence in the source-drain current (I_{ds}). In contrast, the MoS_2:Nb device exhibits a drastically different behavior with a *p*-type conduction, a much weaker V_g dependence, and much higher on-current. The weak V_g dependence of the MoS_2:Nb device is similar to recent observations from degenerately *n*-type doped MoS_2 crystals [135], further confirming the degeneracy of our Nb doping level.

Next, a vertically stacked *p*-*n* junction was formed by overlaying a multilayer MoS_2:Nb flake onto a few-layer, undoped MoS_2, as shown in the inset of Fig. 5.8(b). The sample was then mildly annealed to enhance the inter-layer coupling [136] between the van der Waals *p*-*n* interface. Ti/Au layers were deposited again for achieving ohmic contacts with both the MoS_2:Nb and undoped MoS_2. Such vertically stacked device architecture has been recently shown to be able to support high current densities and offer superior tunability of the junction current [137]. The resultant *p*-*n* homo-junction exhibits excellent rectification characteristics as shown in Fig. 4b. Remarkably, the degree of rectification is tunable by modulating the density of free carriers in the bottom *n*-type layer with electrostatic field from the back gate. In such asymmetric p^+-*n* junction devices, the rectification properties are predominantly governed by the lightly doped *n*-side in which the depletion layer extends. While the heavily *p*-doped MoS_2:Nb is relatively insensitive to V_g, the density of electrons in the undoped *n*-side rapidly increases upon more positive V_g, leading to much enhanced current flow (see a qualitative band diagram in Fig. 5.9). This unique, tunable rectification of current is fully reversible with respect to variation of V_g, indicating the operation stability and durability.

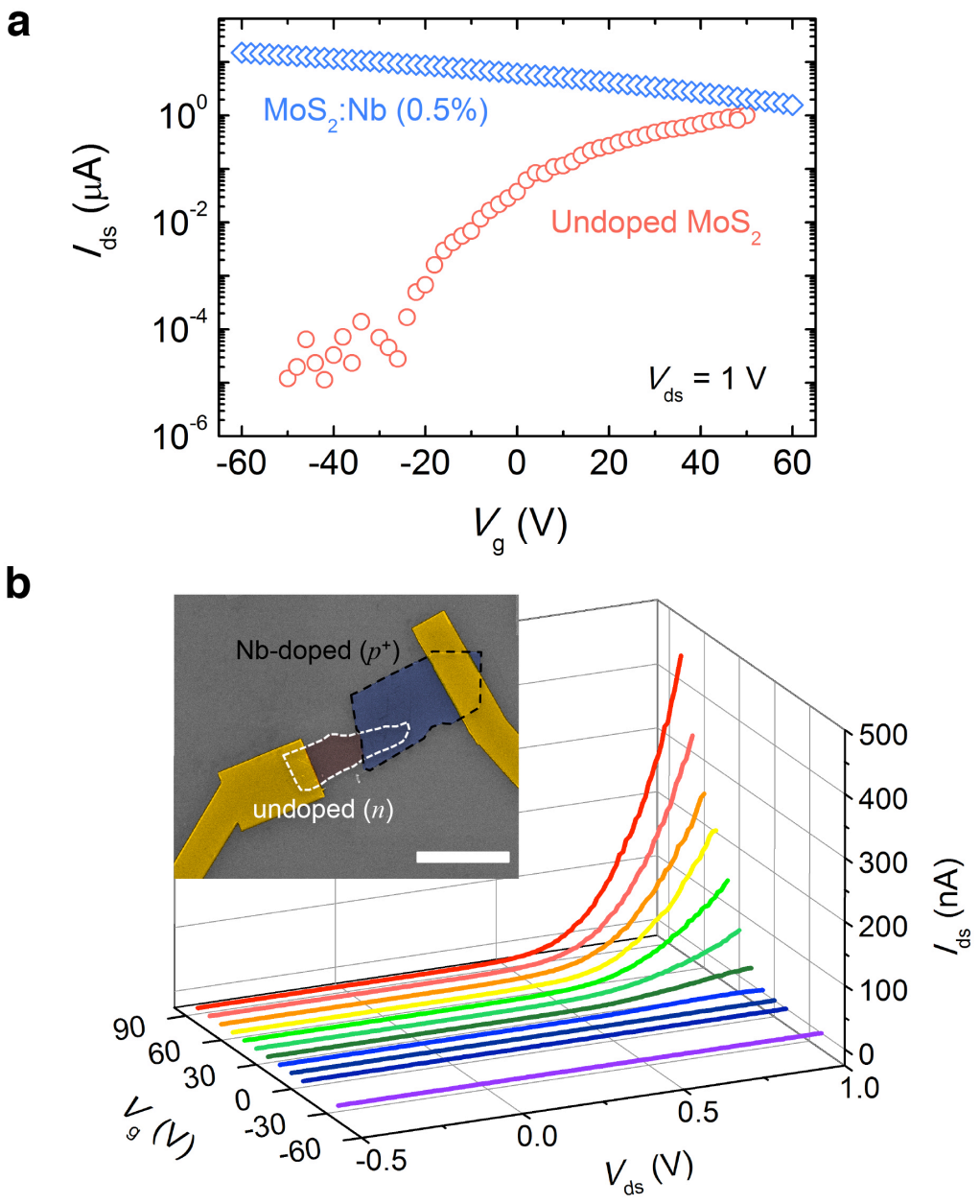

Figure 5.8. Gate-tunable rectification across a van der Waals MoS_2 *p-n* junction. (a) Gate voltage (V_g) dependence of channel current of multilayer MoS_2:Nb and undoped MoS_2 devices at a bias voltage (V_{ds}) of 1 V. Ti/Au was used for the source (s) and drain (d) contacts. (b) *I-V* characteristic at variable back-gate voltages measured across the van der Waals *p-n* junction assembled with MoS_2:Nb (60 nm) and undoped MoS_2 (4 nm). Inset is a false-color scanning electron microscopy image along with a scale bar of 10 μm.

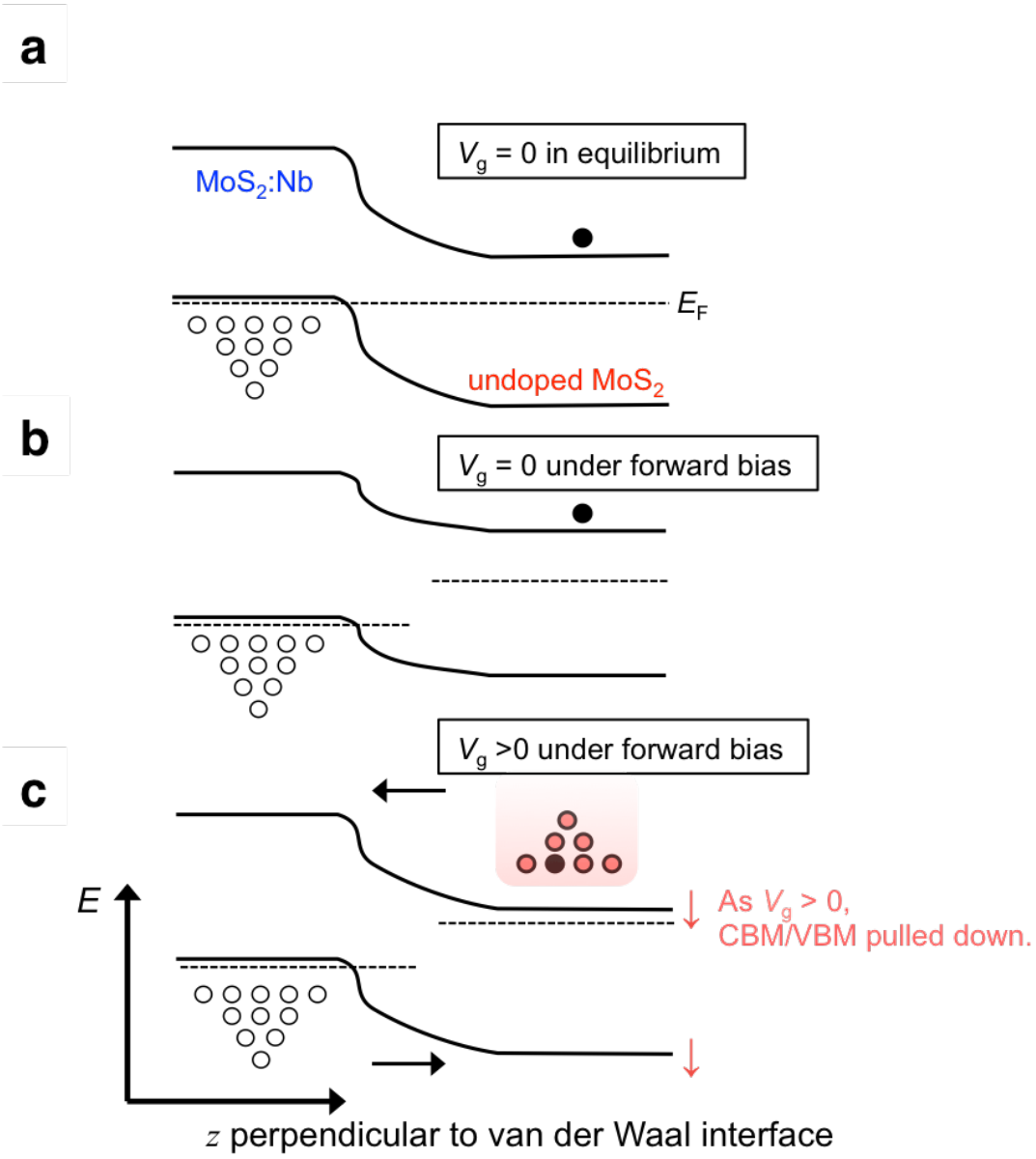

Figure 5.9. Band diagrams across vertical (z) MoS_2 p-n homojunction when no back-gate voltage (V_g) is applied in equilibrium state, and under forward bias, respectively (a and b), and a positive V_g is applied under forward bias (c). Left and right sides correspond to MoS_2:Nb (p) and intrinsic MoS_2 (n), respectively. Here, the natural band edge offset between the few-layer (~ 5 layers) and multilayer (~ 60 nm) MoS_2 is ignored.

Notably, the fabricated Hall devices and *p-n* junctions are stable in ambient air even without additional treatment such as capping layer protection, with only minimal changes in the R_{xx} and *I-V* characteristics over time (Fig. 5.10). This is in stark contrast to the existing approach of using molecular doping, which usually suffers from volatility and reactivity with air and/or water molecules. This superior stability is due to the covalently-bonded, substitutional dopants, similar to those previously observed in graphene (*e.g.,* long-term operational stability of nitrogen-doped graphene as an electrode in fuel cells). Our results also show that, thanks to the degeneracy and bipolarity of doping, one can achieve a wide tunability of current rectification as compared to the recently reported *p-n* diodes built from type-II hetero-junctions [117,118]. Moreover, distinct metals with particular work functions are not needed in making contact with the MoS_2 homo-junction devices, thus simplifying the device fabrication process.

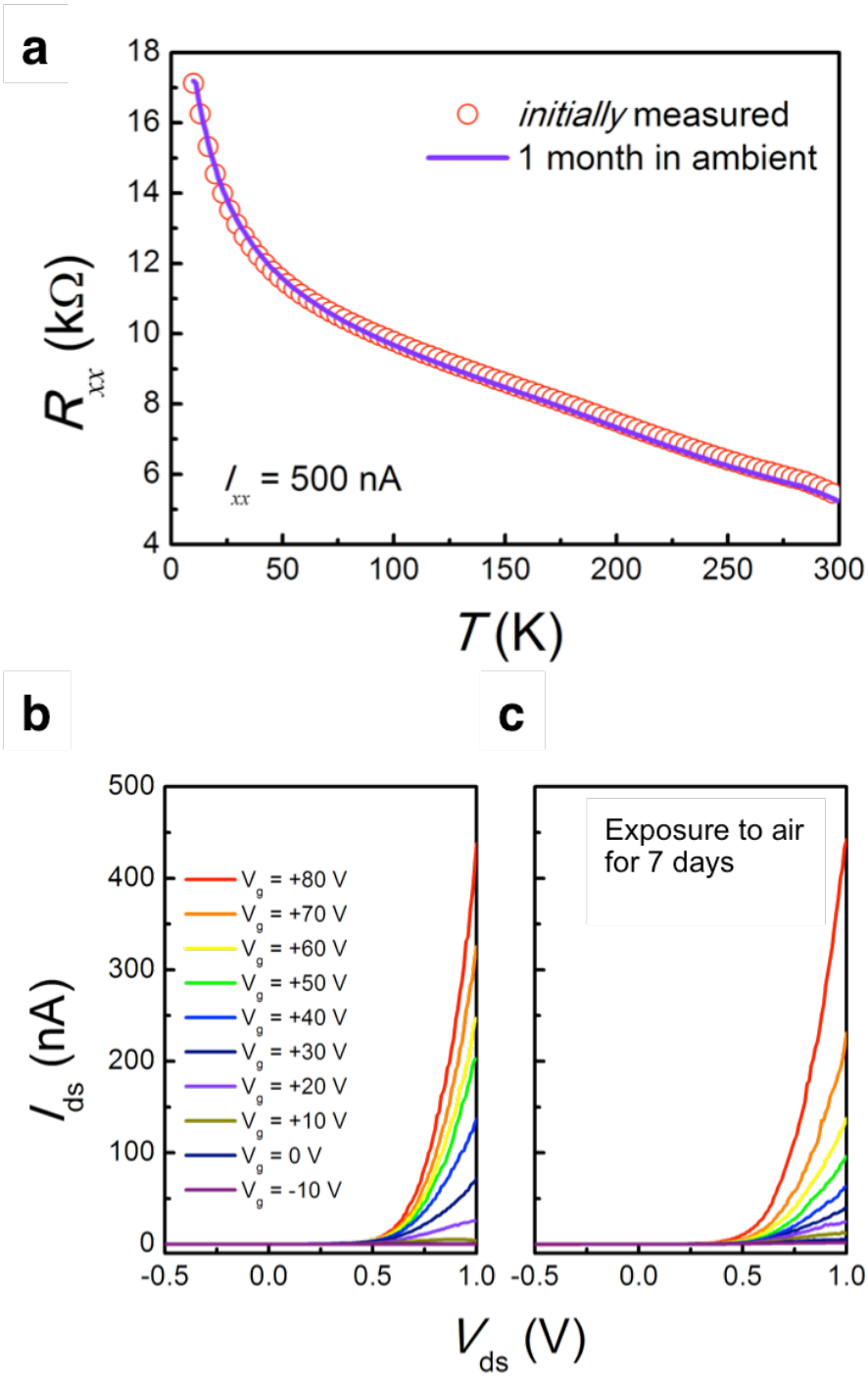

Figure 5.10. (a) Direct evidence of doping stability of a MoS_2:Nb-based device with comparison of R_{xx} measured before and after one month in ambient. (b-c) Comparison of *I-V* rectification of the MoS_2:Nb-based diode at various gating voltages before (b) and after (c) 7 days exposure to ambient air.

5.7 Summary and remarks

As the VBM of MoS_2 is located at ~ 5.4 eV, well below the vacuum level, it is challenging to find proper metals and surface-adsorbed molecules with high reduction potentials to donate holes to the VBM. Therefore, only the atomic substitution method demonstrated in this work can stabilize effective, high-density of hole doping in MoS_2. On the other hand, *ab initio* computations have predicted that both Nb (for *p*-type) and Re (for *n*-type) dopants are thermodynamically miscible on the cation site in MoX_2 and WX_2 at high temperatures, where X represents the chalcogen anion [122]. Therefore, it is expected that the CVT synthesis technique demonstrated in this work can be readily extended to doping other TMDs. To this end, a general cation substitution strategy can be developed to dope all TMDs against their native unipolar doping propensity, so as to achieve bipolar doping in these TMDs.

In summary, we demonstrate a substitutional cation doping strategy in which degenerately high concentration of free carriers are introduced in the host TMDs with covalently bonded dopants. The strategy is superior in terms of versatility and stability over other doping methods based on adsorption or intercalation of volatile species. Given the native *n*-type conduction in MoS_2, the stable *p*-type doping is of great importance for device applications, and also provides a materials platform to explore and exploit the spin-polarized valence bands of MoS_2.

Chapter 6

Conclusions and final remarks

When earnest labor brings you fame and glory,
And all earth's noblest ones upon you smile,
Remember that life's longest, grandest story
Fills but a moment in earth's little while:
"This, too, shall pass away."

LANTA W. SMITH (1856 – 1939)

In this dissertation, point defect physics in 2D layered semiconductors is refined and the relevant applications are demonstrated in the areas of environment-friendly technologies and next-generation optoelectronics. With bismuth and transition-metal chalcogenide nanostructures, synthesized by various techniques as MBE, CVD and CVT, their optical, electrical, and thermal properties are thoroughly investigated after introducing native defects and/or successfully incorporating substitutional dopants. All the observations and novel findings are well understood under a dramatic interaction between point defects and host 2D materials at reduced dimension.

Firstly, defect physics in bismuth chalcogenides is revisited in terms of their special topological surface states and unintentially conductive bulk counterpart. Intentionally introduced native defects tend to stabilize the Fermi level in the conduction band in topological insulators Bi_2Se_3, Bi_2Te_3 and their alloys. The measured electron density and mobility saturate with the Femi level stabilization at high doses of high-energy particle irradiation, similarly observed with decreasing thickness in pristine films. This implies that the defects, presumably associated with dangling bonds abundant on the

surface and/or interfaces, will result in formation of electron accumulation layers and 2D electron gas. The understanding well explains difficulties in ongoing efforts to resolve the surface transport properties of TIs, and has important implications for potential applications that utilize the unique dispersion relation of the topological states on the surface of these materials.

Furthermore, the irradiation-induced point defects uniquely enhance thermoelectric figure-of-merit *ZT* in Bi_2Te_3 by decoupling the three key thermoelectric parameters and varying all of them in the desired direction. This is enabled by the multiple functionalities of the point defects acting beneficially as electron donors, energy-dependent charge scattering centres and phonon blockers. Our results suggest that a significant improvement of the thermoelectric performance can be achieved through a judicious control of the defect densities by post-growth irradiation damage. As the point defects are expected to be generated and behave in the similar way in a wide range of narrow-bandgap semiconductors, it is possible to extend this technique to improve the heat-to-electricity efficiency of other materials with a single processing step.

As for recently developed monolayer TMDs, their optical properties are studied in a correlation with defect density. Defects induced by the alpha particle irradiation and vacuum thermal annealing dramatically enhance overall integrated PL intensity at cryogenic temperature. Also, a new peak that is below the band gap is observed. We find that the new peak at 1.75 eV originates from bound excitons that are formed after free excitons are localized by the defects. The overall enhancement in the integrated PL intensity has been attributed to the charged to free/bound exciton transition as a result of gas molecules interacting with the defect site which depletes electric charges residing in the host material.

At last, we demonstrate a substitutional cation doping strategy in which degenerately high concentration of free carriers are introduced in the host TMDs with covalently bonded dopants. The strategy is superior in terms of versatility and stability over other doping methods based on adsorption or intercalation of volatile species. Given the native *n*-type conduction in MoS_2, the stable *p*-type doping is of great importance for device applications, and also provides a materials platform to explore and exploit the spin-polarized valence bands of MoS_2.

From developing doping strategies and defect engineering for next-generation 2D optoelectronic and energy harvesting devices, through understanding fundamental point defect physics by experimental and theoretical means, this dissertation concludes with special emphasis that atomic scale defects and dopants can play greater and more various roles in 2D semiconductors than they did in 3D counterparts. Those multifunctionalities of point defects will accelerate the practical realization of 2D semiconductor-based devices supported by following future works combined with all works already achieved in this dissertation.

6.1 Future works

6.1.1 Electronic band engineering of monolayer MoS_2 with extrinsic dopants

An unusually strong band anticrossing interaction is anticipated when a substantial amount of transition metal dopants is introduced in atomically thin semiconductors due to the highly localized *d*-shell derived impurity states. A possible example is *p*-type monolayer molybdenum disulfide (MoS_2) doped with niobium (Nb). Upon atomic orbital hybridization between Nb impurity level and valence band maximum (VBM) of host MoS_2, its photoluminescence and absorption spectra will be greatly modified and display unprecedented thickness dependence since VBM is very sensitive to thickness and each valley has a different dominant orbital constituent. Combined with advance optical characterizations, it will shed light on many-body interactions in the two-dimensional limit.

6.1.2 Correlation between defect quantification and PL quantum yield

While point defects in graphene activate the Raman-active centrosymmetric A_{1g} mode well known as the D-peak, no such metric exists for quantifying defects in monolayer TMDs. From our defect-related photoluminescence study described in Chapter 4, it is suggested that bound-exciton PL can be employed for evaluating the crystal quality of monolayer semiconductors as its overall PL intensity is sensitively dependent on point defect density. This optical study can be correlated with recently developed HRTEM (and STEM)-based point defect identification and quantification of atomically thin membranes. This future work will give a rigorous and non-destructive guidance toward defects quantification of 2D materials exclusively based on their optical responses.

6.1.3 Cross-plane thermal conduction across weakly bound atomic layers

As a new family member of TMDs, rhenium disulfide (ReS_2) displays extraordinary thickness-insensitive physical properties, in stark contrast to other conventional TMDs (*e.g.,* MoS_2), and it is theoretically predicted to have much reduced out-of-plane thermal

conductivity due to its very weak interlayer coupling, arising from its distorted 1T crystal structure. Experimentally, it can be quantitatively investigated with time-domain thermoreflectance (TDTR) measurements for few-layer and bulk ReS_2 crystals. A systematic comparison with MoS_2, a representative hexagonal TMD, it will suggest that cross-plane thermal conductivity can be potentially employed as a quantitative measure of the interlayer coupling, since it depends on the stacking order as well as the strength of coupling between adjacent layers.

6.1.4 Artificial interlinking between dissimilar 2D materials

It has been widely reported that the interlayer coupling in a variety of TMDs gives rise to exotic physics such as thickness-dependent vibrational and optoelectronic properties, and they can be tuned by modulating interlayer coupling with external stimuli. Intercalation chemistry and hydrostatic pressurization using diamond anvil cell have been traditionally utilized to modulate interlayer coupling. Additionally, displaced atoms by low-dose ion irradiation can be localized between atomic layers acting as intercalates, ultimately inducing the interlinking between the layers. This new mechanism will be used to control charge transfer between dissimilar 2D semiconductors and realize other new physics.

Appendix A

Nanoscale thermoelectric effects at metal-insulator domain walls in VO_2[5]

Strongly correlated materials share a unique feature where phase transitions result in significant changes in physical properties, making these materials of particular interest for their potential device applications beyond the scope of current semiconductor technologies. Such devices are inherently complicated in nature owing to strong coupling of the crystal lattice with charge, spin, and orbital degrees of freedom of electrons. Vanadium dioxide (VO_2) is one of such materials, extensively studied as it undergoes a highly stable high- temperature metal to low-temperature insulator transition (MIT) at $T_{MIT\text{-}Bulk} \approx 340$ K. The electronic phase transition is accompanied by a structural transition in which a metallic rutile phase (M_R) converts to a semiconducting monoclinic phase (I), resulting in ~1% expansion of the lattice along the tetragonal *c*-axis (C_R). Multiple monoclinic lattice structures (I_{M1}, I_{M2}) are available for the insulating phase, which are almost optically identical and have very similar free energies, adding to the complexity of the material system. The more resistive I_{M2} phase has a lattice constant ~0.6% longer along C_R than I_{M1} and can act as an intermediate state between I_{M1} and M_R, generally associated with higher tensile strains [138,139].

[5] Reproduced in part with permission from J. Suh et al., "Direct observation of nanoscale Peltier and Joule effects at metal-insulator domain walls in vanadium dioxide nanobeams," Nano Letters **14,** 2394 Copyright 2014 American Chemical Society.

One-dimensionally aligned metal–insulator (M–I) domain configurations can be attained either by substrate-induced uniaxial strain [140] or nonuniform transition metal doping in a single-crystalline VO_2 nanobeam (NB) [141]. In the former case, M_R domains appear gradually upon heating, shifting T_{MIT} depending on the nature of external stress. Given a strong adhesive interaction with the substrate, I_{M2} phase (with longer lattice constant along C_R) becomes thermodynamically stable and the alternating M–I heterostructures are spontaneously organized (Figure A.1(a)). This substrate-mediated MIT leads to a gradual decrease in electrical resistance until VO_2 NB becomes fully metallic around ~390 K (Figure A.1(b)). Though it is generally believed that the MIT is induced by the symmetric splitting of the t_{2g} band composed of 3d vanadium states (Figure A.1(c)), the physical nature of M–I wall is still undetermined and poorly understood despite its promising electrical and thermal applications at the nanometer scale.

In this Appendix, we investigate the electro-thermal activities at M–I walls by utilizing thermoreflectance imaging microscopy to create a thermal map of VO_2 NBs under current bias in the M–I coexisting phase regime. Thus far, electrical measurements of the thermoelectric properties of VO_2 NBs have been conducted over the length of the device [142], determining effective material properties with indirect information about the domain interface. We report the direct observation of the highly localized Peltier cooling/heating and Joule heating at the M–I boundary, which acts as a thermal point source. In addition, our analysis suggests that an observed change in polarity of thermoreflectance coefficient can differentiate between the I_{M1} and I_{M2} insulating phases while our calculation of the microelastic strain on the NB M–I interface establishes each monoclinic phase to have a unique and favorable domain wall configuration. These experiments provide insight into the native M–I heterostructures of VO_2 NBs. The M–I domain walls are expected to be truly nanometer-thick, suggesting exotic functionalities at the truly nanometer length scale.

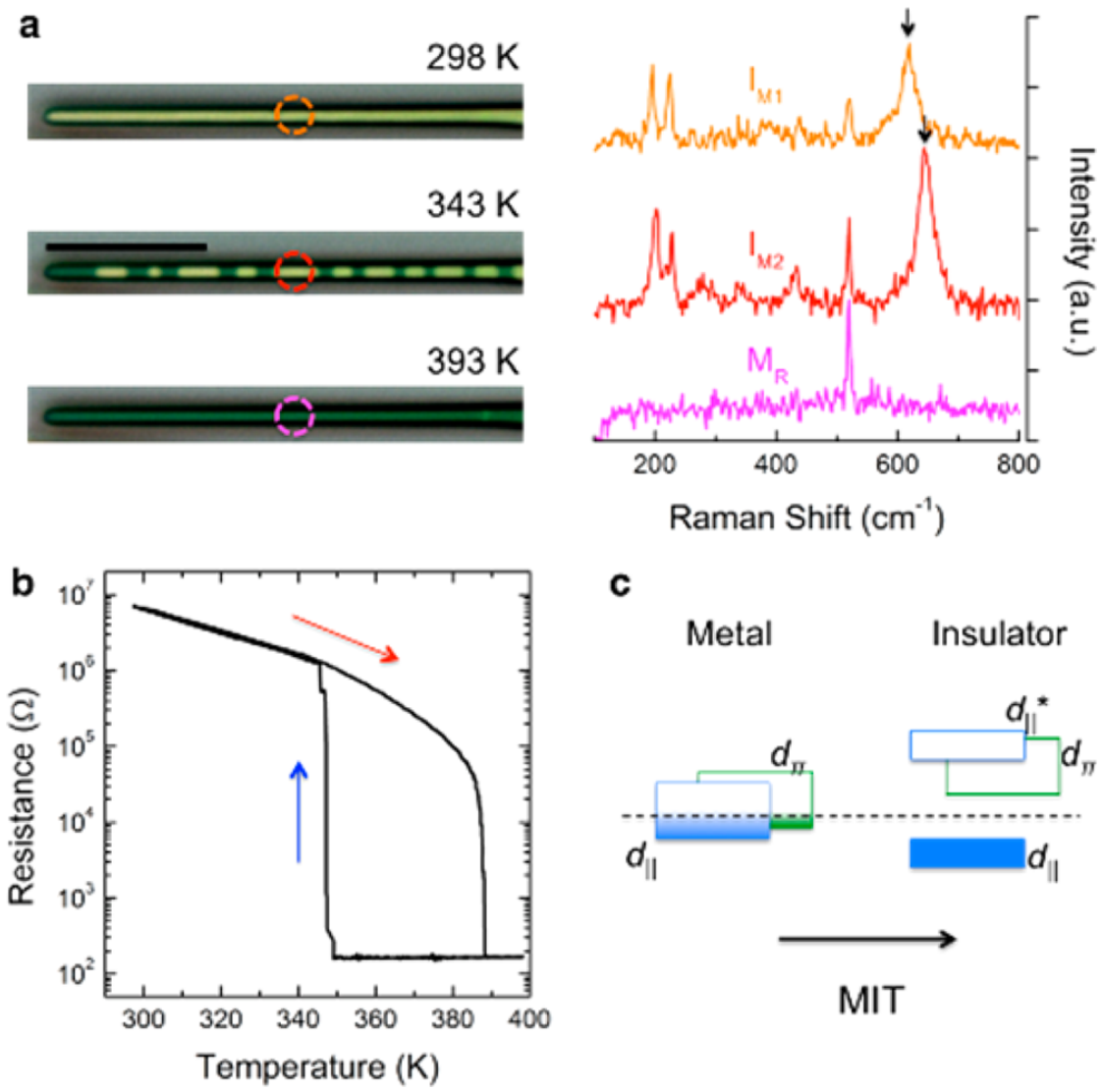

Figure A.1. Metal–insulator heterostructures along an individual VO_2 nanobeam. (a) Optical images of a typical VO2 NB upon heating from room temperature (I_{M1}) through coexisting domains (M_R and I_{M2}) to a fully metal M_R state. The physical domains are identified by Raman spectroscopy. Scale bar represents 10 μm. (b) Heating and cooling resistance as a function of temperature for device 1. (c) Band diagram for M and I phases.

The VO_2 NBs employed in this study were synthesized on 1 μm thick thermally grown SiO_2/Si substrates via a vapor transport approach [143]. These single-crystalline NBs varied in length from 20 to 250 μm and typically had a 0.5 μm^2 rectangular cross-section. Optically clean NBs were preselected, and then devices were fabricated by conventional photolithography with two or four Au/Cr contacts deposited with 10 μm

spacing using e-beam evaporation. Rapid thermal annealing at 525 K for 2 min was subsequently applied to achieve ohmic contact; negligible contact resistance was confirmed by a comparison of four-probe and two-probe I–V measurements. VO_2 NBs are naturally bonded to the SiO_2/Si substrate and experience uniaxial tensile strain along C_R (oriented as the NB long axis) as a result of high temperature growth and thermal expansion mismatch between the NB and the substrate.

We have visualized the thermal response of NB devices to electrical bias using charge-coupled device (CCD)-based thermoreflectance thermal microscopy. This noninvasive method provides two-dimensional thermal images of a sample surface with 200–300 nm spatial and 10 mK temperature resolutions. The technique relies on the small but detectable variation of the surface reflectivity with temperature, as quantified by the thermoreflectance coefficient C_{TR}, a material and illumination wavelength-dependent parameter that defines the relationship between the relative reflectivity change $\Delta R/R$ to the thermal field ΔT (relative to ambient) at the device surface: $\Delta T = (1/C_{TR})(\Delta R/R)$.

In the following experiments, we used a narrowband green LED ($\lambda \approx 530$ nm) to illuminate the VO_2 NBs through a microscope objective with ×250 magnification and monitored the reflectivity of the NBs with a scientific grade CCD camera. Green illumination selected since the C_{TR} for the contact material (Au) is well-known at this wavelength. The thermal images presented in this Appendix assume a uniform C_{TR} of -2×10^{-4} K^{-1}. The NB substrate was mounted with a thin layer of thermal paste onto a Peltier heater for ambient temperature control. We then applied a 3.75 Hz sinusoidal voltage across (multiple) segments of the NB to create a slowly oscillating thermal field. The bias period was several orders of magnitude longer than the typical thermal response times of devices this size, ensuring that the NBs were operating in the quasi-static thermal regime. Bias current amplitudes were limited to ~15 μA such that the NB domains were not displaced by electro-thermal effects [144] in the M–I coexisting state. We employed the minimum possible current bias that induced a measurable signal while remaining in the linear regime of the *I-V* curve for the NB. We continuously monitored the optical image during the measurement to ensure the stable configuration of M–I heterostructures along NBs.

The phase-locked CCD captured a periodic sequence of 8 images corresponding to eighth-period integrals of the reflectance signal under sinusoidal excitation. Data were averaged over ~500 periodic cycles to achieve sufficient signal-to-noise ratios. Adequate mathematical processing provided the magnitude and relative phase of the first and second harmonic components of the reflectivity field. This corresponds to a separation of the Peltier and Joule terms in the thermal field, given their respective linear (first harmonic) and quadratic (second harmonic) current dependencies.

Several NBs were examined in this manner, and it became apparent that each NB could be categorized into one of two observed trends depending on the strength of the

attachment to the substrate (hence built-in strain): the first type exhibited periodic domain configuration and had a smooth decrease in resistance with temperature as described in Figure A.1. The second type of NB displayed few and irregular domain formation, accompanied by a distinct jump in electrical resistance around T_{MIT}. For clarity, representative examples of each category, designated device 1 and device 2, respectively, are analyzed in this Appendix.

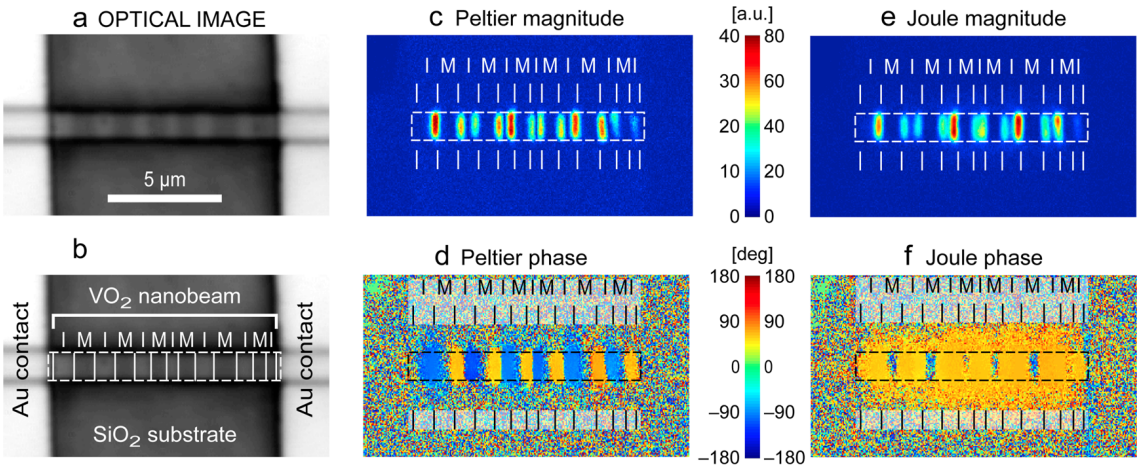

Figure A.2. Thermoreflectance thermal images of device 1 taken at 355 K under 10 μA applied current. (a,b) Optical images of the nanobeam (greyscale). (c,d) Peltier temperature magnitude and phase images, respectively. (e,f) Joule temperature magnitude and phase images. While both Peltier and Joule signals are localized at the interfaces, phase images show very different dynamics of how alternating Peltier cooling and heating in nearby interfaces exchange energy mainly through the nanobeam. However, there is no cancellation in the Joule activity, and Joule heating is propagating in the substrate.

We first present results for a VO_2 NB (device 1), which exhibited the typical periodic domain configuration; Raman spectroscopy (Figure A.1(a)) established this device was in the M_R–I_{M2} phase coexisting state [139]. Thermal images of the NB taken at 355 K under an applied 10 μA sinusoidal current are presented in Figure A.2. As discussed, periodic domains are indicative of homogeneous substrate adhesion and are clearly observed in the optical image depicted in Figure A.2(a,b) (greyscale image); this domain configuration remained stationary for the duration of the thermoreflectance measurement. Figure A.2(c,e) displays the temperature magnitudes of the Peltier and Joule signals, respectively. Both signals originate in the interface regions between metal and insulator domains, which behave as thermal point sources. We expect to see Peltier heating or cooling at the M–I junction given the presence of an energy barrier [145]. In this case, the signal may not be fully resolvable in an optical measurement due to the

diffraction limit. However, Joule heating is also concentrated at the M–I junction indicative of a significant resistance of the domain wall (R_{DW}) between the metallic and insulating domains. For the specific current amplitude depicted in these figures, Joule heating is stronger than the magnitude of Peltier and is consequently better resolved; the average ratio of the Joule magnitude to that of Peltier (J/P) is ~1.75. It is interesting to note that while R_{DW} plays a minor role from an electrical standpoint (relative to the overall NB resistance), it is crucial from the perspective of the local thermal behavior of the NB. Thermal imaging reveals that the associated resistance is comprised in a very small region, leading to power densities at the M–I junction that are much higher than that along the length of the NB. Highly localized Joule heating may also be attributed to the band offset between M and I domains through the possible introduction of an associated depletion region; however, the exact nature of the junction is still unknown.

Phase information from the thermal signal can be much more revealing as it is quite sensitive to small variations in the thermal distribution across the sample. The thermal response time of the NB is approximately 5 orders of magnitude shorter than the period of the applied current, leading to uniform thermal phase. Thus, any deviations in the phase image are due to bipolar behavior (cooling instead of heating) or sign changes in the C_{TR}. The Peltier phase image (Figure A.2(d)) depicts both heating and cooling localized at the M–I interfaces: when one interface is heating (under forward bias), the neighboring interface is clearly cooling (under reverse bias) denoted by the 180° phase shift. As expected, the Joule signal (Figure A.2(f)) does not exhibit this phase shift and is always heating.

While the Peltier signal is seemingly concentrated inside the insulating region, we expect the actual thermal activity to also present in the metal region. We attribute the apparent lack of thermal signal over the metallic state to a small thermoreflectance coefficient, as the images are based on a uniform C_{TR} calibrated for Au only. Phase-shifted Joule activity is evident in the metal regions of the NB and into the substrate owing to its stronger signal but is not visible in the magnitude images. To explain this result, the C_{TR} of the metal phase must be of opposite sign and significantly smaller in magnitude than that of the insulating state. It is evident in Figure A.2(f) that the supporting substrate of the sample also functions as a heat sink for Joule heating. The signal spreads outward uniformly from its peak at the domain walls, demonstrating good thermal contact between the NB and the substrate. The lack of Peltier substrate activity is not simply because of its lesser signal magnitude. Heating and cooling signals at nearby domain walls are mainly coupled through the nanobeam with little leakage into the substrate; this interaction may diminish the overall Peltier magnitude in this device. Through inspection of the phase images, we can confirm that the resultant reflectivity signals are due to thermal fluctuations and not movement at the domain boundaries. The uniform thermal signals at the interfaces occur over a larger width than expected for edge effects from movement not observed optically. In addition, the point source-like behavior with

continuous activity into other regions of the image (nearby substrate) would not be possible.

The apparent total strain (and thus domain pattern) differed between samples due to nonuniform substrate adhesion, variations in growth temperature, and stress induced by the end-to-end clamping by the contacts. In this sense, NBs with a nonperiodic M–I domain pattern are possible and display quite different temperature-dependent behavior, as is shown in Figure A.3 for a sample (device 2) held at 348 K. Current was applied across two consecutive segments of the NB (Figure A.3(a,f)); referred to in this Appendix as the right-hand side (RHS) segment and the left-hand side (LHS) segment. Irregular domain patterns nucleated from the side contacts at 328 K, a much lower ambient temperature as compared to device 1 and considering $T_{\text{MIT-Bulk}}$. The domain walls in both segments were initially at a ~50° angle relative to the NB long axis. The domain configuration and angled domain walls of this NB can be indicative of nonuniform stress distribution along the length and width of the NB [140], suggesting weak substrate interaction and/or clamping strain from the Au contacts.

For the thermoreflectance measurement, we applied sinusoidal current at varying amplitudes, ranging from 5 to 10 μA, very similar in magnitude to the previous NB as this was the minimum necessary to resolve the Peltier signal. After one measurement run at 8 μA bias, the domain configuration on the RHS changed from M–I–M with angled domain walls (Figure A.3(a–e)) to M–I with a single vertical wall (Figure A.3(f–j)), possibly due to excessive Joule heating at the interface. The new domain configuration was stable for all subsequent measurements.

The magnitude of Peltier temperature in the RHS segment was very similar to that of uniformly clamped NB (Figure A.2(c)); however, Joule heating was substantially greater. For the same current bias applied for device 1 (10 μA), $J/P_{RHS} \approx 7$ and $J/P_{LHS} \approx 5$. Such significant Joule heating, especially on the RHS, could drive the domains to another insulating state (from I_{M1} to I_{M2}). These highly localized junction Peltier and Joule effects are also responsible for M–I domain wall propagation along the VO_2 NBs at high currents (well above those used during the measurement), as previously reported in suspended $W_xV_{1-x}O_2$ NBs [144]. This is especially true for device 2, as the NB does not dissipate Joule heating well into the substrate possibly due to weaker adhesion. The resultant phase oscillation could be controlled and sustained with the addition of a parallel capacitor by repeating the charging and discharging process.

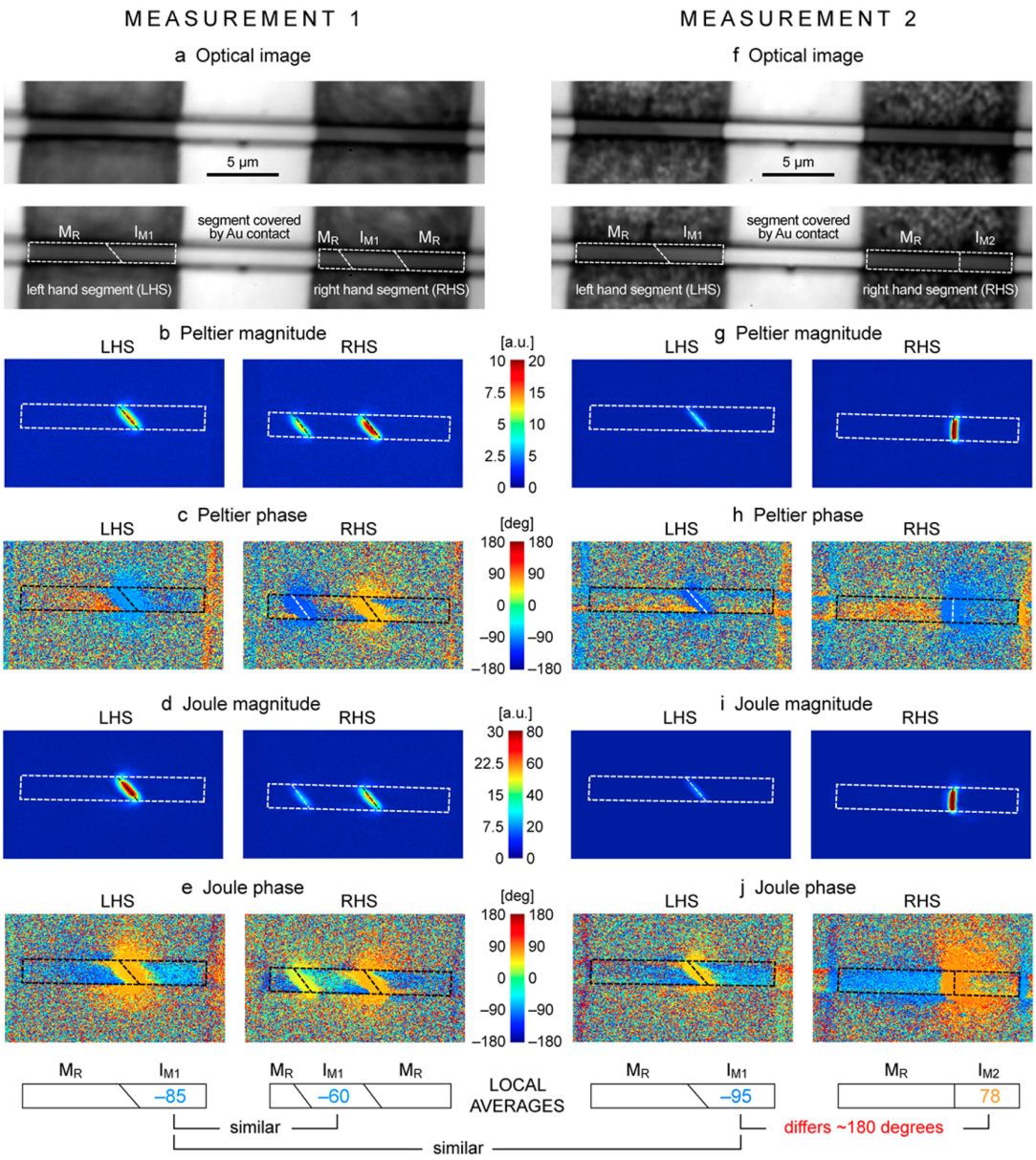

Figure A.3. Thermal images of nonperiodic nanobeam (device 2) at 348 K under 8 μA current excitation. Two NB segments and the adjoining electrode region are under current bias. (a–e) Initial thermoreflectance measurement images of device 2 before the RHS segment changed from M– I–M to M–I domain configuration. (f–j) Thermal images for the same current bias taken after the RHS segment stabilized. As domain walls are at substantial distances from each other, both Joule and Peltier phase images show heat exchange mainly with the substrate. Also note the change in the phase of the Joule heating in the RHS segment, which is an indication of different thermoreflectance coefficient for the two insulating phases.

The phase images of both Peltier (Figure A.3(c,h)) and Joule (Figure A.3(e,j)) confirm the earlier premise that the signals occur at the domain walls. The typical spreading pattern from a thermal point source is detected along the NB and into the substrate. The relative signal strengths along the NB show heat diffuses preferentially in the metal region of the RHS segment, possibly owing to its higher thermal conductivity [146]. Activity along the Au-covered-NB region gives us a reference value for C_{TR}, as this is known to be negative for Au at this illumination wavelength. From this and the expected uniformity of the Joule phase activity, we gain valuable insight about C_{TR} of the other regions. C_{TR} of the metal domains is always positive, while the C_{TR} of the insulator domain on the RHS segment of measurement 2 is negative (Figure A.3(j), RHS), similar to the scenario presented for device 1 in Figure A.2. However, the insulating state in the LHS segment during the same measurement is roughly 180° out of phase from the aforementioned insulator domains, implying a positive C_{TR} (Figure A.3(j), LHS). We believe that the difference in the sign of C_{TR} between these two insulating domains distinguishes the two monoclinic phases of VO_2; that is, the reflectivity dependence on temperature variations has the opposite behavior for the two monoclinic states. This is in agreement with the phase information for the RHS segment before the change to the single vertical domain wall; the insulator domain on the RHS during measurement 1 (Figure A.3(e)) is roughly 180° phase shifted from the I domain in the RHS during measurement 2 (Figure A.3(j)) for the same excitation bias. For clarity, the average phase values of the NB regions associated with this analysis are presented below the phase images in Figure A.3(e,j). The significant change in the thermoreflectance properties between the two insulating phases could be attributed to the difference in reflective signatures of the two monoclinic phases under polarized light. Further thermoreflectance measurements using a polarized light source would illuminate the underlying mechanism of the C_{TR} sign change.

We applied Khachaturyan's microelasticity theory for a single coherent inclusion in the matrix of a parent phase to analyze the elastic energy and thus orientation of the M–I interface of a VO_2 NB in an attempt to understand the change in domain wall alignment. Both the M_R/I_{M1} and M_R/I_{M2} junctions are considered coherent. Both rutile–monoclinic structural transitions have four possible variants each with different stress-free transformation strains, leading to eight possible domain wall configurations all with minimized elastic energy density. The favored orientation exhibits reduced total elastic energy, which is related to the geometry of NB; accordingly, M_R/I_{M1} will favor an acute angle of 56° (Figure A.4) with the NB top surface, while M_R/I_{M2} may display an 89° (Figure A.4) or 33° acute angle. This is consistent with the experimentally observed angles of devices 1 and 2 whose insulating states are identified through the sign of C_{TR} during thermoreflectance imaging: the M_R/I_{M1} domain wall exhibits an angle of 48–52° and M_R/I_{M2} presents as a 90° interface (Figures A.2 and A.3).

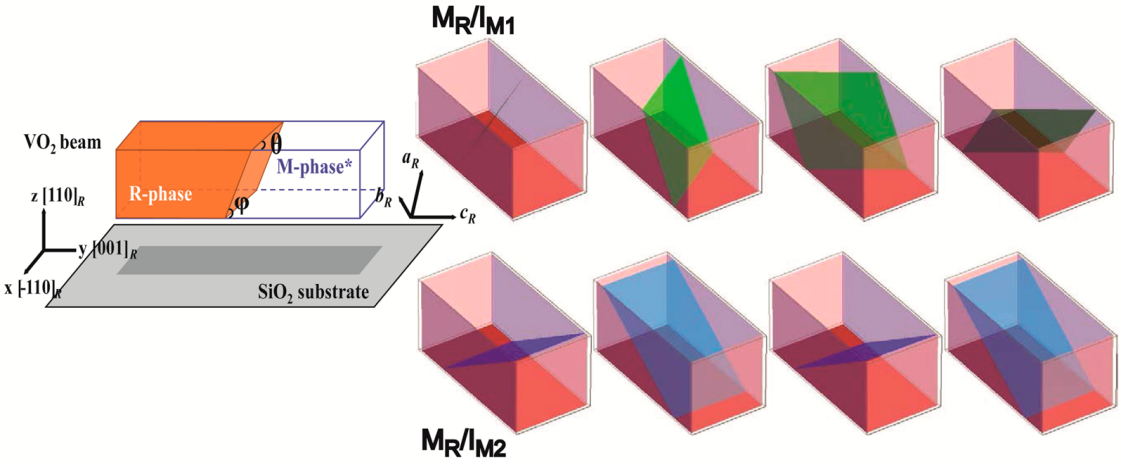

Figure A.4. Three-dimensional plots of possible habit planes for θ = 56° M_R/I_{M1} (green) and θ = 89° M_R/I_{M2} (blue). These habit planes exhibit minimized total elastic energy for the interface and are thus considered favorable.

Further evidence identifying the insulating phases of device 1 and 2 is obtained by examining the resistance trend with ambient temperature of the two NBs (Figure A.5). Device 2 exhibits a large jump in resistance at 335 K, coinciding with the appearance of the first metal domain. This implies that either R_{DW} is quite large, ~300 kΩ, or that I_{M1} converted to the more resistive I_{M2} insulating state, similar to the behavior described in Kasirga et al [138]. In contrast, device 1 shows a fairly steady decrease in resistance before becoming fully metallic. Both NBs display the expected Arrhenius behavior for a nondegenerately doped semiconductor before the metal domains emerge, $R_I(T) = R_{I,0}e^{E_a/k_BT}$. However, device 2 has a markedly lower overall resistance despite similar sample geometries; thus, the two NBs have quite dissimilar activation energy: $E_{a(dev1)}$ = 0.3 eV and $E_{a(dev2)}$ = 0.11 eV; both are consistent with values reported in the literature ranging from 0.08 to 0.36 eV [145]. The lower activation energy suggests device 2 to be more highly doped. When the domains coexist, the total resistance R_T of the NB is composed of four factors:

$$R_T(T) = x(T)R_I(T) + [1 - x(T)]R_M(T) + R_C + R_{DW} \quad \text{(A.1)}$$

where $x(T)$ is the length fraction of the NB in the I state at a given ambient temperature, and R_I and R_M are the expected insulating and metal resistances, respectively. The contact resistance, R_C, was shown to be negligible. We used this equation and the extrapolated Arrhenius fitting at multiple ambient temperatures to determine R_{DW} of the more uniform NB (device 1), which we found to be 39 ± 7 kΩ.

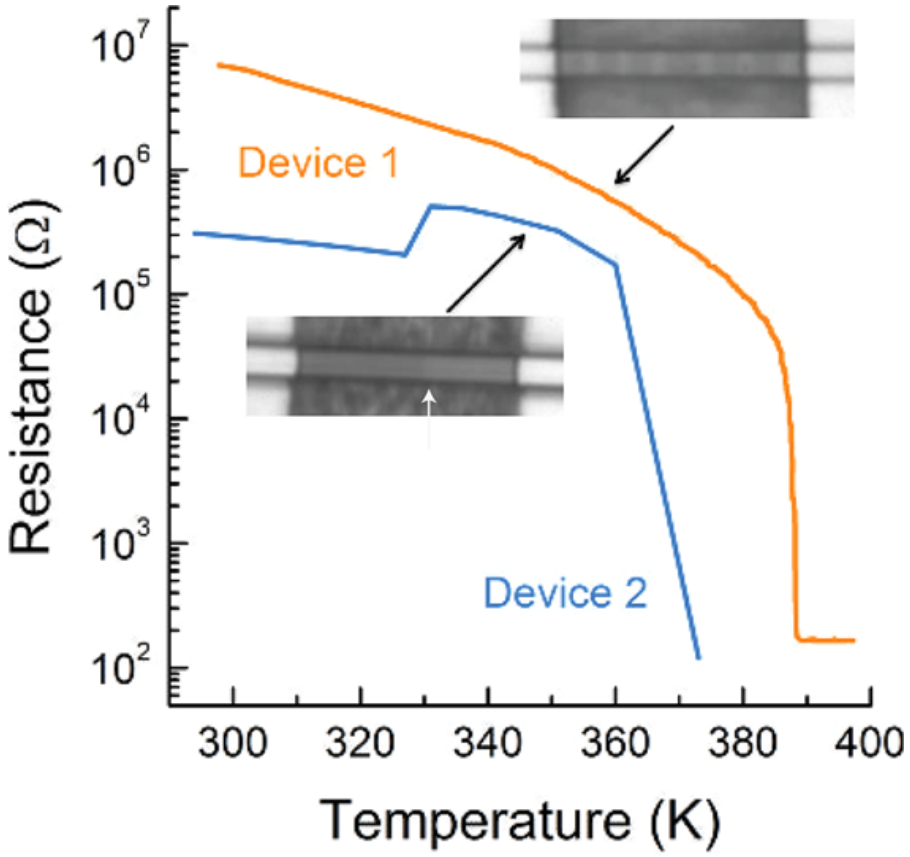

Figure A.5. Resistance as a function of ambient temperature comparison of the two NBs: devices 1 and 2. Device 2 exhibits a jump in resistance coincident with the emergence of metallic domains due to the conversion from I_{M1} to I_{M2} and the additional resistance of the domain walls.

The jump in resistance, sign change of the C_{TR}, and transformation of the interface angle of device 2 denote the change in monoclinic crystal structure in the M–I coexisting state. $T_{MIT\text{-}dev2}$ is a lower temperature than $T_{MIT\text{-}Bulk}$, indicating compressive strain driving the NB to the phases with smaller lattice constants (M_R and I_{M1}). The irregular domain patterns in addition to strong Joule activity at the M–I interface suggest poor substrate bonding, which would reduce tensile stress felt by the NB upon cooling from the high growth temperature (~1000 °C). Thus, device 2 was initially in the I_{M1} state. At elevated temperatures, the appearance of metal domains alleviates compressive strain while inducing tensile strain in the adjacent insulating domain. The induced strain, accompanied by intense Joule heating in the RHS segment generated by the current applied during the measurement, stimulated the conversion from I_{M1} phase to I_{M2}.

VO_2 NBs with good substrate adhesion would experience tensile strain at the temperatures of this experiment. Homogenous periodicity and uniform thermal signal in the substrate demonstrate uniaxial tensile strain in device 1 along the NB long axis, fixing the insulating phase to the I_{M2} phase with a longer lattice constant. The higher overall resistance and the persistence of I domains with vertical interfaces to 390 K, well above $T_{MIT\text{-}Bulk}$, further support this assertion. The sign of the C_{TR} of the I phase in device 1 is negative and is therefore I_{M2}, in agreement with the analysis of device 2 and confirmed by Raman spectroscopy.

In conclusion, our results directly reveal the extremely local Peltier and Joule effects across the M–I domain walls. Thermal images show that alternating Peltier heating and cooling at neighboring domain interfaces exchange energy through the nanobeam; while Joule heating dissipates in the substrate. We show that significant domain wall resistance is responsible for concentrated Joule heating. The insight gained through thermoreflectance imaging and the ability to distinguish between insulating phases illuminate the underlying impact of stress on the nanobeam, while examination of the elastic energy at the interface determines the favored wall configurations to minimize the total elastic strain for each monoclinic phase.

Biblography

[1] J. Moore, Topological insulators: The next generation. *Nature Physics* **5**, 378 (2009).

[2] L. Fu, C. L. Kane, and E. J. Mele, Topological insulators in three dimensions. *Physical Review Letters* **98**, 106803 (2007).

[3] Y. L. Chen *et al.*, Experimental realization of a three-dimensional topological insulator, Bi_2Te_3. *Science* **325**, 178 (2009).

[4] T. Zhang *et al.*, Experimental demonstration of topological surface states protected by time-reversal symmetry. *Physical Review Letters* **103**, 266803 (2009).

[5] D. Kim *et al.*, Surface conduction of topological dirac electrons in bulk insulating Bi_2Se_3. *Nature Physics* **8**, 459 (2012).

[6] N. Bansal, Y. Kim, M. Brahlek, E. Edrey, and S. Oh, Thickness-independent transport channels in topological insulator Bi_2Se_3 thin films. *Physical Review Letters* **109**, 116804 (2012).

[7] L. Fu and C. L. Kane, Superconducting proximity effect and majorana fermions at the surface of a topological insulator. *Physical Review Letters* **100**, 096407 (2008).

[8] X. L. Qi, R. Li, J. Zang, and S.-C. Zhang, Inducing a magnetic monopole with topological surface states. *Science* **323,** 1184 (2009).

[9] R. Yu *et al.*, Quantized anomalous hall effect in magnetic topological insulators. *Science* **329**, 61 (2010).

[10] J. J. Cha *et al.*, Weak antilocalization in $Bi_2(Se_{(x)}Te_{(1-x)})_3$ nanoribbons and nanoplates. *Nano Letters* **12**, 1107 (2012).

[11] M. Bianchi *et al.*, Coexistence of the topological state and a two-dimensional electron gas on the surface of Bi_2Se_3. *Nature Communications* **1**, 128 (2010).

[12] C. E. ViolBarbosa *et al.*, Direct observation of band bending in the topological insulator Bi_2Se_3. *Physical Review B* **88**, 195128 (2013).

[13] C. Chen *et al.*, Robustness of topological order and formation of quantum well states in topological insulators exposed to ambient environment. *Proceedings of the National Academy of Sciences USA* **109**, 3694 (2012).

[14] M. T. Pettes, J. Maassen, I. Jo, M. S. Lundstrom, and L. Shi, Effects of surface band bending and scattering on thermoelectric transport in suspended bismuth telluride nanoplates. *Nano Letters* **13,** 5316 (2013).

[15] X. He *et al.*, Surface termination of cleaved Bi_2Se_3 investigated by low energy ion scattering. *Physical Review Letters* **110**, 156101 (2013).

[16] P. M. Coelho *et al.*, Temperature-induced coexistence of a conducting bilayer and the bulk-terminated surface of the topological insulator Bi_2Te_3. *Nano Letters* **13**, 4517 (2013).

[17] W. Walukiewicz, Intrinsic limitations to the doping of wide-gap semiconductors. *Physica B* **302-303**, 123 (2001).

[18] X. Liu *et al.*, Characterization of Bi_2Te_3 and Bi_2Se_3 topological insulators grown by MBE on (001) GaAs substrates. *Journal of Vacuum Science & Technology B: Microelectronics and Nanometer Structures* **30**, 02B103 (2012).

[19] X. Liu *et al.*, in *Bismuth-containing compounds,* H. Li, Z. M. Wang, Eds. (Springer, New York, 2013), vol. 186, chap. 11, pp. 263.

[20] S. R. Messenger *et al.*, Nonionizing energy loss (NIEL) for heavy ions. *IEEE Transactions on Nuclear Science* **46**, 1595 (1999).

[21] N. P. Butch *et al.*, Strong surface scattering in ultrahigh-mobility Bi_2Se_3 topological insulator crystals. *Physical Review B* **81**, 241301 (2010).

[22] H. Scherrer and S. Scherrer, in *Thermoelectrics handbook: Macro to nano,* D. M. Rowe, Ed. (CRC Boca Raton, 2006), chap. 27, pp. 1.

[23] W. Walukiewicz, Amphoteric native defects in semiconductors. *Applied Physics Letters* **54**, 2094 (1989).

[24] E. Kioupakis, M. L. Tiago, and S. G. Louie, Quasiparticle electronic structure of bismuth telluride in the GW approximation. *Physical Review B* **82**, 245203 (2010).

[25] D. Haneman, Photoelectric emission and work functions of InSb, GaAs, Bi_2Te_3 and germanium. *Journal of Physics and Chemistry of Solids* **11**, 205 (1959).

[26] S. Li *et al.*, Fermi-level stabilization energy in group III nitrides. *Physical Review B* **71**, 161201(R) (2005).

[27] A. X. Levander *et al.*, Effects of point defects on thermal and thermoelectric properties of InN. *Applied Physics Letters* **98**, 012108 (2011).

[28] D. T. Speaks *et al.*, Fermi level stabilization energy in cadmium oxide. *Journal of Applied Physics* **107**, 113706 (2010).

[29] P. King *et al.*, Unification of the electrical behavior of defects, impurities, and surface states in semiconductors: Virtual gap states in CdO. *Physical Review B* **79**, 035203 (2009).

[30] W. Zawadzki and W. Szymanska, Elastic electron scattering in InSb-type semiconductors. *Physica Status Solidi (b)* **45**, 415 (1971).

[31] E. O. Kane, Band structure of indium antimonide. *Journal of Physics and Chemistry of Solids* **1**, 249 (1957).

[32] J. Wu *et al.*, Effects of the narrow band gap on the properties of InN. *Physical Review B* **66**, 201403 (2002).

[33] W. Richter, H. Kohler, and C. R. Becker, A raman and far-infrared investigation of phonons in the rhombohedral V-VI compounds. *Physica Status Solidi (b)* **84**, 619 (1977).

[34] B.-L. Huang and M. Kaviany, Ab initio and molecular dynamics predictions for electron and phonon transport in bismuth telluride. *Physical Review B* **77**, 125209 (2008).

[35] S. K. Mishra, S. Satpathy, and O. Jepsen, Electronic structure and thermoelectric properties of bismuth telluride and bismuth selenide. *Journal of Physics: Condensed Matter* **9**, 461 (1996).

[36] J. G. Analytis *et al.*, Bulk Fermi surface coexistence with dirac surface state in Bi_2Se_3: A comparison of photoemission and Shubnikov–de Haas measurements. *Physical Review B* **81**, 205407 (2010).

[37] A. A. Taskin, S. Sasaki, K. Segawa, and Y. Ando, Manifestation of topological protection in transport properties of epitaxial Bi_2Se_3 thin films. *Physical Review Letters* **109**, 066803 (2012).

[38] W. Walukiewicz, Mechanism of schottky barrier formation: The role of amphoteric native defects. *Journal of Vacuum Science & Technology B: Microelectronics and Nanometer Structures* **5**, 1062 (1987).

[39] J. Wu *et al.*, Effects of electron concentration on the optical absorption edge of InN. *Applied Physics Letters* **84**, 2805 (2004).

[40] P. D. C. King *et al.*, Large tunable Rashba spin splitting of a two-dimensional electron gas in Bi_2Se_3. *Physical Review Letters* **107**, 096802 (2011).

[41] S. Chu and A. Majumdar, Opportunities and challenges for a sustainable energy future. *Nature* **488**, 294 (2012).

[42] C. J. Vineis, A. Shakouri, A. Majumdar, and M. G. Kanatzidis, Nanostructured thermoelectrics: Big efficiency gains from small features. *Advanced Materials* **22**, 3970 (2010).

[43] A. Shakouri, Recent developments in semiconductor thermoelectric physics and materials. *Annual Review of Materials Research* **41**, 399 (2011).

[44] K. Biswas *et al.*, High-performance bulk thermoelectrics with all-scale hierarchical architectures. *Nature* **489**, 414 (2012).

[45] R. Venkatasubramanian, E. Siivola, T. Colpitts, and B. O'Quinn, Thin-film thermoelectric devices with high room-temperature figures of merit. *Nature* **413**, 597 (2001).

[46] X. Yan *et al.*, Experimental studies on anisotropic thermoelectric properties and structures of *n*-type $Bi_2Te_{2.7}Se_{0.3}$. *Nano Letters* **10**, 3373 (2010).

[47] B. Poudel *et al.*, High-thermoelectric performance of nanostructured bismuth antimony telluride bulk alloys. *Science* **320**, 634 (2008).

[48] J. P. Fleurial, L. Gailliard, R. Triboulet, H. Scherrer, and S. Scherrer, Thermal properties of high quality single crystals of bismuth telluride: Part 1: Experimental characterization. *Journal of Physics and Chemistry of Solids* **49**, 1237 (1988).

[49] Y. Min *et al.*, Surfactant-free scalable synthesis of Bi_2Te_3 and Bi_2Se_3 nanoflakes and enhanced thermoelectric properties of their nanocomposites. *Advanced Materials* **25**, 1425 (2012).

[50] P. Ghaemi, R. Mong, and J. Moore, In-plane transport and enhanced thermoelectric performance in thin films of the topological insulators Bi_2Te_3 and Bi_2Se_3. *Physical Review Letters* **105**, 166603 (2010).

[51] J. O. Jenkins, J. A. Rayne, and R. W. Ure, Elastic moduli and phonon properties of Bi_2Te_3. *Physical Review B* **5**, 3171 (1972).

[52] Y. S. Kim *et al.*, Thickness-dependent bulk properties and weak antilocalization effect in topological insulator Bi_2Se_3. *Physical Review B* **84**, 073109 (2011).

[53] T. Borca-Tasciuc, A. R. Kumar, and G. Chen, Data reduction in 3ω method for thin-film thermal conductivity determination. *Review of Scientific Instruments* **72**, 2139 (2001).

[54] J. Suh *et al.*, Fermi-level stabilization in the topological insulators Bi_2Se_3 and Bi_2Te_3: Origin of the surface electron gas. *Physical Review B* **89**, 115307 (2014).

[55] W. Walukiewicz, Mechanism of Fermi-level stabilization in semiconductors. *Physical Review B* **37**, 4760 (1988).

[56] D. O. Scanlon *et al.*, Controlling bulk conductivity in topological insulators: Key role of anti-site defects. *Advanced Materials* **24**, 2154 (2012).

[57] D. West, Y. Sun, H. Wang, J. Bang, and S. Zhang, Native defects in second-generation topological insulators: Effect of spin-orbit interaction on Bi_2Se_3. *Physical Review B* **86**, 121201(R) (2012).

[58] M. S. Bahramy *et al.*, Emergent quantum confinement at topological insulator surfaces. *Nature Communications* **3**, 1159 (2012).

[59] R. L. Petritz, Theory of an experiment for measuring the mobility and density of carriers in the space-charge region of a semiconductor surface. *Physical Review* **110**, 1254 (1958).

[60] R. Jones *et al.*, Evidence for *p*-type doping of InN. *Physical Review Letters* **96**, 125505 (2006).

[61] H. J. Goldsmid, *Introduction to thermoelectricity*. (Springer, Heidelberg, Germany, 2010).

[62] J. Cai and G. Mahan, Effective Seebeck coefficient for semiconductors. *Physical Review B* **74**, 075201 (2006).

[63] F. D. Rosi, Thermoelectricity and thermoelectric power generation. *Solid-State Electronics* **11,** 833 (1968).

[64] L. Hu *et al.*, Enhancement in thermoelectric performance of bismuth telluride based alloys by multi-scale microstructural effects. *Journal of Materials Chemistry* **22**, 16484 (2012).

[65] C. Dames and G. Chen, 1ω, 2ω, and 3ω methods for measurements of thermal properties. *Review of Scientific Instruments* **76**, 124902 (2005).

[66] P. G. Klemens, The scattering of low-frequency lattice waves by static imperfections. *Proceedings of the Physical Society* **68A**, 1113 (1955).

[67] O. Madelung, *Semiconductors: Data handbook*. (Springer, 2004).

[68] C. B. Satterthwaite and R. W. Ure, Electrical and thermal properties of Bi_2Te_3. *Physical Review* **108**, 1164 (1957).

[69] H. J. Goldsmid, The thermal conductivity of bismuth telluride. *Proceedings of the Physical Society Section B* **69**, 203 (1956).

[70] F. Yang, T. Ikeda, G. J. Snyder, and C. Dames, Effective thermal conductivity of polycrystalline materials with randomly oriented superlattice grains. *Journal of Applied Physics* **108**, 034310 (2010).

[71] F. Yang and C. Dames, Mean free path spectra as a tool to understand thermal conductivity in bulk and nanostructures. *Physical Review B* **87**, 035437 (2013).

[72] H. J. Goldsmid, Heat conduction in bismuth telluride. *Proceedings of the Physical Society* **72**, 17 (1958).

[73] H. S. Ji *et al.*, Vacancy-suppressed lattice conductivity of high-ZT In_4Se_{3-x}. *Physical Review B* **87**, 125111 (2013).

[74] J. Wu *et al.*, Superior radiation resistance of $In_{1-x}Ga_xN$ alloys: Full-solar-spectrum photovoltaic material system. *Journal of Applied Physics* **94**, 6477 (2003).

[75] V. N. Brudnyi, S. N. Grinyaev, and N. G. Kolin, Electronic properties of irradiated semiconductors: A model of the Fermi level pinning. *Semiconductors* **37**, 557 (2003).

[76] I. Chowdhury *et al.*, On-chip cooling by superlattice-based thin-film thermoelectrics. *Nature Nanotechnology* **4**, 235 (2009).

[77] N. E. Coates *et al.*, Effect of interfacial properties on polymer-nanocrystal thermoelectric transport. *Advanced Materials* **25**, 1629 (2013).

[78] X. L. Yang, S. H. Guo, F. T. Chan, K. W. Wong, and W. Y. Ching, Analytic solution of a two-dimensional hydrogen atom. I. Nonrelativistic theory. *Physical Review A* **43**, 1186 (1991).

[79] A. K. M. Newaz *et al.*, Electrical control of optical properties of monolayer MoS_2. *Solid State Communications* **155**, 49 (2013).

[80] K. F. Mak *et al.*, Tightly bound trions in monolayer MoS_2. *Nature Materials* **12**, 207 (2012).

[81] J. S. Ross *et al.*, Electrical control of neutral and charged excitons in a monolayer semiconductor. *Nature Communications* **4**, 1473 (2013).

[82] K. F. Mak, C. Lee, J. Hone, J. Shan, and T. F. Heinz, Atomically thin MoS_2: A new direct-gap semiconductor. *Physical Review Letters* **105**, 136805 (2010).

[83] M. M. Benameur *et al.*, Visibility of dichalcogenide nanolayers. *Nanotechnology* **22**, 125706 (2011).

[84] C. Lee *et al.*, Anomalous lattice vibrations of single- and few-layer MoS_2. *ACS Nano* **4**, 2695 (2010).

[85] S. Tongay *et al.*, Thermally driven crossover from indirect toward direct bandgap in 2D semiconductors: $MoSe_2$ versus MoS_2. *Nano Letters* **12**, 5576 (2012).

[86] S. Horzum *et al.*, Phonon softening and direct to indirect band gap crossover in strained single-layer $MoSe_2$. *Physical Review B* **87**, 125415 (2013).

[87] H. Sahin *et al.*, Anomalous Raman spectra and thickness-dependent electronic properties of WSe_2. *Physical Review B* **87**, 165409 (2013).

[88] W. Zhao *et al.*, Evolution of electronic structure in atomically thin sheets of WS_2 and WSe_2. *ACS Nano* **7**, 791 (2013).

[89] S. Mathew *et al.*, Magnetism in MoS_2 induced by proton irradiation. *Applied Physics Letters* **101**, 102103 (2012).

[90] G. Finkelstein, H. Shtrikman, and I. Bar-Joseph, Optical spectroscopy of a two-dimensional electron gas near the metal-insulator transition. *Physical Review Letters* **74**, 976 (1995).

[91] H. Qiu *et al.*, Electrical characterization of back-gated bi-layer MoS_2 field-effect transistors and the effect of ambient on their performances. *Applied Physics Letters* **100**, 123104 (2012).

[92] T. Schmidt, K. Lischka, and W. Zulehner, Excitation-power dependence of the near-band-edge photoluminescence of semiconductors. *Physical Review B* **45**, 8989 (1992).

[93] K.-K. Liu *et al.*, Growth of large-area and highly crystalline MoS_2 thin layers on insulating substrates. *Nano Letters* **12**, 1538 (2012).

[94] Y. Yu *et al.*, Controlled scalable synthesis of uniform, high-quality monolayer and few-layer MoS_2 films. *Scientific Reports* **3**, 1866 (2013).

[95] P. E. Blöchl, Projector augmented-wave method. *Physical Review B* **50**, 17953 (1994).

[96] J. P. Perdew, K. Burke, and M. Ernzerhof, Generalized gradient approximation made simple. *Physical Review Letters* **77**, 3865 (1996).

[97] S. Grimme, Semiempirical GGA-type density functional constructed with a long-range dispersion correction. *Journal of Computational Chemistry* **27**, 1787 (2006).

[98] G. Kresse and J. Hafner, Ab initiomolecular dynamics for liquid metals. *Physical Review B* **47**, 558 (1993).

[99] P. Esquinazi *et al.*, Induced magnetic ordering by proton irradiation in graphite. *Physical Review Letters* **91**, 227201 (2003).

[100] A. Hashimoto, K. Suenaga, A. Gloter, K. Urita, and S. Lijima, Direct evidence for atomic defects in graphene layers. *Nature* **430**, 870 (2004).

[101] O. V. Yazyev and L. Helm, Defect-induced magnetism in graphene. *Physical Review B* **75**, 125408 (2007).

[102] S. Tongay *et al.*, Broad-range modulation of light emission in two-dimensional semiconductors by molecular physisorption gating. *Nano Letters* **13**, 2831 (2013).

[103] K. M. Yu *et al.*, Diluted II-VI oxide semiconductors with multiple band gaps. *Physical Review Letters* **91**, 246403 (2003).

[104] B. Radisavljevic, A. Radenovic, J. Brivio, V. Giacometti, and A. Kis, Single-layer MoS_2 transistors. *Nature Nanotechnology* **6**, 147 (2011).

[105] S. Kim *et al.*, High-mobility and low-power thin-film transistors based on multilayer MoS_2 crystals. *Nature Communications* **3**, 1011 (2012).

[106] B. Radisavljevic, M. B. Whitwick, and A. Kis, Integrated circuits and logic operations based on single-layer MoS_2. *ACS Nano* **5**, 9934 (2011).

[107] H. Wang *et al.*, Integrated circuits based on bilayer MoS_2 transistors. *Nano Letters* **12**, 4674 (2012).

[108] A. Pospischil, M. M. Furchi, and T. Mueller, Solar-energy conversion and light emission in an atomic monolayer *p-n* diode. *Nature Nanotechnology* **9**, 257 (2014).

[109] B. W. Baugher, H. O. Churchill, Y. Yang, and P. Jarillo-Herrero, Optoelectronic devices based on electrically tunable *p-n* diodes in a monolayer dichalcogenide. *Nature Nanotechnology* **9**, 262 (2014).

[110] J. S. Ross *et al.*, Electrically tunable excitonic light-emitting diodes based on monolayer WSe_2 *p-n* junctions. *Nature Nanotechnology* **9**, 268 (2014).

[111] J. Kang, S. Tongay, J. Zhou, J. Li, and J. Wu, Band offsets and heterostructures of two-dimensional semiconductors. *Applied Physics Letters* **102**, 012111 (2013).

[112] Y. J. Zhang, J. T. Ye, Y. Yomogida, T. Takenobu, and Y. Iwasa, Formation of a stable *p–n* junction in a liquid-gated MoS_2 ambipolar transistor. *Nano Letters* **13**, 3023 (2013).

[113] S. Chuang *et al.*, Mos_2 *p*-type transistors and diodes enabled by high work function MoO_x contacts. *Nano Letters* **14**, 1337 (2014).

[114] M. Fontana *et al.*, Electron-hole transport and photovoltaic effect in gated MoS_2 schottky junctions. *Scientific Reports* **3**, 1634 (2013).

[115] S. Mouri, Y. Miyauchi, and K. Matsuda, Tunable photoluminescence of monolayer MoS_2 via chemical doping. *Nano Letters* **13**, 5944 (2013).

[116] J. D. Lin *et al.*, Electron-doping-enhanced trion formation in monolayer molybdenum disulfide functionalized with cesium carbonate. *ACS Nano* **8,** 5323 (2014).

[117] C.-H. Lee *et al.*, Atomically thin *p-n* junctions with van der Waals heterointerfaces. *Nature Nanotechnology* **9,** 676 (2014).

[118] H. Fang *et al.*, Strong interlayer coupling in van der waals heterostructures built from single-layer chalcogenides. *Proceedings of the National Academy of Sciences USA* **111**, 6198 (2014).

[119] H. Qiu *et al.*, Hopping transport through defect-induced localized states in molybdenum disulphide. *Nature Communications* **4**, 2642 (2013).

[120] K. F. Mak, K. He, J. Shan, and T. F. Heinz, Control of valley polarization in monolayer MoS_2 by optical helicity. *Nature Nanotechnology* **7**, 494 (2012).

[121] R. Suzuki *et al.*, Valley-dependent spin polarization in bulk MoS_2 with broken inversion symmetry. *Nature Nanotechnology* **9**, 611 (2014).

[122] K. Dolui, I. Rungger, C. Das Pemmaraju, and S. Sanvito, Possible doping strategies for MoS2 monolayers: An ab initio study. *Physical Review B* **88**, 075420 (2013).

[123] J. A. Wilson and A. D. Yoffe, The transition metal dichalcogenides discussion and interpretation of the observed optical, electrical and structural properties. *Advances in Physics* **18**, 193 (1969).

[124] V. Ivanovskaya *et al.*, Ab initio study of bilateral doping within the MoS_2-NbS_2 system. *Physical Review B* **78**, 134104 (2008).

[125] F. L. Deepak *et al.*, Fullerene-like (IF) $Nb_xMo_{1-x}S_2$ nanoparticles. *Journal of the American Chemical Society* **129**, 12549 (2007).

[126] M. R. Laskar *et al.*, P-type doping of MoS_2 thin films using Nb. *Applied Physics Letters* **104**, 092104 (2014).

[127] S. Tongay *et al.*, Two-dimensional semiconductor alloys: Monolayer $Mo_{1-x}W_xSe_2$. *Applied Physics Letters* **104**, 012101 (2014).

[128] B. Chakraborty *et al.*, Symmetry-dependent phonon renormalization in monolayer MoS_2 transistor. *Physical Review B* **85**, 161403 (2012).

[129] Y.-H. Lee *et al.*, Synthesis of large-area MoS_2 atomic layers with chemical vapor deposition. *Advanced Materials* **24**, 2320 (2012).

[130] Y.-C. Lin *et al.*, Properties of individual dopant atoms in single-layer MoS_2: Atomic structure, migration, and enhanced reactivity. *Advanced Materials* **26**, 2857 (2014).

[131] M. Remskar, Z. Skraba, P. Stadelmann, and F. Levy, Structural stabilization of new compounds: MoS_2 and WS_2 micro- and nanotubes alloyed with gold and silver. *Advanced Materials* **12**, 814 (2000).

[132] P. Joensen, E. D. Crozier, N. Alberding, and R. F. Frindt, A study of single-layer and restacked MoS_2 by x-ray diffraction and x-ray absorption spectroscopy. *Jounal of Physics C: Solid State Physics* **20**, 4043 (1987).

[133] N. R. Pradhan *et al.*, Ambipolar molybdenum diselenide field-effect transistors: Field-effect and Hall mobilities. *ACS Nano* **8**, 7923 (2014).

[134] W. Jin *et al.*, Direct measurement of the thickness-dependent electronic band structure of MoS_2 using angle-resolved photoemission spectroscopy. *Physical Review Letters* **111**, 106801 (2013).

[135] D. Kiriya, M. Tosun, P. Zhao, J. S. Kang, and A. Javey, Air-stable surface charge transfer doping of MoS_2 by benzyl viologen. *Journal of the American Chemical Society* **136**, 7853 (2014).

[136] S. Tongay *et al.*, Tuning interlayer coupling in large-area heterostructures with cvd-grown MoS_2 and WS_2 monolayers. *Nano Letters* **14**, 3185 (2014).

[137] W. J. Yu *et al.*, Highly efficient gate-tunable photocurrent generation in vertical heterostructures of layered materials. *Nature Nanotechnology* **8,** 952 (2013).

[138] T. S. Kasırga *et al.*, Photoresponse of a strongly correlated material determined by scanning photocurrent microscopy. *Nature Nanotechnology* **7**, 723 (2012).

[139] S. Zhang, J. Y. Chou, and L. J. Lauhon, Direct correlation of structural domain formation with the metal insulator transition in a VO_2 nanobeam. *Nano Letters* **9**, 4527 (2009).

[140] J. Wu *et al.*, Strain-induced self organization of metal–insulator domains in single-crystalline VO_2 nanobeams. *Nano Letters* **6**, 2313 (2006).

[141] S. Lee *et al.*, Axially engineered metal–insulator phase transition by graded doping VO_2 nanowires. *Journal of the American Chemical Society* **135**, 4850 (2013).

[142] D. Fu *et al.*, Comprehensive study of the metal-insulator transition in pulsed laser deposited epitaxial VO_2 thin films. *Journal of Applied Physics* **113**, 043707 (2013).

[143] B. S. Guiton, Q. Gu, A. L. Prieto, M. S. Gudiksen, and H. Park, Single-crystalline vanadium dioxide nanowires with rectangular cross sections. *Journal of the American Chemical Society* **127**, 498 (2005).

[144] Q. Gu, A. Falk, J. Wu, L. Ouyang, and H. Park, Current-driven phase oscillation and domain-wall propagation in $W_xV_{1-x}O_2$ nanobeams. *Nano Letters* **7**, 363 (2007).

[145] C. Miller *et al.*, Unusually long free carrier lifetime and metal-insulator band offset in vanadium dioxide. *Physical Review B* **85**, 085111 (2012).

[146] D.-W. Oh, C. Ko, S. Ramanathan, and D. G. Cahill, Thermal conductivity and dynamic heat capacity across the metal-insulator transition in thin film VO_2. *Applied Physics Letters* **96**, 151906 (2010).